Growth, Fabrication and Characterization of Metamorphic InGaSb Photodetectors for Application in 2.0 μm and Beyond

By

Farseem Mannan Mohammedy

Growth, Fabrication and Characterization of Metamorphic InGaSb Photodetectors for Application in 2.0 μm and Beyond

By
Farseem Mannan Mohammedy
B.Sc. (1999), M.Sc. (2002)
Bangladesh University of Engineering and Technology,
Dhaka, Bangladesh

A Thesis
Submitted to the School of Graduate Studies
in Partial Fulfillment of the Requirements
for the Degree of Doctor of Philosophy

McMaster University
Hamilton, Ontario, Canada

Doctor of Philosophy (2008) (Electrical and Computer Engineering)	McMaster University Hamilton, Ontario

TITLE: *Growth, Fabrication and Characterization of Metamorphic InGaSb Photodetectors for Application in 2.0 μm and Beyond*

AUTHOR: Farseem Mannan Mohammedy,	B.Sc., M.Sc. Bangladesh University of Engineering and Technology, Dhaka, Bangladesh.
SUPERVISOR: Prof. M. Jamal Deen	Professor, Electrical and Computer Eng.
Co-SUPERVISOR: Prof. David A. Thompson	Professor Emeritus, Engineering Physics
NUMBER OF PAGES: xvii, 151	

Abstract

Sensing systems for mid-infrared wavelengths (2 to 5 μm) have important applications in biomedical, atmospheric and process gas monitoring systems. For lack of a suitable substrate, the full potential of GaSb-based materials, which are particularly suitable for operating in these wavelengths, are not completely realized. Hence, metamorphic growth technology, that allows the growth of semiconductor epilayers of arbitrary composition on any substrate, has been explored for antimony materials in this research. This makes the growth of device layers, containing arbitrary composition of GaSb-based materials, possible on commercially available 6"-GaAs substrates, and thereby reducing fabrication cost.

Metamorphic growth of $In_{0.15}Ga_{0.85}Sb$ was achieved using gas-source molecular beam epitaxy by growing compositionally graded $In_xGa_{1-x}Sb$ buffer layers on a GaSb substrate. The effects of growth temperature on the quality of the metamorphic buffer layers along with the etching issues (both wet and dry) of GaSb-based materials were studied.

Homo-junction n-i-p and p-i-n diodes were fabricated on $In_{0.15}Ga_{0.85}Sb$ metamorphic layers. The dark current and its temperature dependence were measured and the extraction of area and perimeter components of dark current was done. The modeling of the components of dark current suggests that the diode currents were dominated by surface leakage. Surface passivation by silicon nitride and polyimide were investigated and our findings suggest that the former resulted in a better passivated surface. Responsivity measurements show that $In_{0.18}Ga_{0.82}Sb$ diodes, metamorphically grown on GaSb substrates, have a cut-off wavelength of 2270 nm. Finally, hole (β) and previously unreported electron (α) ionization coefficients, at room temperature and 90^{o} C, were extracted from these structures. The results show that $\alpha > \beta$ for $In_{0.10}Ga_{0.90}Sb$ for both temperatures.

These photodetectors can be implemented in practical receiver systems for mid-infrared applications, such as atmospheric CO_2 and methane detection at 2.0 μm. The possibility of growing antimony-based device layers on larger substrates, paves the way for future optoelectronic receiver systems operating at longer wavelengths, where both the photodetector and the amplifier can be integrated in the same module.

This thesis is dedicated to my father,

MOHAMMED ABDUL MANNAN,

and to the memory of my mother,

HOSNE ARA MANNAN,

who didn't live to see its completion.

Acknowledgements

All praise be to The Omniscient and The Omnipotent, Who gave me the ability to finish this thesis. Throughout this six years of my stay, my supervisor, Professor M. Jamal Deen, was always there with an open door for all the problems that I faced, even in the most bleak and dark moments of my personal life. His excellent mentorship, guidance and personality will remain a cherished memory for the remaining days of my life. Next, I thank Professor Dave Thompson, for his encouragement and supervision. His deep understanding of the semiconductors was most useful during the growths in MBE and the fabrications. I particularly admire his likeness to precision both in work and in words. Other than these two supervisors, there was Dr. Bradley J. Robinson, who acted like a pseudo-supervisor throughout. He taught me the MBE and introduced me to the intricacies of the experimentalists' world. I must cherish the illuminating discussions that we had over many issues of science, technology and society.

Professor Peter Mascher and Professor Shiva Kumar spared time out of their busy schedule to sit into my committee meetings and also in my comprehensive exam committee. I thank them for being so kind and helpful to me for all these years. Prof. Xun Li was always welcoming to my curiosities.

At this point, I must acknowledge the help that I got from two persons outside McMaster University – Dr. Igor Vurgaftman (Naval Research Laboratory, USA) and Professor Partha Dutta (Rensselaer Polytechnic Institute, USA), who always took the pains to reply my email queries about material fundamentals and antimony processing issues. Thank you very much.

Since I worked in two groups, obviously I have a long list of persons to acknowledge. My thanks go to my friends at the Microelectronics Research Lab: Sasan Naseh, Rizwan Murji, Yeasser El-Battawy, Saman Asgaran, Nabeel Jafferali, Ahmad Fakhr, Kalyan Bhattacharyya, the three Wei's, Munir El-Desouki, Naser Faramarzpour, Yasaman Ardeshirpour, Moussa Kfouri, Hamed Mazhab-Jafari, Waleed Shinwari. Mohammad Naser, famous for his addiction to long rambling monologues, enlightened many evenings, and was patient during my incessant pickings on him. From Engineering Physics: Y. Shi, J. Huang, S. Tavakoli, A. Youngker, and Cui Kai from Materials Science deserve mention. Dr. Oksana Hulko did all the sample preparation required for the TEMs and took the images for me. I am greatly indebted to her for her assistance. Doris S. and Zhilin P. gave me passionate training on the clean room procedures; they were always there when I was in need. Graham Pearson was a real friend and great research scientist to look for when in need. I also thank Dr. O. Marinov for his help with equipments. My other friends and well-wishers from the Bangladeshi community at Hamilton: Prof. W. Khan, Prof. M. Howlader, Prof. A. S. Huque, Dr. M.S.A. Zilany, M. Hasanuzzaman, Ferdous K. Khan, Tanvir Quadir and Dr. Asif Quader must be mentioned. My uncle Dr. M. A. Akhteruzzaman and his family must be acknowledged for providing support.

I would also like to thank the administrative and technical staff of the ECE department of McMaster University. Special mentions go to Cheryl Gies and Cosmin Coroiu, who have two of the most loving faces in the department.

I am truly indebted to my wife, Farhana Mannan, who has always been there for me at all times, silently taking care of the daily chores.

Finally, my parents suffered in many ways over this long time of my absence from home. My mother could not live to see this thesis. I take this opportunity here to dedicate this thesis to the loving memory of my mother and to my father, for his enduring patience for the insufferable loneliness that he faced throughout this time.

Table of Contents

List of Figures

List of Tables

RIE	Reactive Ion Etching
RTA	Rapid Thermal Anneals
RTD	Resonant Tunneling Diode
SEM	Scanning Electron Microscope
TMAH	Tetramethyl Ammonium Hydroxide
VLIR	Very Long Infrared
XTEM	Cross-sectional Transmission Electron Microscopic

Symbols

α	Absorption Coefficient, Electron Ionization Coefficient
β	Hole Ionization Coefficient
λ	Wavelength, Mean Free Path
ϕ	Beam Pressure, Energy States
η	Ionization Efficiency, Quantum Efficiency
τ	Minority Carrier Lifetime
θ_B	Bragg Angle
$\partial\theta$	Peak Separation
μ_{n}, μ_{p}	Electron and Hole Mobility
Δ_{so}	Split-off Band
a	Lattice Constant
$a_{\perp}$	Perpendicular Lattice Constant
$a_{\parallel}$	In-Plane Lattice Constant
B_s	Fitting Parameter
$C_{12}(x)$, $C_{11}(x)$	Stiffness Coefficients
D	Minority Carrier Diffusion Constant
D*	Detectivity
E_F	Fermi Level Energy
E_g	Bandgap
E_r	Optical Phonon Energy
$F_{1/2}(x)$	Fermi-Dirac Integral
F	Shape-Factor for The L-Band

$F(V)$	Electric Field
I_{ion}	Ion Flux
J	Current Density
J_A	Current Density Component from Area
J_{diff}	Diffusion of Minority Carriers
J_{disl}	Current Density From Dislocations
J_{GR}	Generation Current
J_P	Current Density Component From Perimeter
J_{shunt}	Surface Leakage
J_{X}	Flux
k	Hole to Electron Ionization Ratio
l_s, W	Depletion Width
M	Molecular wt., Gain
M_e, M_h	Gain Due to Electron And Hole
$\mathrm{m_e}$, $\mathrm{m_h}$, $\mathrm{m_{so}}$	Electron, Hole And Split-Off Effective Masses, respectively
N	Dislocation Density
$n(N_D)$, $p(N_A)$	Doping Level (Electron, Hole)
N_C	Density of States
n_i	Intrinsic Carrier Concentration
P_{plasma}	Microwave Plasma Power
P_{rf}	Rf Power
q	Charge
R	Responsivity
R_oA	Zero-Bias-Resistance-Area Product
r_s	Surface Resistivity
rf	Radio Frequency
T	Absolute Temperature
T_G	Growth Temperature
V_{bs}	Depletion Potential
V_{DC}	Bias Voltage
Z	Atomic Number
μ_{Hall} , n_{Hall}	Hall Measurement Values For Mobility And Concentration

Chapter 1 Introduction

1.1 The 6.1 Å Family

Herbert Kroemer, the Nobel laureate who pioneered the molecular beam epitaxy of antimonides in mid-1980's, in his 2004 review paper[1] expressed the vision about the emerging field of a new sub-family among the III-V compound semiconductors: "The three semiconductors InAs, GaSb, and AlSb form an approximately lattice-matched set around 6.1 Å, with (room temperature) energy gaps ranging from 0.36 eV (InAs) to 1.61 eV (AlSb). Like other compound semiconductors, they are of interest principally for their heterostructures, especially heterostructures combining InAs with the two antimonides and their alloys. This combination offers band lineups that are drastically different from those of the more widely studied (Al,Ga)As system, and the lineups are one of the principal reasons for interest in the **6.1 Å family**".

The 6.1 Å family members are shown in Figure 1.1 with their associated bandgap and lattice constant with respect to other III-V semiconductors. This figure also shows the relative position of InGaSb, in relation to other members of the 6.1 Å family and other semiconductors as well. Among the 6.1 Å family the binary compound GaSb is readily available as a substrate for epitaxial growth of heterostructure-based devices useful for their optoelectronic properties in areas of emerging applications [2]. The binary compounds (GaSb, AlSb, InAs), along with their ternary or quaternary alloys, constitute very interesting band alignments (type-II or III) (see Figure 1.2) leading to many interesting device structures which can be exploited using various combinations of these materials and their band alignments [3]. Reference [4] reviews research associated with this 6.1 Å family for the development of high-speed, low-power, electronic devices. This arises from the very high room temperature mobilities exhibited by these binary compounds. These mobilities are even higher when cooled. For example, InAs has very high electron mobility (30,000 cm^2/V.s at 300K) and devices exploiting InAs-channels can utilize this property to great advantage. The development of antimony-based transistors for use in low-noise high-frequency amplifiers, digital circuits, and mixed-signal circuits could provide the enabling technology needed to address the rapidly expanding need for higher capacity in communications [4].

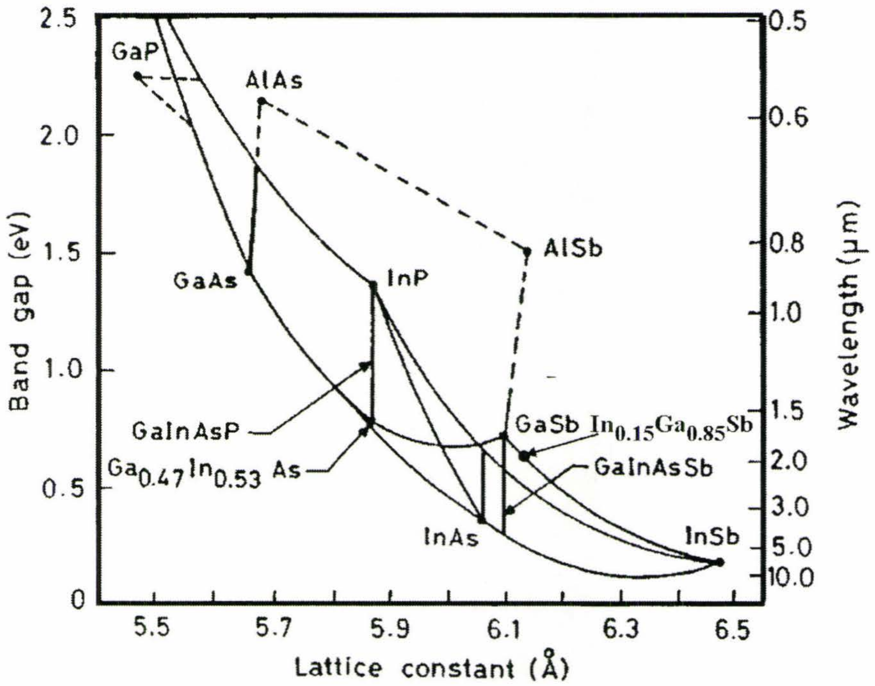

Figure 1.1: III-V semiconductor materials and the 6.1 Å family [2].

Reference [4] is a comprehensive review of antimony-based electronic device structures – high electron mobility transistors (HEMTs), resonant tunneling diodes (RTDs) and heterojunction bipolar transistors (HBTs). The real advantage of antimony based devices over those of silicon, GaAs or InP based devices, is their ability to achieve high frequency operation with very low power consumption. As electronic systems become more complex, more mobile and more demanding in terms of frequency and bandwidth, there is a need to develop new technologies that offer improved performance, particularly in the area of power consumption. This, according to Tim Whitaker of *Compound Semiconductor* [5], is one of the key factors behind DARPA's antimonide-based compound semiconductors program, which began in July 2001. Antimonide-based integrated ciruits (ICs) have already demonstrated the potential to offer a 10-fold reduction in power consumption compared with equivalent InP-based devices. The technology is very promising for low-voltage mm-wave ICs, as well as very high-speed, low-power digital ICs.

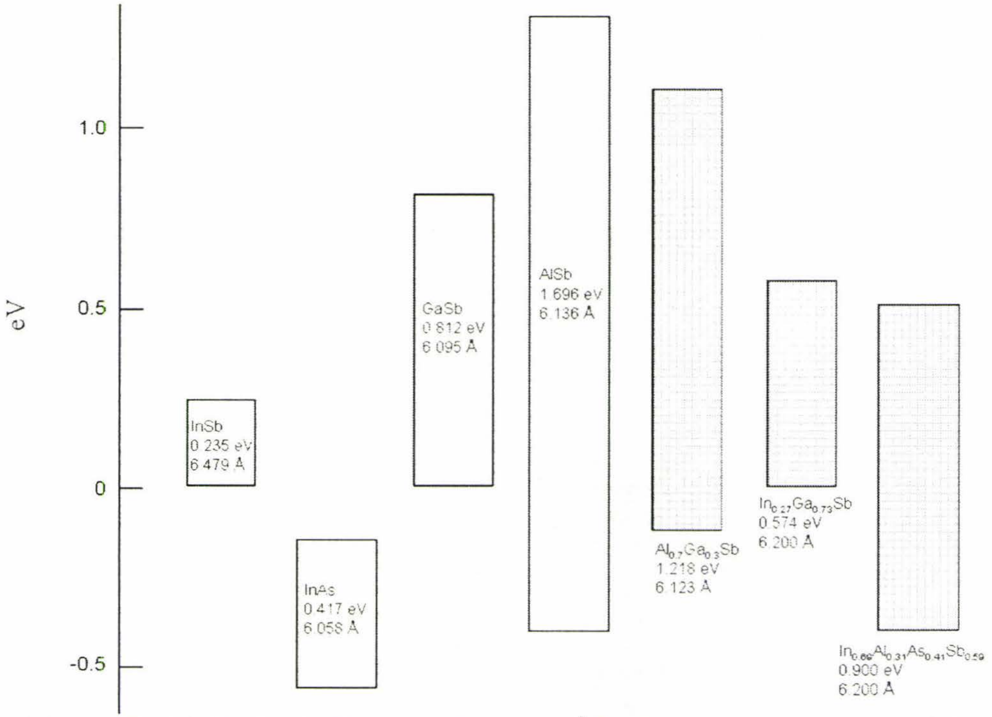

Figure 1.2: Relative band alignments for the 6.1 Å family and the related alloys [4].

Among the many potential applications are digitally beam-steered phased array receivers, particularly those deployed in space; 80–160 Gbit/s optical communication systems; unmanned reconnaissance vehicles; and mobile, battery-powered systems in general [5]. Powerful and easy-to-use lasers operating in the mid-infrared (MIR) range are important for a variety of industrial and military applications, including IR countermeasures, light detection and ranging, remote trace-gas sensing, and secure free-space communications. MIR range has tremendous defense opportunities. Other than night-vision applications, IR operation is sought in high-tech defense mechanisms such as heat-seeking missiles, aircraft and enemy tank imaging. IR counter-measures include shooting a beam to the incoming missile and blind its detectors. LIR applications include more important and classified applications as ballistic missiles.

1.2 Applications in the Mid-Infrared Wavelength

The motivation to choose the antimonide family is to generate and detect light in the mid infrared (MIR) wavelength region which this materials system supports. In Table 1.1, the different wavelength regions along with their designated wavelengths in microns are shown.

Table 1.1: Wavelength ranges [6],[7].

	Wavelength, μm
Near infrared (NIR)	< 2.0
Mid infrared (MIR or mid-IR)	2–5
Long infrared (LIR)	8–14
Very long infrared (VLIR)	14–50

The near-IR, widely known as NIR region, is chosen for telecommunication purposes as fiber optics operating at those wavelengths prove to have very low loss per km thus requiring fewer repeaters[8], [9]. Fiber losses are considerably higher for shorter wavelengths and exceed 5 dB/km in the visible spectral region which is unsuitable for long-haul telecommunication [10]. For single mode fibers, narrow windows of low attenuation exist at longer wavelengths around 1.3 and 1.55 μm. At 1.55 μm the attenuation is < 0.2 dB/ km [9]. Two reasons to aim for MIR detection are the development of non-silica fibers and potential biomedical applications.

Non-Silica Fibers

In the NIR region, the fundamental silica fiber attenuation is dominated by Rayleigh scattering and multiphonon absorption from the infrared absorption edge. There are ways to reduce this loss even further in the MIR region of the spectrum. This is possible because of the inverse 4th power wavelength dependence of the Rayleigh scattering (λ^{-4}). Hence, increasing the wavelength decreases the loss. This can be made possible by employing higher atomic mass materials. Likely candidates are fluoride, fluoride-chloride, chalcogenide and possible oxides [9]. Chalcogenide glasses generally comprise S, Se and Te together with Ge, Si, As and Sb and are compatible with MIR and LIR operation. Non-silica fluoride glasses include fluorides of zirconium (ZrF_4) with added fluorides of Zn, La, Ba, Al used as modifiers and stabilizers.

Other compound metal fluorides (for example, zirconium-barium-lanthanum-aluminum fluoride etc.) are also available to serve the purpose. Fibers based on ZrF_4 have losses projected to be $\sim 10^{-2}$ dB/km at 2.55 μm confirmed with better experimental data [11]. Recent refinements of the scattering loss have modified this value to be 0.024 dB/km or about eight times less than that for silica fibers (p.58 of [12]). However, various loss mechanisms limit the predicted performance of the fluoride glasses, which are also less durable than silica fibers when faced with atmospheric moisture and water. The use of hermetic coating may be essential for these fibers. The potential of developing ultra-low loss and hence repeater-less transoceanic optical fiber communication is the main driving force towards the development of non-silica fibers. A comparison of the spectral losses for several types of non-silica fibers is shown in Figure 1.3.

A comprehensive review of the various non-silica IR fibers can be found in [12]. While IR fibers are becoming increasingly important, they require further development before they replace the present day silica fibers. There are important technological and commercial obstacles that have to be overcome to implement non-silica IR-fibers (IR) for long-haul communications. The author in [12] notes: "In general, both the optical and mechanical properties of IR fibers remain inferior to silica fibers and, therefore, the use of IR fibers is still limited primarily to non-telecommunication, short-haul applications requiring only tens of meters of fiber rather than kilometer lengths common to telecommunication applications. The short-haul nature of IR fibers results from the fact that most IR fibers have losses in the few dB/m range. An exception is fluoride glass fibers which can have losses as low as a few dB/km. In addition, IR fibers are more fragile. These deleterious features have slowed the acceptance of IR fibers and restricted their use today to applications in chemical sensing, thermometry, and laser power delivery."

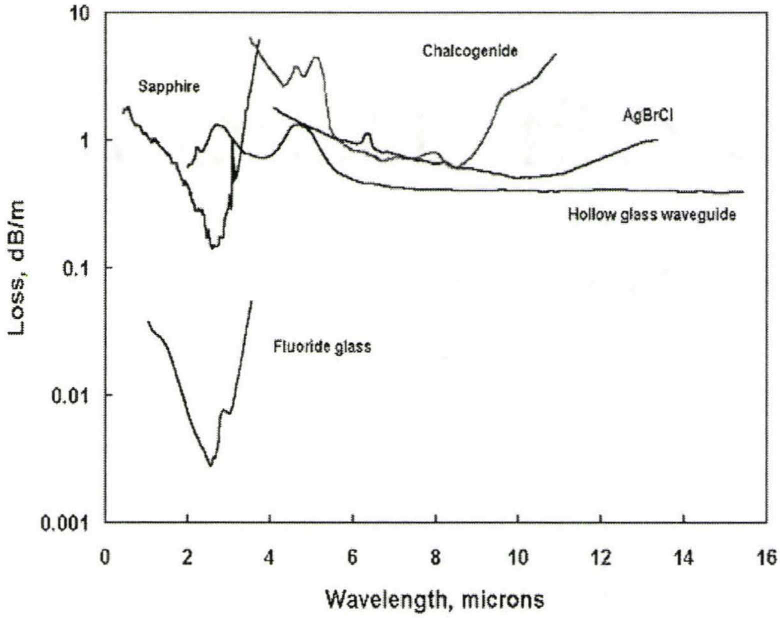

Figure 1.3: Loss spectra for some common IR fibers [12].

Other Applications

Detectors are used for detecting biological and hazardous bio-molecules. IR detectors can be used in remote sensing of biotoxins (e.g. smallpox, sarin gas, ricin, anthrax) and sensing in hazardous environments. Also continuous monitoring of water contamination and bacteria detection is possible by infrared sensors. Quantum well infrared photodetectors (QWIPs) operating in the MIR spectral range can be used in a host of applications, such as [13]: medical diagnosis, location of forest fires, unwanted vegetation encroachment, monitoring crop health, coastal erosion, deforestation of tropical rain forests and the ability to locate and monitor thermal and gaseous pollution sites. There is a new emerging multidisciplinary field known as "bio-nanophotonics" where tremendous opportunity of photonics applications is possible [14]. The IR light is important for bio-imaging as it can penetrate deeper into the tissue producing information for 'tissue engineering'.

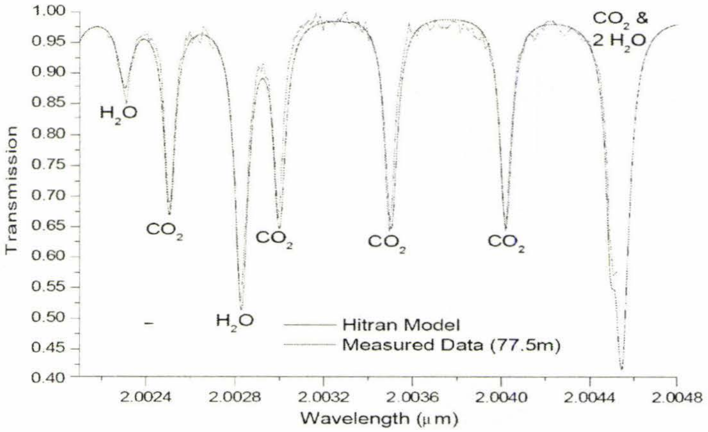

Figure 1.4: Absorption wavelengths for water and the carbon dioxide lines [16].

Among other applications of the MIR spectral region are monitoring of chemical processes (combustion and gas flow monitoring, H_2S detection), chemical sensor applications (as some molecular species possess characteristic vibrational bands in 1–11 μm) and the semiconductor process industry (HCl monitoring during plasma-etch of poly-Si). There is also great interest in broadband detectors for numerous critical applications such as temperature sensing, process control, and atmospheric monitoring. The 0.6 to 2.5 μm spectral region has a large number of principal absorption lines, which enable active and passive remote sensing of O_2, H_2O, CH_4, CO, NH_3, and a number of hydrocarbons in the atmosphere [15],[16]. Carbon dioxide is a key greenhouse gas that affects the global warming and it is important to trace the amount of CO_2 in the atmosphere. Figure 1.4 shows the absorption spectra for atmospheric CO_2 and H_2O lines around 2 μm wavelength. Satellites having detectors in MIR range can help monitoring forest fires [17]. The photodetectors fabricated in this project can replace the existing MCT ones in the satellite imaging systems for the same wavelength range. For the same detectivity as the MCT detectors, our InGaSb photodetectors do not require any cooling.

1.3 Metamorphic Buffer layers

In order to tune the device to a specific wavelength, it is necessary to use ternary or even quaternary compounds using the elements Ga, In, As, Sb with composition appropriate to the desired wavelength. These compounds typically have lattice constants different to the GaSb substrate resulting in strained growth and high defect densities. In order to mitigate this problem, metamorphic buffer layers (M-buffers) are used allowing growth of a new pseudo-substrate having the desired lattice constant on which to grow the device structure with low defect densities. Metamorphic growth is initiated on a standard substrate and by varying the composition of the subsequent layers, either gradually or in steps, can ultimately provide a new layer with a different lattice constant. The lattice mismatches in the buffers are accommodated through the formation of dislocations. The density of threading dislocations in the top layer can then be greatly reduced by heat treatment (annealing) and thus the top layer of the M-buffer becomes the required pseudo-substrate. Since the use of metamorphic buffers provides the device designer with increased flexibility to 'bandgap engineer' different materials with different properties (through the lattice constant) and since GaSb substrates are currently limited to 2-inch diameter wafers, the use of GaSb metamorphic layers on InP could yield 4-inch wafers for fabricating mid-infrared, antimony-based lasers and photodetectors.

The interest in M-buffers is growing considerably because of the attractive features of reduced cost and comparable electronic/optoelectronic properties of those layers grown on M-buffers [17]-[31]. Near the substrate interface, the dislocation density is typically ~10^9 cm^{-2} gradually reducing to ~10^6 cm^{-2} near the top of the M-buffer and the root-mean-square value of surface roughness is around 14 Å [19],[20]. Electronic transport in layers grown on M-buffers has been characterized by Hall measurement techniques. A comparison shows that the electron mobility in HEMT devices metamorphically grown on GaAs remains comparable to those grown lattice matched to the substrate at room temperature [19]. Most importantly, the electron mobilities and sheet densities do not degrade significantly. There are two ways to achieve the metamorphic structure — step graded and linearly graded. From photoluminescence studies it has been suggested that a linearly graded M-buffer has narrower and higher intensity photoluminescence peaks. Also, photodetectors grown on a linearly graded M-buffer [21],[23] have exhibited reduced dark current values, allowing fabrication of low leakage photodetectors [23].

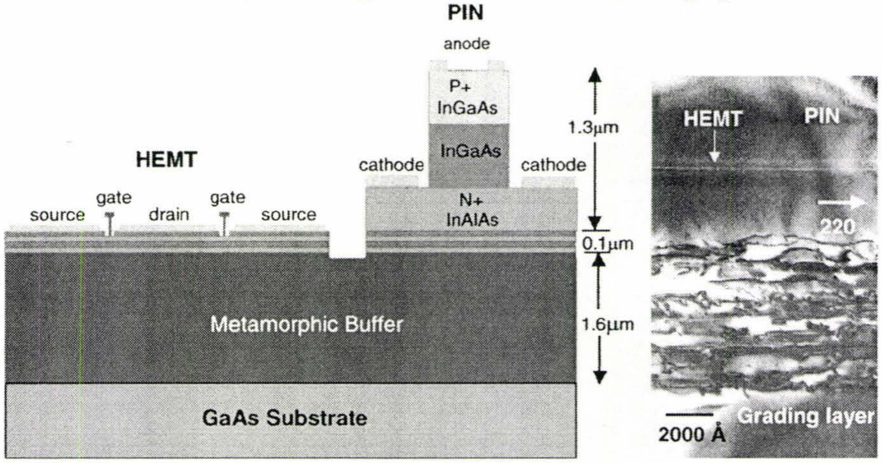

Figure 1.5: Schematic cross-sectional view of the OEIC with metamorphic HEMT and photodetector; and XTEM image showing buffer layers and the HEMT and p-i-n structure [29].

Extensive work on M-buffers or substrates has been carried out at Raytheon Microelectronics Centre and are reported in [18],[19],[21],[23],[24],[27]-[29]. Their research concentrated on growing buffer layers on a GaAs substrate and changing the lattice constants of the subsequent layers metamorphically through steadily adding In to reach In$_{0.53}$Ga$_{0.47}$As, allowing good quality, relaxed InP to be deposited on the top layers. Transistors and photodetectors could then be fabricated in the metamorphic InP layer as part of an integrated optoelectronic receiver exhibiting satisfactory performance. Photodiodes fabricated on these M-buffers [21] achieved a low dark current of 500 pA, a responsivity of 0.6 A/W, and a 3dB bandwidth of 38 GHz at 5 V reverse bias for 1.55 µm light. Figure 1.5 shows one such detector-HEMT structure fabricated on M-buffers along with the cross-sectional transmission electron microscopic (XTEM) image.

Other materials details, e.g. thermal properties of the resulting M-layers, effects of growth temperature on surface roughness, of M-substrates can be found in [26]-[31].

In order to explore the full potential of the 6.1 Å family and to be able to grow epilayers of any composition that may be of interest to the device designer, the present thesis has extended the metamorphic growth techniques to one member of the 6.1 Å family.

1.4 Comparison of Detector Technologies

Modern IR detectors got a boost after the second world war. Detectors based on the lead salt compounds were available in the 1950's for usage in anti-air-missile-seeking applications [32]. The discovery of transistors gave a boost in the maturing of processing techniques which helped the advancement of the detectors also. At the end of the 1950's, the potential of III-V and II-VI semiconductors were recognized and put to use. "These alloys allowed the bandgap of the semiconductor and hence the spectral response of the detector to be custom tailored for specific applications" [32]. The early 1960's saw an increasing interest in HgCdTe (mercury cadmium telluride — MCT) alloys as they allowed detectors capable of detecting in the LIR range. The MCT detector family is one of the most thoroughly studied systems. 1967 saw the emergence of silicon detectors. The end of the 1950's and the beginning of the 1960's saw the introduction of narrow bandgap semiconductor alloys in III-V (InAsSb), IV-VI (PbSnTe) and II-VI (HgCdTe) material systems. Narrow bandgap semiconductors allow for very long wavelength detection (MIR and LIR). The attractive properties of these materials are high optical absorption and high electron mobility [7],[32]. Together with these properties, the scope for bandgap engineering through composition variation made these materials systems very attractive. It is mainly military applications that drove the research and development in infrared detectors. Even today, the major projects of infrared detection are being pursued by defense institutions. Next to them in the race are the industrial entrepreneurs seeking biomedical applications for infrared detectors. Both of them come with an added component of secrecy, for military, industrial and security reasons, which actually hinder the dissemination of ideas and inhibit collaborative works.

MCTs, QWIPs, QDIPs and Nanocrystals

At present the most popular IR detectors are MCTs, QWIPs (quantum well infrared photodetectors employing intersubband transitions and mostly based on GaAs/AlGaAs system), strained superlattices based on antimonides, high-temperature superconductors, pyroelectric detectors and bolometers (thermal detectors) and very recently QDIPs (quantum dot infrared photodetectors). The most popular and efficient among them are the MCTs. High absorption coefficient, high efficiency and low optical generation along with flexibility for optimized detection for broad range (1–25 μm) make MCTs very attractive [7]. But QWIPs are also very good competitors as MCTs suffer from being a hazardous material system and alloy instability (weak Hg-Te bond). Particularly the high vapor pressure of Hg makes it difficult to maintain a homogeneous composition over a large area which causes reliability issues for focal plane arrays [33]. These limitations led researchers to consider viable alternatives (e.g. III-V semiconductors). The alloy instability runs into "serious difficulties in repeatable growth of uniform-composition bulk crystals and epitaxial layers" [7]. Hence, issues concerning uniformity and yield need to be addressed.

The advantages of QWIPs compared with MCT detectors include the mature GaAs growth and processing technologies, which result in highly uniform, excellently reproducible large-area, low-cost arrays [34],[35]. In addition, the ability to accurately control the band-structure and spectral response allows monolithically integrated multispectral infrared detectors as well as the potential for monolithic integration with high-speed GaAs multiplexers and other electronics. The problems with QWIPs are their complicated fabrication and process technologies (in spite of the maturity of GaAs technology) and their insensitivity to normal light incidence. They also suffer from low conversion (or quantum) efficiency and high dark current. However, it was shown that as a single device QWIPs can never compete with MCTs above 70K due to fundamental limitations associated with intersubband transitions, and can only outperform them at an operating temperature of ~40K. However, for focal plane arrays in the LIR region, QWIPs are better than MCTs due to their high material quality [36].

Antimony-based strained superlattices (e.g. AlGaSb/GaSb or InAs/InGaSb type-II superlattices) are also suitable for LIR detection. The latter system has a few advantages over those of MCTs: a higher degree of uniformity (crucial for large arrays), a smaller leakage current (due to higher effective mass in superlattice), reduced Auger recombination and compatibility with GaAs-based electronics. InAsSb-based detectors are found to have better alloy-stability, higher electron/hole mobilities, and lower substrate cost (GaAs-substrate compatible) [2],[37].

A recent surge of interest has been seen in the area of quantum dots (QD) as there has been a growing literature on the different issues such as growth, carrier transport and optoelectronic properties of QDs. The QDIPs have the advantages of sensitivity to normal excitation illumination, three-dimensional confinement of the carriers ensuring lower dark current and decreased thermionic emission, possibility of high temperature operation along with photoconductive gain and higher detectivity [38],[39]. Their main disadvantage is that they have a reduced absorption coefficient [7]. A direct comparison of the limitations on dark current and detectivity in HgCdTe, QWIP and QDIP shows that QDIPs are expected to potentially rival and exceed the performance of HgCdTe detectors if QD arrays with good dot size uniformity become a reality [40]. Elsewhere, a recent review [39] shows that QDIPs can exhibit much higher responsivity than QWIPs due to lower capture probability and hence larger photoelectric gain. Higher responsivity is unfortunately accompanied by higher dark current, because it is amplified with the same gain. The QDIPs based on low-density arrays of relatively large QDs are expected to be inferior to QWIPs in detectivity. But those based on extremely dense arrays of small QDs, in which the bound electrons are really zero-dimensional, can significantly surpass QWIPs in detectivity [41], [41].

A new kind of detector consisting of *nanocrystals* involving a novel fabrication process has been reported. These "solution processed" nanocrystals have outperformed their epitaxially grown semiconductor competitors. It has been shown in [41] that detectivities (D*) as high as 5×10^{12} cmHz$^{1/2}$W^{-1} in the visible spectra (400-900 nm) and 10^{13} cmHz$^{1/2}$W^{-1} at 1.3 μm are possible with novel PbS based nanocrystals whereas the detectivity was only 10^{12} cmHz$^{1/2}$W^{-1} for epitaxially grown InGaAs [42]. Usually a higher value of D* is preferred, since the reciprocal of D* gives a measure of minimum detectable signal power.

Thermal Detectors

A thermal detector operates by absorbing incident radiation to change its temperature and "the resultant change in some physical property is used to generate an electrical output" [32]. The signal, however, does not depend on the photonic nature of the incident radiation and hence thermal effects are generally wavelength-independent: the signal depends upon the radiant power but not upon its spectral content. Generally speaking, these detectors are of modest sensitivity and slow response, but of very low cost and easy to use. *Bolometers* utilize variation of electrical conductivity to detect incident light and are not good for high speed detection and imaging. Tremendous research and development has been done on Si-bolometers as they now have the lowest unit cost and are compatible with standard 8" Si-processing [7]. Among the promising materials to be used as bolometers are amorphous silicon and superconducting, semiconducting and amorphous YBaCuO thin films on Si. Depending on the material, these bolometers can be operated in both cooled and uncooled forms. The superconducting YBaCuO gives a better sensitivity, but with liquid nitrogen cooling. Those based on amorphous silicon or vanadium oxide (VO_x) compounds do not require cooling but come with a larger decrease in temperature coefficient of resistance [43]. Amorphous silicon has a high $1/f$ noise which degrades sensitivity and vanadium oxide, having improved sensitivity though, suffers from difficult growth procedures. Semiconducting YBaCuO is claimed to have a better responsivity than those of superconducting form and pyroelectric detectors [43]. A change of temperature in a pyroelectric crystal results in a change of spontaneous polarization that induces surface charge in a particular direction — the working principle of *pyroelectric detectors* [7]. Hence, the choice of material for a pyroelectric material is not an easy task as it incorporates many physical parameters and their subtle interdependence. One important limitation with pyroelectric detectors, in spite of their popularity, is that they have to be operated with optical modulators (i.e. choppers). Lead-based oxides (e.g. $PbTiO_3$ or $Pb(ZrTi)O_3$) are the common choices for pyroelectric detectors.

Thermopile detectors, though having only limited imaging applications, are well suited for some low-power applications, are highly linear, require no optical chopper, and have detectivity values comparable to resistive bolometers and pyroelectric detectors. They operate over a broad temperature range with little or no temperature stabilization. However, their responsivity is orders of magnitude less and thus their applications in thermal imaging systems require very low-noise electronics to realize their potential performance. They are employed as linear arrays that are mechanically scanned to form an image of stationary objects. The wide operating-temperature range, lack of temperature stabilization and radiometric accuracy make thermopiles suitable for space-based scientific imaging applications [7].

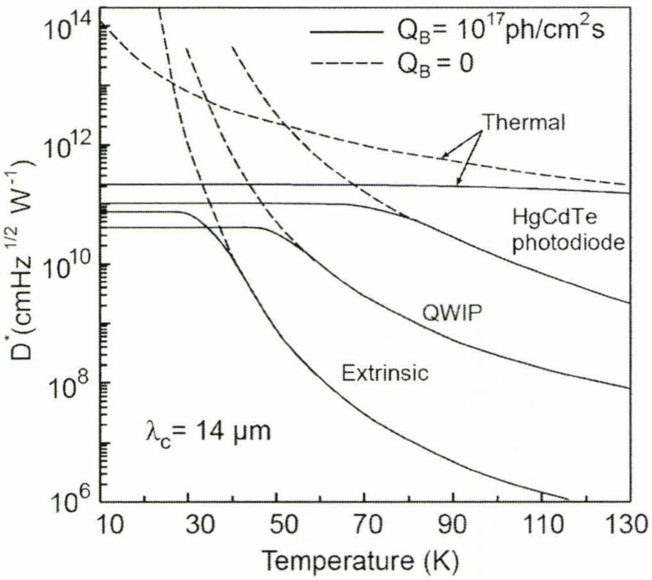

Figure 1.6: Comparison of various detector technologies [7].

Figure 1.6, reproduced here from [7], shows at a quick glance the comparative behavior of different detectors at a certain wavelength (14 μm) with and without background photons. From this figure, several observations can be made [7]. First, thermal detectors have excellent thermal stability. Second, among photon detectors MCTs outperform all others (even with background limited operation). Third, at room temperature the performance of the thermal detectors is much better than other detectors. Fourth, with the absence of any background photons at very low temperatures, photon detectors are better than the thermal ones. Also, it is suggested that as the wavelength of operation goes higher, thermal detectors become the preferred one —the photon detectors are preferable at long wavelength infrared with low operating temperatures and thermal detectors are preferable at very long wavelengths. This is attributed to the different dependences of the detectivities (or sensitivities) on wavelength and temperature which is again due to the fundamental difference of the nature of the noise for these two types of detectors (dominance of generation-recombination noise in the former and temperature fluctuation noise in the latter).

1.5 Scope and Outline of the Thesis

Metamorphic growth technology is a useful way, in principle, to grow semiconductor epilayers of any composition applicable to the device designer's intended application, on any substrate. Optoelectronic integrated circuits (OEIC) have been successfully demonstrated on GaAs substrates which include both the photodetector and an amplifier (HEMT) in the same dye. This reduces the cost and serves as a compact front-end component for a complete receiver system. The present thesis demonstrates that this growth technique can be extended to include the 6.1 Å family's most important member – gallium antimonide. Commercially available substrates are limited to 6-inch GaAs and 4-inch InP substrates. In order to grow device layers and 'bandgap engineer' their properties for applications in the mid infrared region, the designer needs to either grow his own substrates (cost ineffective) or grow lattice mismatched layers (resulting in highly strained systems). The metamorphic growth technology provides a way to solve this dilemma by growing buffer layers which are compositionally graded (either linearly or in small steps) and thus allowing a metamorphic terminal layer to be used as a pseudo-substrate for further growth of active device layers. The substrate used can be one of the routinely available substrates and thus ensuring a cost-effective fabrication process.

Scope

The present thesis successfully demonstrates that metamorphic growth is possible with the antimonides, by growing GaSb metamorphic layers on InP substrates using GaAsSb buffer layers. GaAsSb metamorphic layers were grown as a 'proof of concept' for the feasibility of growing and characterizing Sb containing metamorphic layers with a long term plan of fabricating diodes metamorphically on InP or GaAs substrates. GaAsSb layers are also attractive for use in HBT applications [44]. After successful growth and characterization of this M-layer, the metamorphic technology was then extended to another ternary, i.e. InGaSb, with a view to be able to fabricate detectors for mid-infrared.

It was demonstrated in the present thesis that good-quality photodetectors can be fabricated on a metamorphic layer of InGaSb grown on GaSb. InGaSb has many promising applications in photodetectors [45]-[47] and lasers [48],[49].

The first step towards fabrication process is to investigate the etching processes. We have investigated the reactive ion etching of GaSb thoroughly by changing various control parameters (e.g. microwave and rf power, gas ratio, chamber pressure). The gas mixture used is methane-argon-hydrogen, which is very popular with InP-based dry etching. This study shows that one can use the existing set-up for InP processing and do not need to make costly adjustments for corrosive chlorine-based gases for example. The resulting etching rates are reproducible and highly vertical mesa sidewalls and good surface morphology has been demonstrated.

The growth and characterization of InGaSb layers, suitable for fabrication of a photodetector with a long wavelength cut-off > 2 μm, were carried out and the effects of growth temperature on the quality of the metamorphic layers investigated. Our findings suggest that with a growth temperature higher than 500^{o} C, the threading dislocations propagating through the top metamorphic layer are reduced; the dislocation density and the surface roughness are also reduced.

Active homojunction device layers were then grown on this metamorphic platform. The diodes were characterized under dark and illuminated conditions. Also, the effect of surface passivation by silicon nitride and polyimide has been investigated suggesting that the former is better. The theoretical study shows that both at room temperature and 90^{o} C, the dark current of the diodes is dominated by surface leakage. The area and perimeter components of this leakage current have been extracted.

The responsivity for one of these diodes ($In_{0.18}Ga_{0.82}Sb$) was measured with a cut-off at 2270 nm. The detectivity was calculated and its dependence on temperature and bias was investigated. Finally, the electron and hole ionization coefficients were extracted from these diodes. We have found that for $In_{0.10}Ga_{0.90}Sb$, both at room temperature and 90° C, electron ionization coefficient dominates over hole ionization coefficient. The excess noise figure for these diodes is below 4 at room temperature nominal gains up to 10. This implies that avalanche photodiodes made out of InGaSb will not introduce excess noise if implemented in a receiver system, since the lower the excess noise figure the better would be the signal-to-noise ratio of the avalanche photodetector.

The research work presented in this thesis has resulted in three published articles:

- F. M. Mohammedy, O. Hulko, B. J. Robinson, D. A. Thompson and M. J. Deen, "Effect of growth temperature on InGaSb metamorphic layers and the fabrication of InGaSb p-i-n diodes," *J. Vac. Sci. Technol. B,* **26,** p.636-642, (2008).
- F. M. Mohammedy, Z. L. Peng, D. A. Thompson and M. J. Deen, "RIE of GaSb with an ECR source using Methane/Hydrogen chemistry in an Argon plasma," *J. Electrochem. Soc.,* **154,** p.H127-H130, (2007).
- F. M. Mohammedy, O. Hulko, B. J. Robinson, D. A. Thompson, M. J. Deen and J. G. Simmons, "Growth and characterization of GaAsSb metamorphic samples on an InP substrate," *J. Vac. Sci. Technol. A,* **24,** p.587-590, (2006).

Outline

The thesis has altogether seven chapters. Chapter 1, above, discussed the emerging field of antimony materials and their closest kins in the 6.1 Å family, possible applications in the mid-infrared wavelength, the literature review on metamorphic layer growth technology and a comparison of some detector technologies.

Chapter 2 discusses the calibration issues regarding the MBE growth of the layers used to fabricate the devices described in this thesis. Groups-III (In, Ga), -V (As, P, Sb) and dopant (Be, GaTe) cell calibrations are discussed. Wet and dry etching issues in GaSb are discussed in Chapter 3. Also described are the details of the reactive ion etching study that was done on GaSb.

Chapter 4 discusses the growth and characterization of metamorphic layers. The x-ray diffraction analysis is discussed to explain how the lattice constant measurements were carried out. This is followed by the description of the growth and characterization of GaAsSb layers. This demonstrated the 'proof of concept' of the metamorphic growth technology for antimony containing material. Afterwards, the growth and characterization of the InGaSb layers grown on GaSb substrate and the growth temperature dependence of the quality of the InGaSb metamorphic layers are discussed.

Chapter 5 discusses the fabrication of homojunction diodes on InGaSb metamorphic layers. The details regarding the dark current measurements, the extraction of the area/perimeter components of the leakage current, temperature dependence of the dark current and its comparison with other published results are described in this chapter. This chapter also includes the theoretical modeling of the dark current components.

Chapter 6 describes all the optoelectronic characteristics of the diodes. The responsivity measurements and the calculation of the detectivity and its temperature and bias dependence are given. This chapter also includes a small survey of the ionization coefficient measurements done in the antimonide materials and concludes with a section on the details of the extraction of ionization coefficients and their temperature and composition dependence.

Finally, Chapter 7 concludes the thesis with a synopsis of the major findings of the present research and suggested improvements and possible extension to future research projects. Appendix 1 lists the important material and device parameters for InGaSb. Appendix 2 discusses important lithographic steps useful for the diode fabrication.

Chapter 2 MBE Operations

This chapter discusses the operational fundamentals of the molecular beam epitaxy (MBE) machine used in this research. The calibration issues of the various elemental sources are also discussed. Calibration is a routine procedure to ensure the machine's reliable and repeatable operation for various growth requirements and to adjust for the flux variations due to cell drifts. This guarantees that the required composition and doping levels are maintained in the epilayers. The results obtained in this study were then applied for the growths discussed in Chapter 4 and Chapter 5.

2.1 Epitaxy

Epitaxy refers to the growth of a crystal layer (epitaxial layer or epilayer) upon a host crystal (substrate) in an ordered fashion. In other words, the symmetry between the contacting crystal planes must be respected. The word 'epitaxy' means "ordered upon" from Greek roots. Hence, the 'law of epitaxy' can be stated according to its earliest proponent L. Royer, who first coined the term 'epitaxy,': "Epitaxy occurs only when it involves the parallelism of two lattice planes that have networks of identical or quasi-identical form and of closely similar spacings" [50]. In molecular beam epitaxy, the mean free path between the sources and the substrate is large enough so that the impinging atomic or molecular fluxes are ballistic in nature. This condition is achieved by maintaining the growth chamber at an ultra-high vacuum. MBE is a versatile technique for growing epitaxial layers typically ranging in thickness, from 1 nm to several thousand nm's. The advantages of MBE include precise control of beam fluxes and growth conditions [44]. Controllable shutters are available at the opening of each effusion cell inside the growth chamber. This allows the beam to be shut on or off very quickly making possible the growth of abrupt heterostructures. Also available are several in-situ surface diagnostic techniques e.g. reflection high energy electron diffraction, optical pyrometer, beam flux monitor. Elemental beams of group-III elements (Al, Ga, In) and dimeric (or tetrameric) beams of group-V elements (P, As, Sb) flow toward the substrate and nucleation begins on the surface. This is a non-equilibrium growth process. The growth temperature is substantially lower than the beam flux temperature and the growth rate is slow (typically ~1 μm/h or 1 monolayer/s).

The Gas Source Molecular Beam Epitaxy (GSMBE) facility was designed and manufactured by SVT Associates, USA (Figure 2.1). The MBE has ten cell-ports – Group III (In, Ga, Al) effusion cell-ports, group-V (Sb, AsH_3/PH_3) cracker cell-ports, dopant (GaTe, Be, Si, CBr_4) cell-ports, an inductively-coupled rf plasma port and one extra port for future expansion. All the cells are located along the bottom edge of the growth chamber (Figure 2.1 (b)) aiming up toward the center where the rotating substrate holder is placed.

The MBE system consists of a stainless steel loading chamber, a transfer and preparation chamber, and a growth chamber. The MBE growth chamber is maintained at ultra high-vacuum using a combination of turbo pumps and cryopumps. Liquid nitrogen cryopanels surround the interior of the growth chamber to minimize re-evaporation from the internal walls and maintain thermal isolation between the cells. This ensures the purity of the epilayers. The base pressure is in the $\sim10^{-9}$ Torr range. This MBE system used a vertical geometry with the sources arranged to provide an upward directed flux upon a downward facing substrate. The sample was placed in a recessed opening in a molybdenum platter and held in place by gravity. Substrate rotation of ~ 15 rpm about an axis normal to its surface was provided to ensure uniform layer thickness, composition and doping.

The substrate temperature, during the cleaning and growth, is measured using infrared pyrometry: a two-channel (950 nm and 850 nm) SVTA IS4K optical pyrometer with a built-in reflectometer. Subsequent temperature measurements on different wafers are performed using the single channel at 950 nm with the emissivity appropriate to that wafer. A thermocouple in the proximity (within 2 mm) of the back surface of the substrate-holder is also present and is used in conjunction with the pyrometer to monitor the growth temperatures.

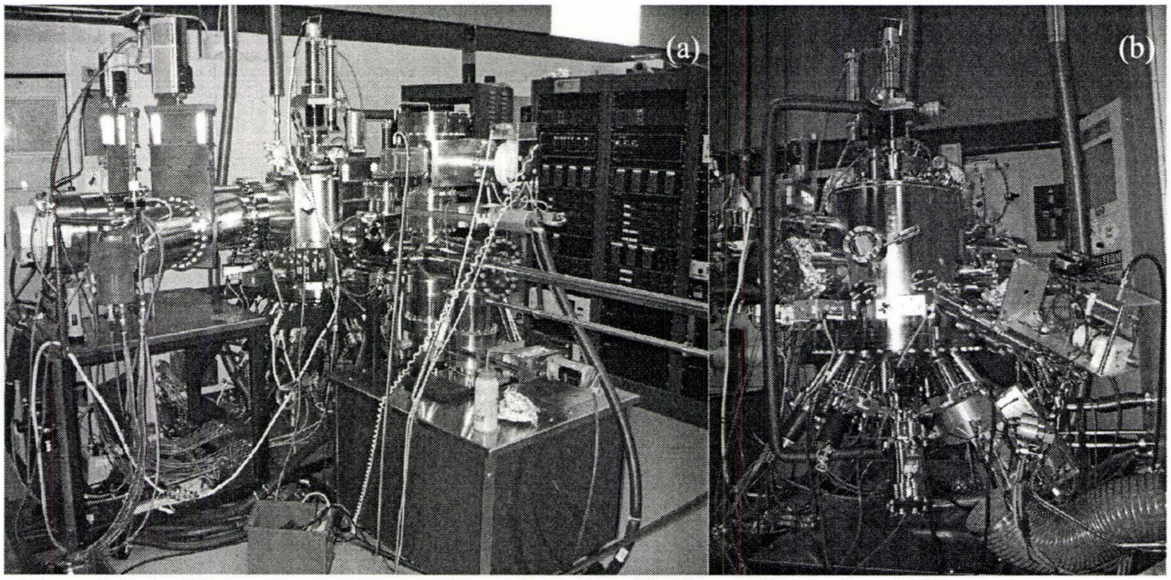

Figure 2.1: (a) The molecular beam epitaxy facility at McMaster University. (b) Shows the vertical growth chamber along with various effusion cells.

2.2 Calibration of the Group-III Cells

Standard solid-source effusion cells are available for all the group-III elements (indium, gallium, aluminum). For the purpose of this research project, only gallium (Ga) and indium (In) cells are used. The source cells have conical-shaped and chemically inert pyrolytic boron nitride crucibles to hold the high-purity indium and gallium metals. Resistance-heating is provided to increase the vapor pressures of elemental Ga and In. Under the ultra-high vacuum pressure maintained at the growth chamber of the MBE, these elemental vapors then effuse from the cell apertures into the chamber. The fluxes are controlled by controlling the cell temperature which is done by programmable Eurotherm® PID controllers. These effusion cells are designed by the MBE manufacturer

SVTA. Each cell is equipped with an external shutter that can be pneumatically controlled to start or stop any desired flux.

Figure 2.2 shows the change of flux with the In and Ga cell temperatures measured by a flux monitor temporarily inserted in place of the substrate holder. Group-III beam fluxes can be calibrated against film thickness measurements since the growth rate is proportional to the group-III arrival rate [51]. The temperature dependence of the impinging fluxes is given by:

$$\phi_{T_1} = \phi_{T_2} \exp\left\{\alpha\left(T_1 - T_2\right)\right\} \Rightarrow \ln\frac{\phi_{T_1}}{\phi_{T_2}} = \alpha\left(T_1 - T_2\right) \tag{2.1}$$

where $\phi_{T1,T2}$ are the fluxes at temperature T_1 and T_2, respectively. Figure 2.2 shows the plot of the logarithmic Ga and In fluxes as a function of the cell temperatures according to eq.(2.1) where ϕ_{T2} is considered as background flux. The slope α is determined from curves in Figure 2.2 for temperatures between T_1 and T_2. Growth rates can be corrected by using eq.(2.1) if the rate at any other temperature is known.

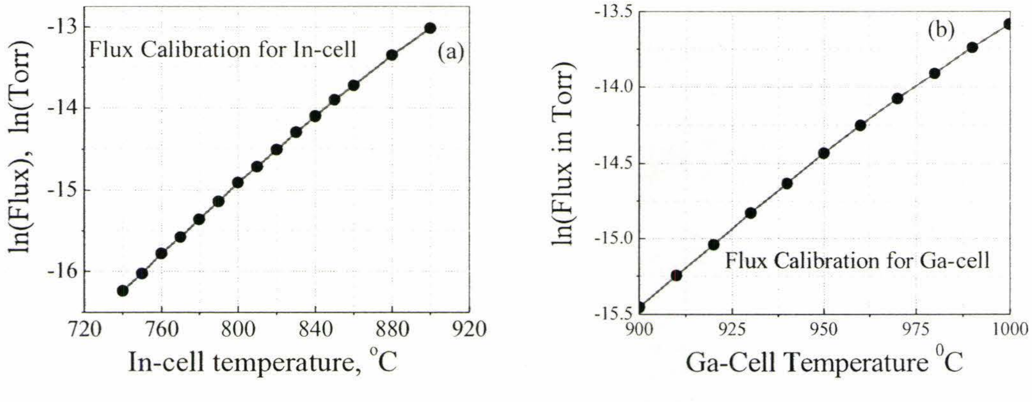

Figure 2.2: Typical indium (a) and gallium (b) fluxes at corresponding cell temperatures.

Typical calibration samples of InP or GaAs are routinely grown at a rate of 1.0 μm/hr. Thickness measurements on these epilayers by Alpha-step profilometers provide the growth rates of In and Ga, respectively. Group-III fluxes are then calibrated by adjusting the cell temperatures according to the desired growth rate and layer composition when two or three group III elements are used for the desired layer. Group-III cells are generally calibrated as part of the routine calibration of the machine and for each new growth request. The day-to-day incremental drift in calibration points is due to the depletion of the source material.

2.3 Calibration of the Group-V Cells

The MBE used for this work utilizes gas sources for arsenic and phosphorus and a solid-source effusion cell for antimony. Arsine (AsH_3) and phosphine (PH_3) are used as source-gas for As and P, respectively. Among the group-V sources, the antimony-source is the most difficult to control.

Arsenic and Phosphorus

Gaseous hydrides (AsH_3 and PH_3) are used to provide As and P. Gas sources are very efficiently controllable but not easy to handle. There are important maintenance and safety issues that are of concern. These hydrides are allowed to flow simultaneously over a filament and are cracked at about 1000^o C to provide As- and P-dimer species. These dimers dissociate while bonding to the group III atoms on the sample surface [105]. The gases are delivered to the growth chamber using a gas-handling system that uses a baratron-based pressure control system. The baratron gauges measure the differential pressure created by the flow of gas species that causes a change in the capacitance in the gauge. In order to calibrate these flow-rates, the beam equivalent pressures (BEP) of the resulting hydrogen, derived from cracking the hydrides, are measured against the baratron readings by inserting an ion-gauge flux monitor at the substrate holder position. The ion gauge measures the beam pressure resulting from the flow from a source-cell with an open shutter. This is shown in Figure 2.3 (a). The solid lines are third-order polynomial fit to the data points. The BEP for phosphine measured at 10 torr (baratron monitor) is normalized to give a flow-rate of 7.0 sccm according to the diameter of the orifice in the gas flow element. This ratio (7.0 sccm / BEP of PH_3 at 10 Torr) is then used to normalize both arsine and phosphine BEP. The resulting calculated flow-rate versus baratron readings are shown in Figure 2.3 (b). This is a very important curve to convert required flow-rates into baratron pressure readings and is frequently used for growths requiring As and/or P.

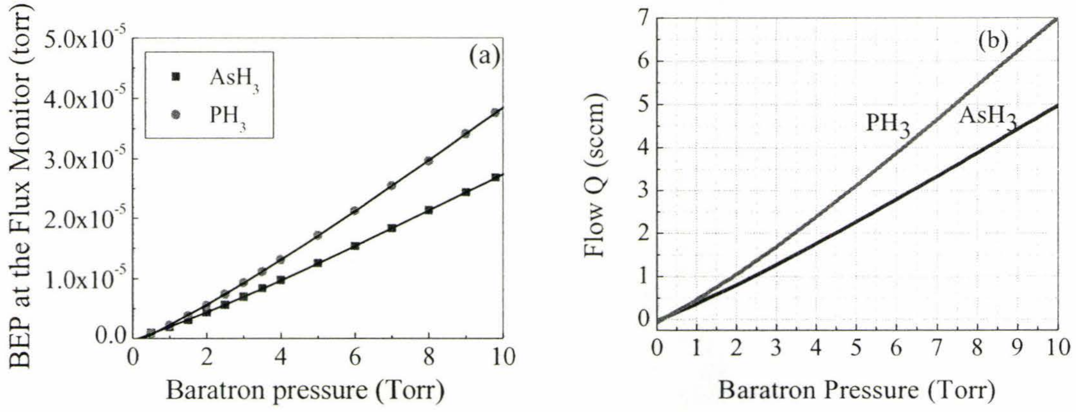

Figure 2.3: (a) Beam equivalent pressure and (b) the calculated flow-rates of the gas sources.

Antimony

The low vapor pressure of antimony makes it one of the "nuisance" elements for MBE. During crystal growth, antimony possesses low surface mobility and the atoms tend to aggregate together forming clusters and precipitates [2]. This leads to antimony antisites (Ga_{Sb}). This property of antimony having a low vapor pressure makes the antimony cell very difficult to calibrate. Also, parameters for growths not requiring antimony are affected by previous runs using the antimony source. This is because antimony coats the interior wall of the chamber resulting in a background Sb flux on the substrate leading to some unwanted incorporation until the walls have been sufficiently covered by subsequent growths. It also makes temperature calibrations difficult since the Sb coats the substrate-holder, the mirror and window used by the pyrometer.

Typically, elemental antimony is used to produce Sb_4 vapor, where either the tetramer is used directly for the epitaxial deposition, or a cracker is attached to dissociate the tetramer into the dimer Sb_2 or the monomer Sb_1 [53] as is done here. Also the corrosive nature of antimony vapor makes the long-term use of any metallic crucible or valve unpredictable [52]. The valve body of the present antimony cell is of molybdenum with a tungsten needle acting as a valve. The antimony effusion cell, used in the present system, is a valved-cracker consisting of a body containing the pyrolytic boron nitride coated crucible, a valve and the cracking tube (see Figure 2.4). The cell was designed by the manufacturer SVTA and is controlled using custom-made software supplied by the manufacturer to operate the valve closing and opening. The temperatures of the three parts of the cell are controlled with Eurotherms®.

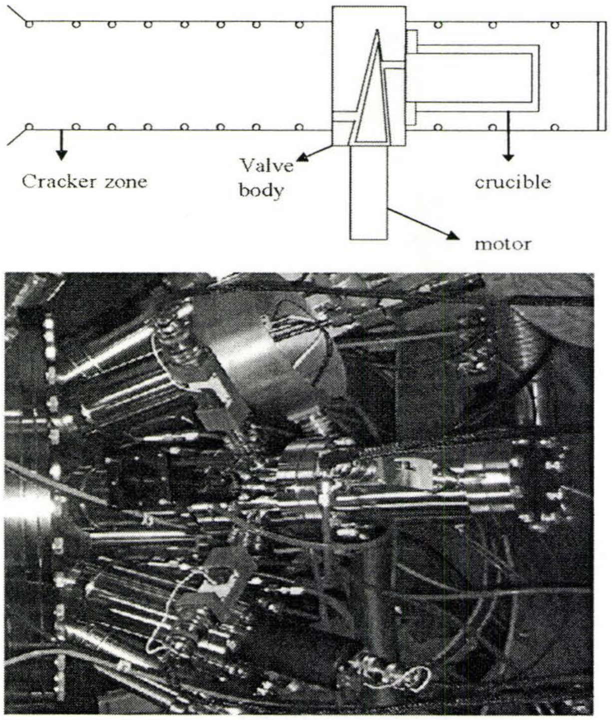

Figure 2.4: Antimony cell: Schematic and real life.

For good-quality film growths, it is important to ensure that antimony vapor is cracked to produce Sb_1 or Sb_2 species [53],[54]. A degassing cycle was followed before every operation of the Sb-cell — ramp up the cracker and valve to 1000° C and 725° C respectively, after a 10 min delay the Sb-crucible is ramped up to 625° C for 10 min. They are then reduced to the operating temperatures of 925, 675 and 580° C, respectively. The cracking temperature 925° C is chosen to ensure that Sb_1 and Sb_2, rather than Sb_4, are the dominant species incident on the substrate. Sb_1 and Sb_2 doesn't affect the electrical properties (Hall mobility) but results in poorer optical quality of the epilayers [53]. This cracking temperature is also suggested by [54] to obtain Sb-monomer in MBE. As the cracking temperature is increased, the dominant species reaching the substrate becomes monomeric, and hence the measured Sb-flux dramatically drops. We have observed a similar but small drop in the flux as the cracker temperature was ramped up (see Figure 2.5 (b)). The observed decrease in flux is caused by molecule decomposition due to the smaller ionization probability and smaller molecular mass of the cracked species [53]. The operating temperature for the present machine is chosen empirically to give an optimum Sb-pressure at the substrate measured by a flux monitor so that at a certain valve position we get an appropriate Sb-flux (ϕ_{Sb}~1.88×10^{-6} Torr) on the substrate.

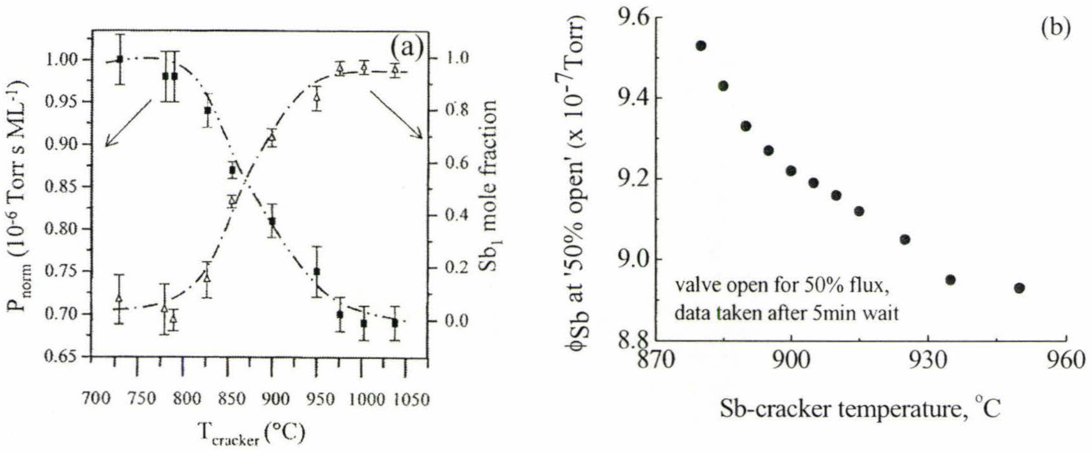

Figure 2.5: Cracker temperature for Sb_1-species. (a) The behavior of the Sb-flux BEP as Sb changes from Sb_2 to Sb_1 [53]. (b) Shows our attempt to reproduce a similar trend in Sb-flux as the cracker temperature was increased.

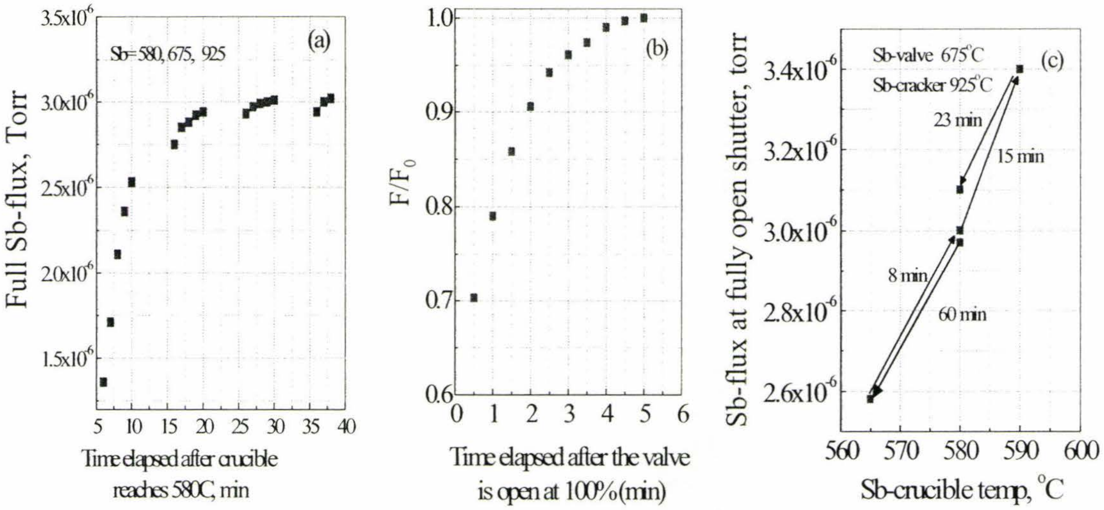

Figure 2.6: (a and b)Two time-delays and(c) the flux hysteresis in Sb-cell operation.

There are at least three time-delays involved in the Sb-cell operation — one delay after the degassing cycle (~30 min) (shown in Figure 2.6 (a)), another delay after opening the valve to 'full open' (5–10 min) (Figure 2.6 (b)), and a final one after the shutter is open (~30 sec). The first delay is the time required by the elemental source to reach thermal equilibrium with the Sb-crucible. There were several pauses during this measurement as is seen by the punctuated flux in Figure 2.6 (a). During each pause, both the shutter and the valve were closed. When they were opened, the flux had to fill up the cracker tube (the second type of delay referred to in Figure 2.6 (b)) which takes about 5-6 min. therefore the starting value of the flux after opening the shutter was slightly lower than when the pause was made. The second delay is due to the finite time required to fill up the cracker zone/tube (see schematic in Figure 2.4). There are additional complications involved in the Sb-cell operation: (i) adjustment of the flux depends on the previous temperature history of the cell — if the cell is cooled from a hotter temperature the ϕ_{Sb} is higher than usual as is evident in Figure 2.6 (c); (ii) based on the previous usage history, if the valve had been opened fully and then closed for considerable time, ϕ_{Sb} takes a longer time to reach the desired level, but if the valve was opened immediately previous then it takes a shorter time to reach the steady-state flux. This dependence on prior history is operationally important and has to be taken into consideration during growths. The curve in Figure 2.7 shows the relation between ϕ_{Sb} (BEP of Sb on the substrate as measured by a flux monitor) and the valve position. This is the operating curve we used for the antimony cell. One can use this curve to determine the operating valve position according to the desired flux for intended operation. In a typical growth day, we move the valve to a predetermined position for a desired level of flux, then adjust this position till the desired flux is obtained and then record the valve position.

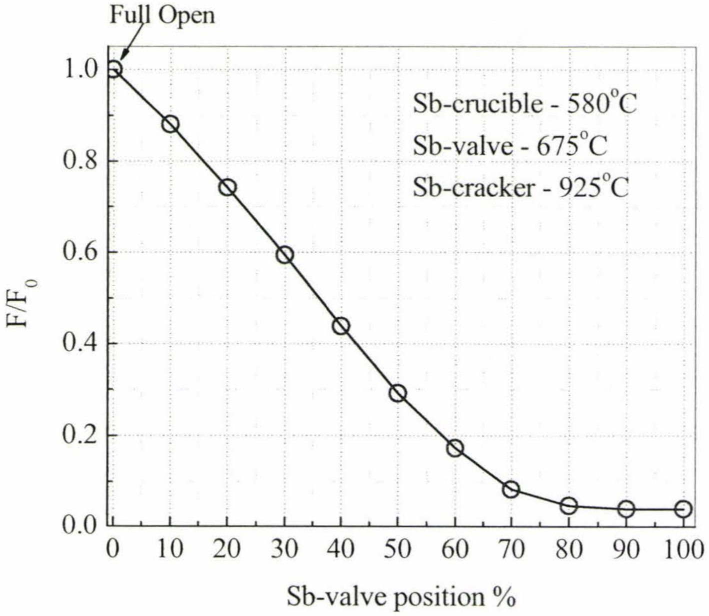

Figure 2.7: Flux variation with the valve position for Sb-cell.

We make use of the Foxon-Joyce equation [54] to estimate the Sb-flux for a growth-rate of 1 monolayer per second (1.0 ML/s) and it is [55]:

$$\frac{J_X}{J_Y} = \frac{\phi_X}{\phi_Y}\frac{\eta_Y}{\eta_X}\sqrt{\left(\frac{T_X}{T_Y}\frac{M_Y}{M_X}\right)} \tag{2.2}$$

$$\frac{\eta}{\eta_{N_2}} = \frac{0.4Z}{14} + 0.6 \tag{2.3}$$

where J_X is the flux, ϕ_X is the BEP, T_X is the cell temperature in absolute scale, M_X is the molecular weight of species of X. By inserting the movable ion gauge temporarily in place of the substrate holder, and from a measure of the beam-on to beam-off pressure the relative flux of each beam can be estimated, [55]. Relative fluxes are then calculated from these relative beam pressure measurements according to eq.(2.2). The ionization efficiency (η) of the species is relative to N_2, and is given by eq.(2.3), whose atomic number is Z. The flux monitor was calibrated for indium flux by growing layers of InP on InP at a nominal growth rate of ~ 1.0 μm/hr (~0.95 ML/s). For a typical growth of InP, the indium cell-temperature is ~ 855° C. According to Figure 2.2, this cell temperature produces a net In-flux of ~1.06×10^{-6} Torr. This In-BEP is then used in eq. (2.2), corrected for the difference in ionization coefficient between In and Sb through eq.(2.3) and for Sb_1 species, to calculate the corresponding Sb-BEP (1.53×10^{-6} Torr; cracker at 925°C) to give 1.0 ML/s flux. An Sb overpressure is necessary to improve the epilayer quality by reducing Ga_{Sb} antisite defects [2]. To ensure an adequate overpressure, a BEP of 1.88×10^{-6} Torr was empirically fixed to yield ~1.23 ML/s on InP. This pressure corresponds to an antimony flux of 1.3 ML/s on GaSb after correcting for the difference in lattice constant.

2.4 Calibration of the Dopant Cells

This section describes the calibration of cells used for doping with tellurium (using a gallium telluride source) and beryllium. GaAs and GaSb layers were grown on semi-insulating GaAs substrates (due to the lack any commercially available semi-insulating GaSb wafers). It has been reported that, in spite of a large mismatch, GaSb layers grown on GaAs are relatively free of dislocations and are of “good crystalline quality” and that the transport in GaSb is unaffected [56],[57]. The layers were characterized by standard Hall-effect measurements [58],[59] to determine the dopant densities and mobilities at room temperature. Small square samples (few mm’s) were cleaved out of the samples grown and the resistivity of the samples were measured according to the standard Van der Pauw technique. The layer thicknesses for these measurements were designed by considering the effects of depletion depth due to surface states and band-bending at the interface of the doped layer and the semi-insulating substrate.

The depletion potential due to surface band-bending is given by [60]:

$$V_{bs} = \phi_s - \left\{ \frac{E_g}{2q} - \frac{kT}{q} \ln \frac{n}{n_i} \right\} \tag{2.4}$$

here E_g is bandgap, n_i is the intrinsic carrier concentration, and n is the doping level. The Fermi level of the free surface states is pinned to ϕ_s below the conduction band.

The width of the surface depletion layer is then defined as [60]:

$$l_s = \sqrt{\frac{2\varepsilon}{q} \frac{V_{bs}}{n}} \tag{2.5}$$

For GaSb, the surface states are at 0.3 eV for p-type and 0.625 eV for n-type below the conduction band [60],[61]. Using the parameters for GaSb in Appendix 1, equations (2.4) and (2.5) are used to determine the surface depletion layer thickness as a function of carrier concentration. The results of these calculations for n and p-type surfaces are shown in Figure 2.8. A similar formulation is available for the band-bending due to free carrier diffusion from the doped epilayers being trapped by deep trap levels in the semi-insulating substrate. This depletion width is l_t for deep traps at ϕ_t below the conduction band. There is not a large difference between the two depletion widths, $l_s \approx l_t$. Thus the doped epilayers were grown of such thickness that the effects of the surface states and band bending due to semi-insulating substrate are less than 10% of the total nominal thickness.

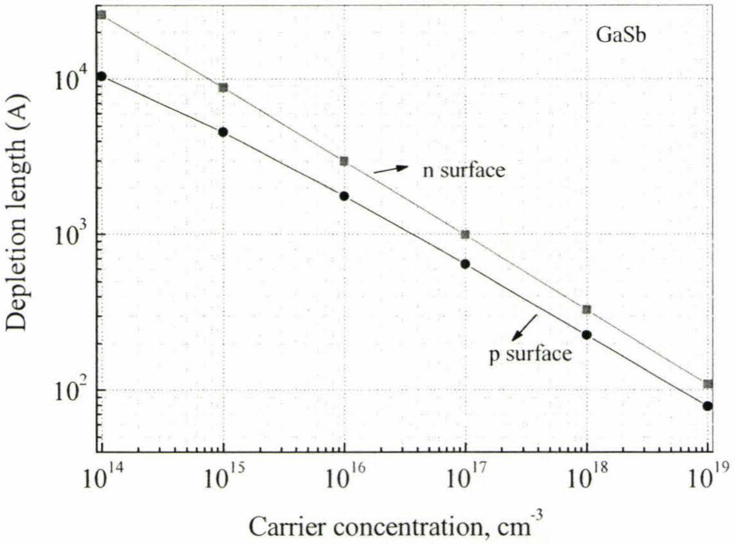

Figure 2.8: Surface depletion depth for n- and p-type GaSb.

Gallium Telluride Cell Calibration

For n-doping, there are reports [62] of various sources that can be used, e.g. GaTe, PbSe, PbTe and SnTe. The n-doping cell in our machine consists of two separate components – the crucible housing a source of GaTe and a cracker tube. The cracker tube temperature is chosen to be high enough so that elemental Ga and Te are separately incident on the substrate. A tube temperature lower than 850° C resulted in a low doping density, hence the cracking temperature was fixed at 850° C for all results reported in this thesis. Figure 2.9 shows the donor densities measured at room temperature for GaAs and GaSb. Figure 2.10 shows the corresponding electron mobilities measured at room temperature. A comment on the GaAs samples with cracker tube at 750° C in Figure 2.9 (black squares): The cracker tube was degassed at around 850° C and the crucible was held at 600° C during most of the time before the growth for this case. Crucible temperature was lowered just before the growth started. Since the crucible was held at quite a high temperature, there is a possibility that considerable residue would remain in the cracker tube. Also, the cracker was not properly degassed at even a higher temperature. This might contribute to the measured doping density for these samples which would otherwise be lower. For cracker temperature of 850° C, the degas was 'hard' enough to ensure that there were no residues in the cracker.

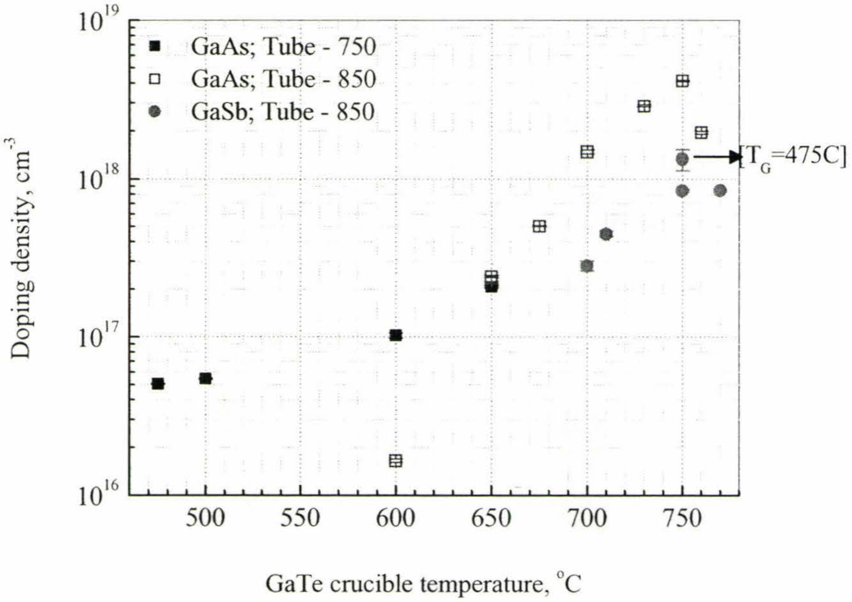

Figure 2.9: Donor doping density for GaAs and GaSb at room temperature.

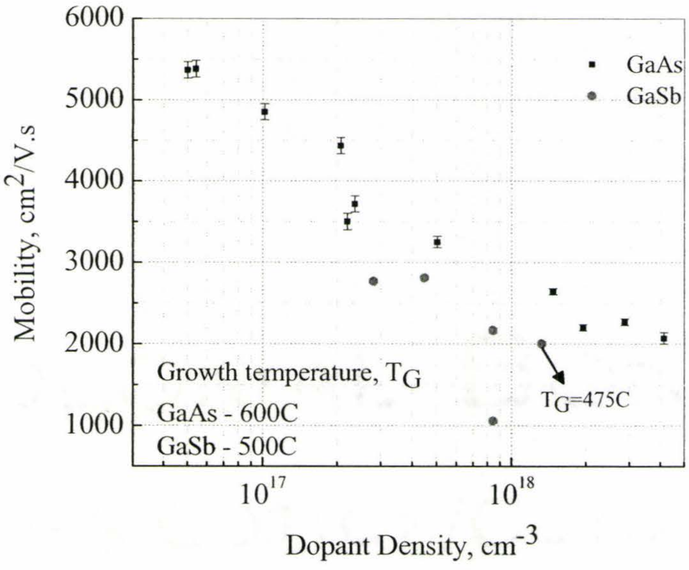

Figure 2.10: Electron mobility of GaAs and GaSb as a function of donor doping density.

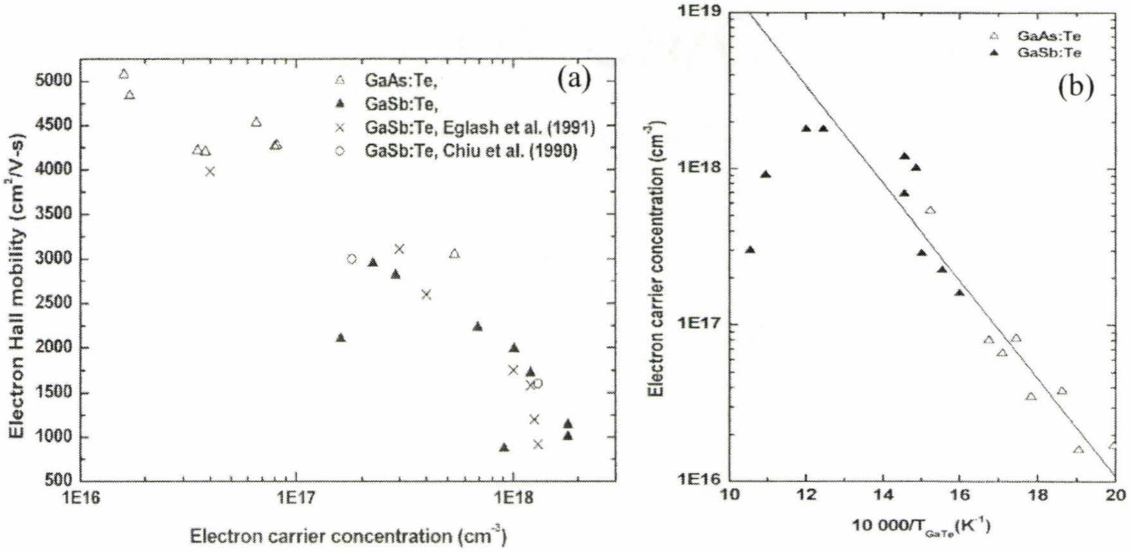

Figure 2.11: (a) Electron mobility vs donor concentration observed in other MBE groups. The triangular data points taken from ref [66]. (b) Carrier saturation beyond 2×10^{18} cm^{-3} has been observed in reference [66] for a one-stageGaTe-cell.

At a high crucible temperature (at 750° C and above in the present case) and at one growth temperature, the donor density seems to saturate (see Figure 2.9) and does not increase any further. This saturation effect of the carrier concentration and consequently the decrease of the mobilities at high carrier concentrations for Te doping has been reported in the MBE literature [62]-[67] and is shown in Figure 2.11 for other MBE research groups. We have grown one sample at a lower temperature (475° C) and have observed the increase in donor density (see Figure 2.9). This shows a possible dependence of donor densities on growth temperature as well. The donors' saturation behavior can either be explained [75] by the two-band theory according to which electrons are distributed among the Γ- and L-bands and hence the Hall concentration shows a saturating tendency (Figure 2.13); or by the inhomogeneous incorporation [76] of Te in GaSb layers possibly caused by native defects. Also, the presence of a high density of native defects in GaSb (dominant Ga_{Sb} antisites) [72],[73] possibly affects the donor incorporation as well. Further research needs to be done to identify the exact cause of this donor density saturation behavior. However, a similar dopant saturation effect has been reported [74] for Be doping in InP where the hole concentration saturates at around 2×10^{18} cm^{-3}.

There is an additional complexity in calculating the donor densities in GaSb. The L-band in GaSb is very close to the Γ-band and is only separated by 0.09 eV. Hence, at room temperature most of the electrons are found in the L-band (see Figure 2.12). So the Hall concentration gives only a weighted average of the two densities in the two bands and hence is an underestimate of the actual donor concentration.

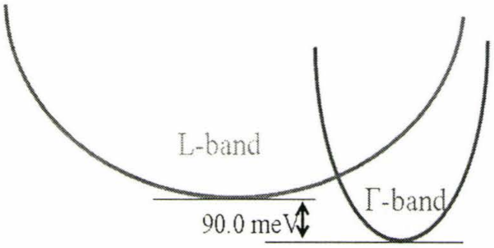

Figure 2.12: Relative position of L-band and Γ-band in GaSb.

This problem has been discussed in [64],[68]-[71], and more recently in [75]:

$$\mu_{\text{Hall}} = \mu_\Gamma \left[\frac{1 + F \dfrac{n_L}{n_\Gamma}\left(\dfrac{\mu_L}{\mu_\Gamma}\right)^2}{1 + \dfrac{n_L}{n_\Gamma}\dfrac{\mu_L}{\mu_\Gamma}} \right] \text{ and } n_\Gamma = n_{\text{Hall}} \left[\frac{1 + F \dfrac{n_L}{n_\Gamma}\left(\dfrac{\mu_L}{\mu_\Gamma}\right)^2}{\left(1 + \dfrac{n_L}{n_\Gamma}\dfrac{\mu_L}{\mu_\Gamma}\right)^2} \right] \tag{2.6}$$

$$\frac{\mu_\Gamma}{\mu_L} = 5 \tag{2.7}$$

$$\frac{n_L}{n_\Gamma} = \frac{N_C(L)}{N_C(\Gamma)} \frac{F_{\frac{1}{2}}\left(\dfrac{E_F - \Delta E}{kT}\right)}{F_{\frac{1}{2}}\left(\dfrac{E_F}{kT}\right)} \tag{2.8}$$

here μ_{Hall} and n_{Hall} are the Hall measurement values for mobility and concentration respectively, F is the shape-factor for the L-band and is 0.85, N_C's are the densities of states in the respective bands, $F_{\frac{1}{2}}(x)$ is Fermi-Dirac integral and is approximated as an analytic function of Fermi level energy E_F in reference [70]. Eq. (2.8) is calculated by iterating [76]:

$$E_F = kT\left(\ln\frac{n}{N_C} + \frac{n}{\sqrt{8}N_C}\right) \tag{2.9}$$

for various values of n till the ratio ${n_L}/{n_\Gamma}$ converges. This value is shown in Table 2.1, column 3. Then equations (2.6) to (2.7) are used to calculate the actual values of donor densities and carrier mobilities for the GaSb-on-GaAs samples which are shown in Table 2.1. Variation of the electron densities in the L- and Γ-band and the total density $n_T = n_L + n_\Gamma$ is plotted in Figure 2.13. This shows that with an increase in the total carrier concentration, most of the electrons populate the L-band rather than the Γ-band. However, eq.(2.8) can be approximated as:

$$\frac{n_L}{n_\Gamma} = \frac{N_C(L)}{N_C(\Gamma)}\exp\left(\frac{\Delta E}{kT}\right) \tag{2.10}$$

and using the ratio of density-of-states in L- and Γ-band as ~60 (according to parameters in Appendix 1), the total density n_T can be calculated. The difference between the exact and the approximate methods is only ~7% and does not affect the diode current density calculation in Section 5.5.

Note that the ratio of n_L/n_Γ increases rapidly as E_F is increased. This means at room temperature, most of the electrons reside in the L-band and the Hall concentration is actually an underestimate of the actual electron concentration. However, for the purpose of this thesis and the growth of diode samples in Section 5.2, growth conditions of sample #170 are followed to achieve a nominal electron density of 1.5×10^{18} cm^{-3}.

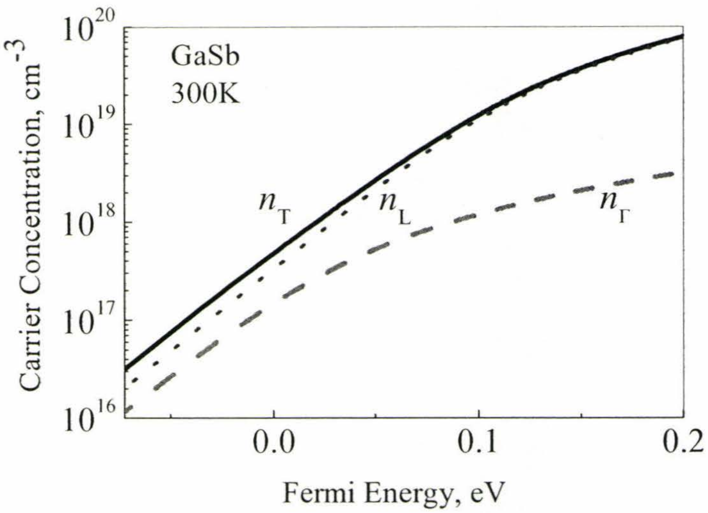

Figure 2.13: Total electron density and the densities in L- and Γ-band at room temperature.

Table 2.1: Dopant density and mobility calculation from Hall sample measurements.

	Dopant density, cm^{-3}					**Mobility, cm^2/V.s**		
Samples (T_G)	Measured	n_L/n_Γ	n_Γ	n_L	*total* n_T	Measured	μ_Γ	μ_L
#167 (500C)	2.81E+17	2.27	1.55E+17	3.53E+17	5.08E+17	2770	3739	748
#141 (500C)	4.49E+17	2.55	2.25E+17	5.75E+17	8.00E+17	2810	3905	781
#168 (500C)	8.43E+17	3.15	3.61E+17	1.14E+18	1.50E+18	2164	3186	637
#170 (500C)	8.57E+17	3.18	3.65E+17	1.16E+18	1.52E+18	1059	1563	313
#196 (475C)	1.33E+18	3.84	4.90E+17	1.88E+18	2.37E+18	2001	3129	626

Beryllium Cell

Compared to the GaTe cell, the acceptor dopant beryllium cell is well-behaved. Figure 2.14 shows the variation of acceptor concentration and mobility with the cell temperature.

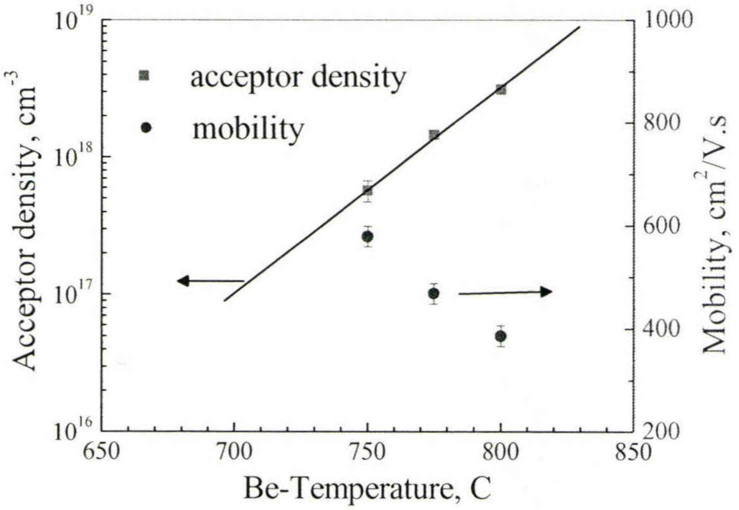

Figure 2.14: Acceptor concentration and mobility vs beryllium cell temperature.

Thick layers of unintentionally doped GaAs and GaSb were grown to determine the background doping densities in these two binary compounds. It was found that GaAs was n-type and GaSb was p-type and had carrier concentrations (mobilities) of $1.2(\pm0.2)\times10^{16}$ cm^{-3} (7517±40 cm^2/V.s) and $2.4(\pm0.2)\times10^{16}$ cm^{-3} (740±40 cm^2/V.s), respectively.

A simple expression can be used to model the measured mobility values:

$$\mu = \frac{\mu_r}{1 + \frac{n}{N_{\text{ref}}}} \tag{2.11}$$

where μ is the measured mobility at carrier concentration of n. The values of μ_r and N_{ref} are extracted from the plots of μ^{-1}-vs-n as shown in Figure 2.15. The measured values of electron and holes mobilities (from Figure 2.10 and Figure 2.14, respectively) are used in Figure 2.15 to extract the reference parameters which are also listed in the same figure. Electron mobilities measured from samples grown at the same temperature were only used.

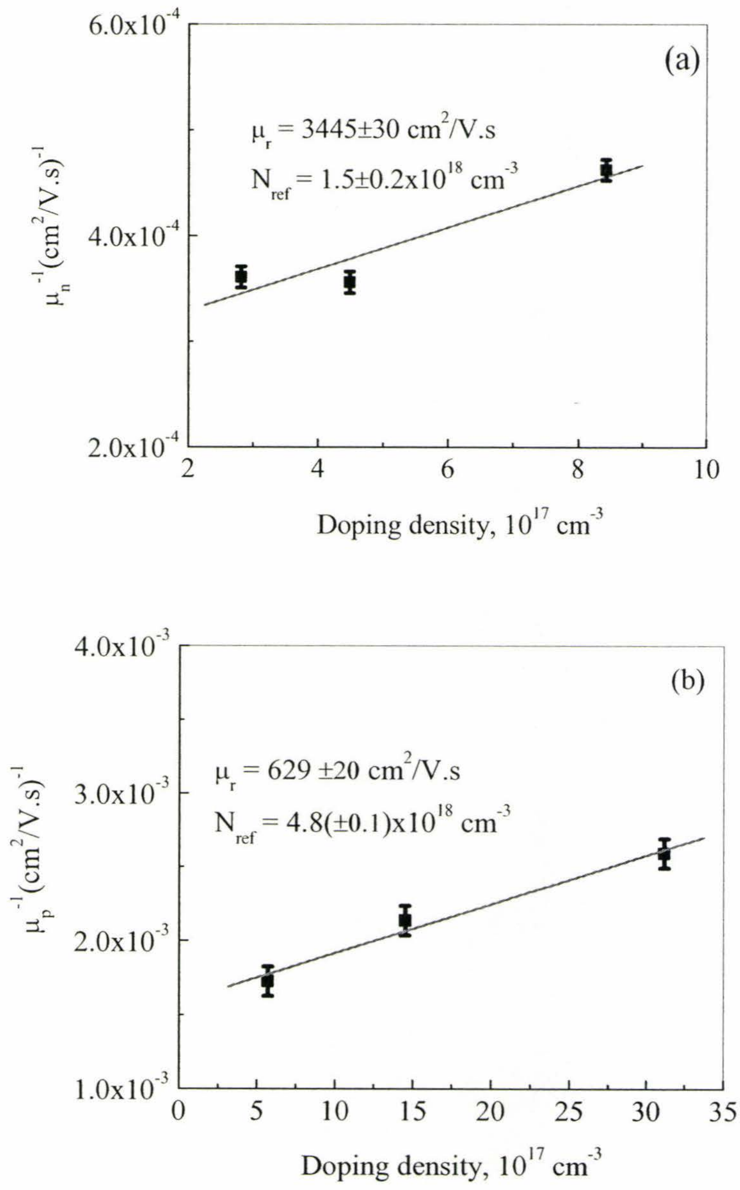

Figure 2.15: (a) Electron and (b) hole mobility fitting.

However, eq.(2.11) can be used to calculate electron and hole mobilities for an arbitrary carrier concentration over the ranges shown in Figure 2.15. At high carrier concentrations ($>10^{18}$ cm^{-3}), electron mobility behaves anomalously (see Figure 2.11(a)), and hence eq.(2.11) cannot be used in that range. Thus, eq.(2.11) can be useful to estimate mobility values for calculating device properties without requiring further measurements.

A note on the accuracies of the measured dopant densities: the electron and hole concentrations measured in this section are subject to measurement errors. The error bars provided on the respective figures provide an estimate for the observed variation from sample to sample. For the dopant concentrations and mobilities for GaSb, these variations are within $\pm 0.2\times 10^{17}$ cm^{-3} and ± 25 cm^2/V.s, respectively. The measured densities were also corrected for additional errors, such as: growth rate error (3% around 1.0 μm/hr nominal growth rate), geometric factor (within 5% of being square) and depletion thickness correction (10% of the total thickness).

2.5 Summary

This chapter discussed the calibration issues of the MBE machine used in the present research. Calibration of the indium, gallium, antimony, beryllium and gallium telluride solid-source cells and arsenic gas source were discussed. The antimony cell calibration was performed for the first time in this machine without any prior experience with antimony. Hence, quite a few challenging problems had to be solved before growth of epilayers could be initiated. The donor doping of GaSb was complicated by the presence of adjacent bands in the conduction band of GaSb and results in an underestimate of the actual donor concentration. The two-band model was used to calculate the total electron concentration. The accuracies of the measured electron and hole concentrations were within 10% of their respective values. The findings of this chapter are applied to the growths of metamorphic and device layers in Chapter 4 and Chapter 5, respectively.

Chapter 3 Etching Issues in GaSb

This chapter deals with the etching properties of the GaSb-based materials used in this research. First, a general discussion is provided on the etching issues and challenges involved in the wet chemical etching and the dry etching techniques and their recipes for GaSb. This is followed by a discussion of the details of wet chemical etching and the experimental results. We will discuss in more detail about one of the many dry etching techniques, namely reactive ion etching (RIE) techniques in a plasma environment, the plasma source being an electron cyclotron resonance (ECR) source. The sample patterns that were used for the etching studies are fabricated using standard lithographic processes (steps 1 to 12) discussed in Appendix 2 with appropriate flowchart.

3.1 Etching issues of GaSb

Fabrication processes relating to GaSb and related materials are getting increasing importance. There exists a comprehensive review [79] on possible etchants for III-V compounds. While some literature exists on issues involving wet chemical etching of GaSb [80],[81], problems are observed such as non-uniform etch rates, anisotropic etching and the poor quality of mesa sidewalls. These problems are also observed from the surface morphology obtained from wet etching in this work summarized in next section. To alleviate these problems, dry etching techniques were explored as an alternative etching technology. Reactive Ion Etching (RIE) is attractive because it produces low levels of surface damage and high-quality processing capabilities. RIE of GaSb-based materials is reported with different combinations of chlorine-based gas mixtures [82]-[84]. Although chlorine-based chemistries are being widely used, they face some problems with In-containing alloys. Also, this gas mixture corrodes the aluminum-pipes that make up the gas-exhaust system in the clean room. By comparison, methane-hydrogen (CH_4/H_2) combinations are known as 'universal etchants' for III-V semiconductors and have an inert gas (Ar or N_2) added to sustain the plasma and induce some physical sputtering. They are extensively used for InP and related compounds [87]-[89],[95],[98] attractive for their low damage to the sputtered surface. Both Electron Cyclotron Resonance (ECR) and Inductively Coupled Plasma (ICP) sources are used in RIE. A radio-frequency (rf) source, connected to the sample providing rf bias, helps to accelerate the ionic species toward the sample surface where etching takes place through ion bombardment which induces sputtering and enhances the chemical reaction. Some literature is available on ECR or ICP RIE applied to GaSb and its related materials using gas mixtures of $CH_4/H_2/Ar$ [86]-[89]. The reported etch properties, etch rate and surface morphology, differ due to the different chamber geometries and gas mixtures used. Hence, more studies are necessary to establish the systematic variations in etching results as a function of plasma and rf power, gas mixture and chamber pressure.

3.2 Wet Chemical Etching

A survey of wet chemical etching for GaSb-based materials can be found in [2],[80]. However, there are many other references that suggest one of many variants of existing recipes or sometimes a completely new recipe. In this work we have experimented with three different chemical solutions — citric acid solution, ammonium hydroxide solution and sulfuric acid solution.

Citric Acid Solution

Citric acid is a popular etchant for GaSb-based materials [80],[81], where hydrogen peroxide acts as an oxidizer with other solvents. We employed two different strengths of citric acid solution —

a. 2 Citric acid . H_2O : 1 H_2O_2

b. 1 Citric acid . H_2O : 2 H_2O_2

Preparation for solution [a] involves mixing 20 gm of anhydrous citric acid powder with 20 mL of de-ionized water. The solution was left for a day before being used. Then add one part of hydrogen peroxide (H_2O_2) to two parts of this hydrous citric acid by volume. Solution [b] was prepared in a similar way. Average etch rates measured for the above two solutions were — 9.6 Å/min (averaged over an etching time of 24 hours) and 14.5 Å/min (averaged over an etching time of 48 hours), respectively. Figure 3.1 (a) shows the etch depth with etch time using solution [a]. Etch rates obtained from Figure 3.1 are quite low. The etch morphology resulting from the same solution is shown in Figure 3.2 (a and b) seen through a high-resolution Scanning Electron Microscope (SEM). The side-walls are not sufficiently vertical for device fabrication and the etched surface is quite rough.

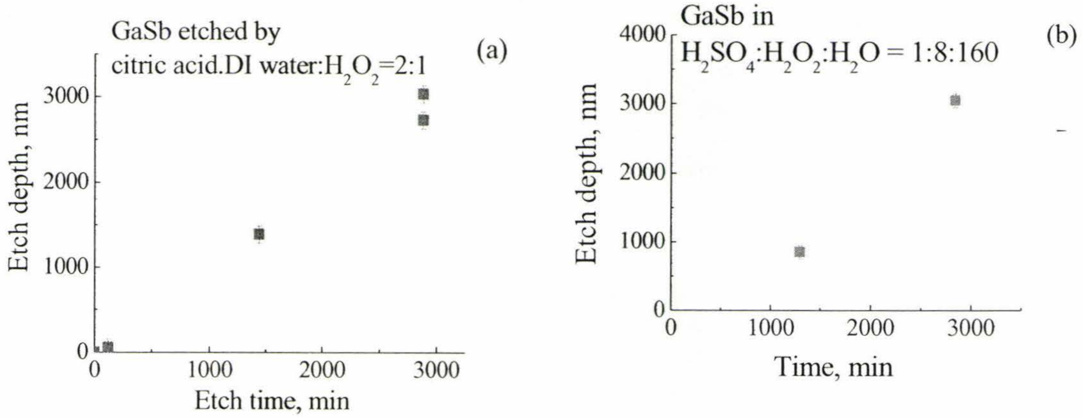

Figure 3.1: (a) Etch depth as a function of time for citric acid solution [a]. A linear fit suggests an etch rate of ~9.6 Å/min. (b) Etch depth versus time for the sulfuric acid solution.

Ammonium Hydroxide Solution

A dilute ammonium hydroxide solution [79] was also tried. The solution consisted of 10 mL of ammonium hydroxide (NH_4OH) mixed with 50 mL of de-ionized water to make a solution of NH_4OH : H_2O = 1:5. The average etch rate in this solution was determined to be ~5.5 Å/min. An SEM image of a mesa structure is shown in Figure 3.2

(c). Figure 3.2 (c) also shows the surface morphology for ammonium hydroxide solution and the features are poor.

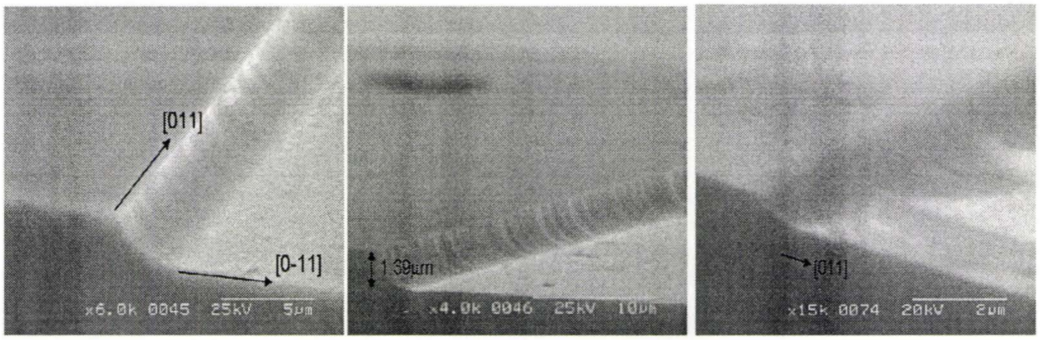

(a) (b) (c)

Figure 3.2: (a and b) SEM micrograph showing etch profiles of citric acid solution [a]. (c) SEM micrograph for ammonium hydroxide solution.

Sulfuric Acid Solution

Finally, a solution of sulfuric acid as suggested in [90] was attempted. The solution was prepared to get a relative strength of H_2SO_4:H_2O_2:H_2O = 1:8:160. The measured etch rate was very slow and it was ~14.2 Å/min. It had a long initial incubation time, where the solution had to etch through the top oxide layers before reaching the underlying GaSb. This is shown in Figure 3.1(b) as there is no etching for the initial ~670 minutes.

As a final comment, none of these wet chemical etching processes resulted in any detectable undercuts to GaSb mesas. However, the etch rates were slow, the mesa sidewalls were not vertical and the resulting etched surface was rough. Also, etch rates were found to be unaffected by the crystallographic orientations of $[011]$ and $[0\bar{1}1]$.

3.3 Reactive Ion Etching of GaSb*

A detailed study on dry etching can be found in [91], while a good review of plasma etching is found in [93]. In our studies, we used an ECR RIE process to investigate details of the etching characteristics of GaSb under various experimental conditions using mixtures of $CH_4/H_2/Ar$. Parameters, such as microwave power, rf bias, gas mixtures and chamber pressure, were systematically varied to observe how they affect the etch rates in GaSb. An atomic force microscope (AFM) and a scanning electron microscope (SEM) were employed to establish the surface morphology and etching quality in terms of roughness values and abruptness of the sidewalls, respectively.

One of the many techniques that can create high density plasma at low pressure is the ECR source first proposed by reference [93]. Our experimental setup closely follows that described by [93] and has been discussed in detail elsewhere [94],[95]. It is shown in Figure 3.3. Basically, this consists of a stainless-steel vacuum chamber, constantly pumped by a compound turbomolecular pump. The sample-stage supports the tantalum sample holder on which the samples are placed for etching purposes and the stage is water-cooled. The ECR source is a Wavemat MPDR 300B operating at a microwave frequency of 2.45 GHz. The required rf bias, inducing negative bias to the sample cathode, is provided by a 13.56 MHz source from Plasma Products Inc. (model RF5S) allowing the ions to bombard the sample with a controllable energy. Semiconductor grade process gases (CH_4, H_2, Ar, O_2 etc.) enter into the chamber through a mass flow controller. The chamber is systematically cleaned prior to every etch-run using an O_2-plasma to remove any residual polymer deposits, followed by Ar and H_2 plasma cleaning that removes left-over O_2 from the chamber. The microwave power provides the plasma, hence the ion density in the plasma is a function of microwave power, and the rf power to the sample chuck provides the bias that accelerates the ions incident on the sample surface, hence the ion current is a function of the rf power.

---

* Part of this section has been published in [99][99].

Experiment

Two-inch diameter p+-GaSb wafers were used throughout this experiment. These wafers were supplied by Wafer Technology, UK and were doped with zinc to the level of ~2x10^{18} cm^{-3}. Silicon dioxide was deposited on these wafers prior to pattern transfer. A simple mask with square and circular patterns was designed. Standard photolithography was used to transfer these patterns onto those wafers (see Appendix 2). The final pattern consisted of p+-GaSb wafer masked by simple SiO$_2$ squares and circles of varying sizes ranging from 5 μm to 400 μm in diameter. These wafers were then cleaved into smaller samples for etching experiments. The etching rate was determined by standard Alpha-step profilometer with an uncertainty of ~10 nm. Additional surface characterizations were done using an optical microscope, SEM and AFM.

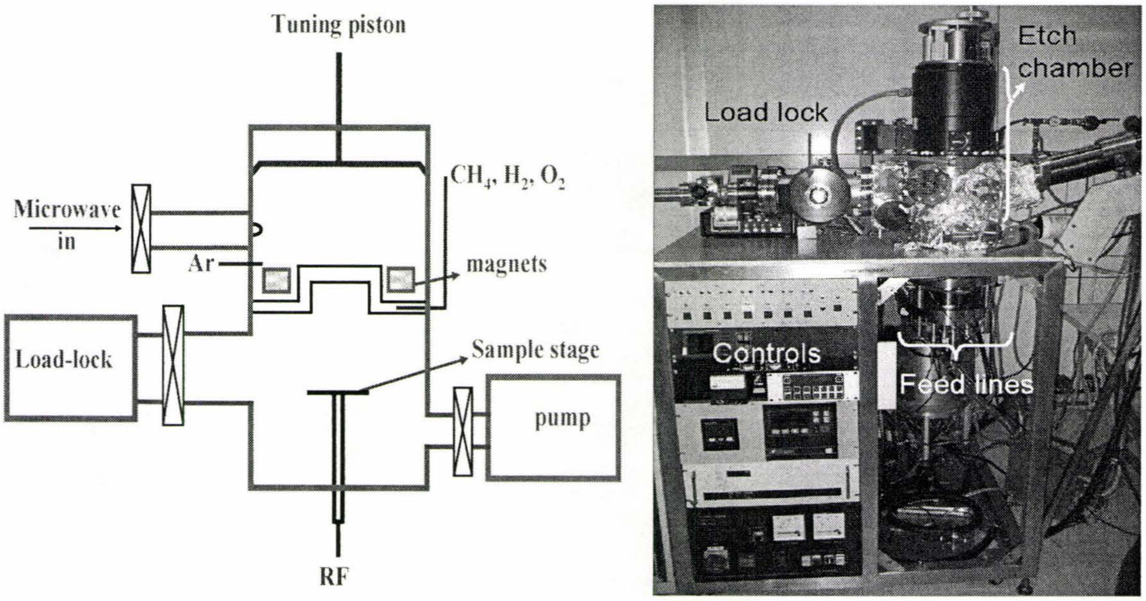

Figure 3.3: RIE chamber in CEDT, schematic (left) and real life (right).

Etching analysis

Using a fixed chamber pressure of 2.0 mTorr and gas ratios of CH_4:H_2:Ar = 4:16:7.6, measured in sccm by flowmeters, the etching characteristics were determined as a function of ECR microwave power (P_{plasma}) for two rf power levels (P_{rf} = 275 W and 100 W). This gas mixture was based on one used successfully for etching GaAs and InP and related compounds in our ECR system. The results for the etch rates for microwave powers of 50 – 300 W are shown in Figure 3.4 for both rf power levels. The etch rate is observed to increase with increasing microwave power for microwave powers up to ~200 W and increases with the rf power. Above 200 W microwave power and at the higher rf power (275 W), the etch rate continues to increase linearly up to 300 W, while with an rf power of 100 W, the etch rate appears to saturate at ~ 40 to 45 nm/min. Observance of saturation in etch rates is explained below in connection with Figure 3.5.

It was noted after etching that the SiO_2 mask is thinned by sputtering during the etching process. In order to measure this loss rate, Si-wafers were mounted with identical SiO_2 patterns along with the GaSb samples in the etching chamber. Figure 3.4 (open symbols) shows this rate of loss of the mask material with changing microwave and rf power levels. The etch rates in GaSb (filled symbols) have been adjusted for this loss. This rate of SiO_2 loss is a stronger function of rf power level than microwave power. At rf power of 100 W, the mask etch rate is ~5 nm/min, independent of the microwave power, while at 275 W, the mask etch rate increases with the microwave power, reaching ~20 nm/min at 300 W (microwave power). The predominant chemical reaction that takes place on the surface of the GaSb samples is the following [97]:

$$\mathrm{GaSb} + 3\mathrm{CH}_4 \xrightarrow{H_2} \mathrm{Ga}\left(\mathrm{CH}_3\right)_3 + \mathrm{SbH}_3$$

Methane, in the presence of excess hydrogen gas, reacts with GaSb to produce tri-methyl-gallium and stibine gaseous products, both of which are volatile. This chemical reaction takes place in addition to the physical sputtering caused by Ar-ions in the RIE chamber. Similar volatile compounds and other possible group-V organometallic compounds are reported in [94] for GaAs and InP etching in the same RIE chamber as used in this research.

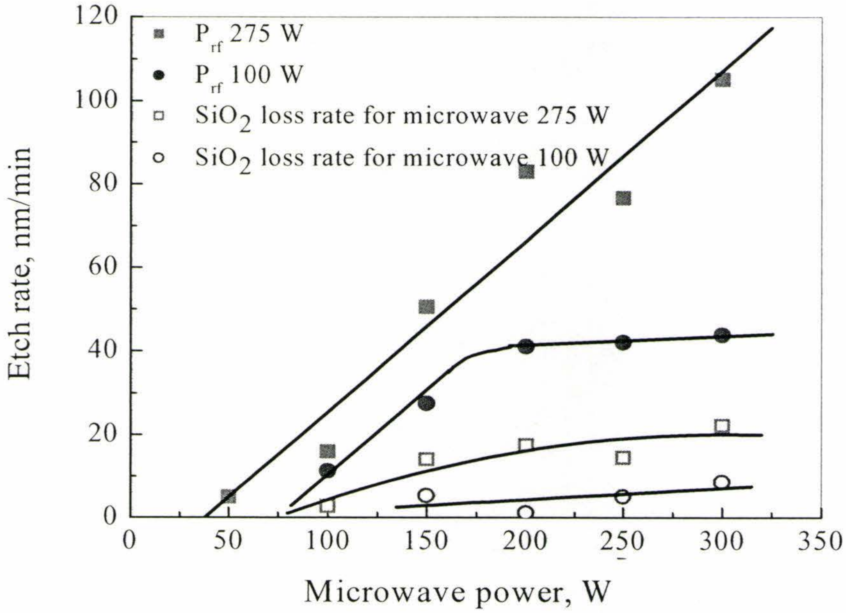

Figure 3.4: Etch rate variation with microwave power for two levels of rf power. Mask etch rate is also shown for two rf levels and is represented by unfilled symbols. Chamber pressure is 2.0 mTorr.

In Figure 3.5 a log–log plot of the absolute value of the bias voltage (V_{DC}) against microwave power is shown. The lines correspond to the relationship:

$$V_{DC} \propto \frac{1}{\sqrt{P_{Plasma}}} \tag{3.1}$$

This behavior is explained using the relationship between the ion flux (I_{ion}) and dc self bias given in [89]:

$$P_{rf} = V_{DC} I_{ion} \tag{3.2}$$

where the ion flux increases with the ECR plasma power as $\sqrt{P_{\text{Plasma}}}$ [93]. Hence, at constant P_{rf}, the self-bias voltage decreases with increasing ECR plasma power and increases with increasing rf power. The saturation behavior of the etch rate for the lower rf power (100 W) at high ECR source power (>200 W) occurs because the decreasing V_{DC} produces less kinetic energy for the bombarding ions (~150 eV), thus reducing or eliminating the physical sputtering contribution to the etch rate. For the high rf power (275 W), the ions have higher energy (~290 – 310 eV) over all ECR power levels ensuring enough physical sputtering over the chemical etching component. As a result, etch rates continue increasing along with the microwave power in the later case. It appears from our experiment, that changing microwave levels is preferable in order to achieve controllable etch rates, since changing rf bias, particularly beyond 150 W, results in less stable bias conditions.

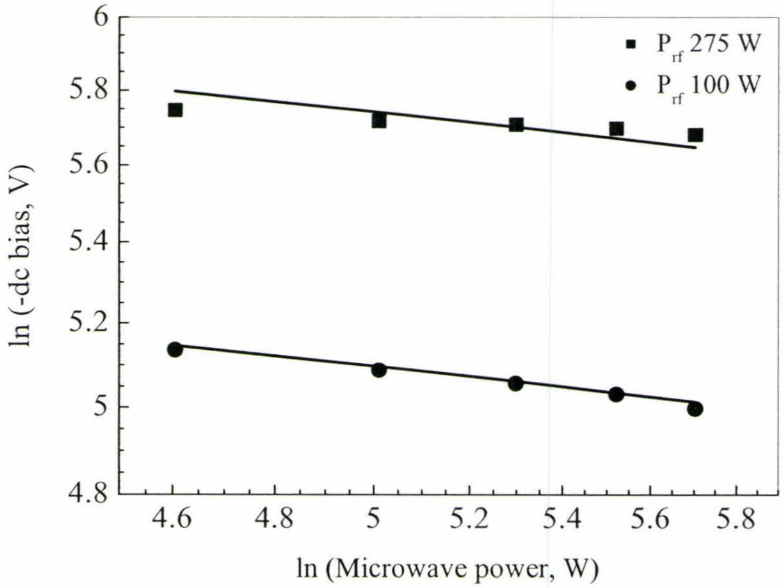

Figure 3.5: Bias voltage variation with microwave power for the same rf power levels, gas ratio and chamber pressure as in Figure 3.4.

Figure 3.6 shows the results for etch depth as a function of etch time using two rf power levels (100 W and 200 W) with the same gas ratio as used above, while all other parameters (chamber pressure and microwave power) are kept fixed. The etch depth is observed to increase linearly with time, but there exists a non-zero intersection of the linear fit to the actual experimental points with the time axis. This indicates that an "incubation time" is required by the plasma to initiate the reactive etching process. This is presumably the plasma exposure time required to sputter remove any surface oxides and other possible surface contaminants in order to produce a clean GaSb surface and allow the onset of the chemical component of the reactive ion etch process of the semiconductor. For the particular case of the lower rf level of 100 W, and for the specific parameters used, this time is about 3 minutes. With higher rf power level (e.g. 200 W in Figure 3.6), this 'incubation time' reduces to almost zero because of the increased sputtering rate associated with the increase in rf power levels removing surface contaminants more quickly. Hence, this "incubation time" loses any practical significance for higher values of power levels, but needs to be compensated for when etching shallow features at low rf and microwave power levels.

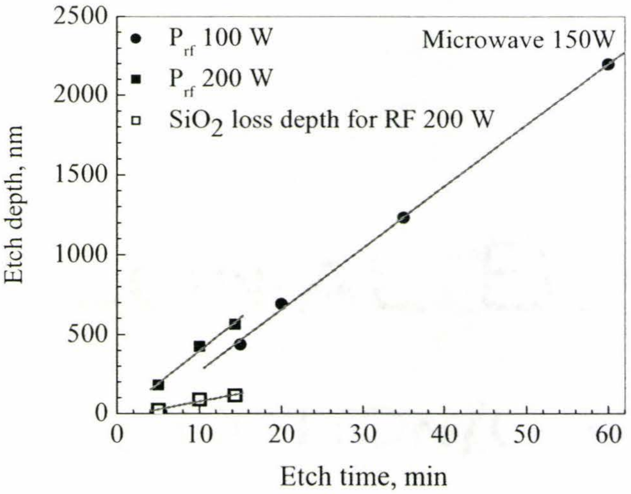

Figure 3.6: Etching depth measured with time for the same gas ratios as above. Etch depth in mask is shown for the rf power of 200 W.

Using the same gas ratios and chamber pressure, the variations of etch rate are given, after adjusting for the SiO_2 mask loss (filled symbols), as a function of rf power at the fixed microwave power levels of 200 W and 150 W are shown in Figure 3.7. The etch rates for the SiO_2 mask are also shown (unfilled symbols). The GaSb etch rate increases linearly with rf power at each fixed microwave power. Also, the etch rate is higher at the higher microwave power, as is the slope of the etch rate versus rf power. This is consistent with increased plasma density at the higher microwave power and a higher P_{rf} ensuring a higher energy of the bombarding ions which increases the sputtering component proportional to the ion energy as well as the reactive etching component. For our RIE system, the use of higher rf power (>200 W) resulted in heating of the sample stage and more residual polymer on the chamber surface requiring a longer O_2 plasma clean between sample etches.

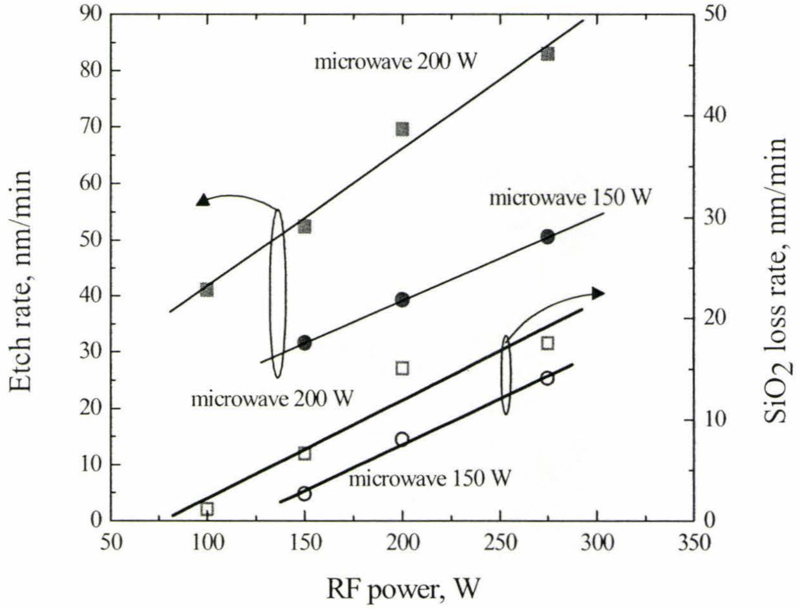

Figure 3.7: Variation of etch rate with rf power in GaSb (filled symbols) and in SiO_2 mask (unfilled symbols) for microwave powers of 150 W and 200 W.

The effect of the chamber pressure on the etch rate is given in Figure 3.8. The etch rate was observed to approach zero at the highest chamber pressure. It was suggested by others [86],[96] that the etch rate decreases with increasing pressure because there are more non-ionized particles at fixed microwave and rf power levels. As a result, the ions experience enhanced recombination with the non-ionized species, thereby resulting in a reduced rate of bombardment [92]. An alternative explanation has also been suggested [96] where increased polymer deposition occurs at higher chamber pressure. Our experience also confirms thicker polymer deposition for higher chamber pressures which required longer O_2-plasma run for its removal. However, from our work it is not possible to select between the processes and it is possible that both play a role.

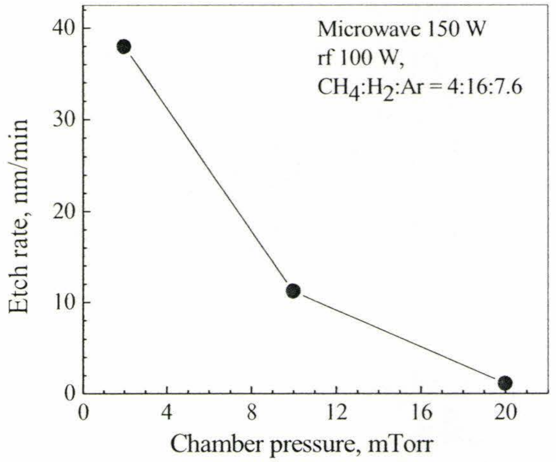

Figure 3.8: Etch rate variation with chamber pressure.

The effect of changing the ratio of the gas mixtures was also investigated. The methane-hydrogen ratio was changed from 4:16 to 8:12 keeping the total flow fixed at 20 sccm. An increased argon flow of 25 sccm was used similar to that in [86]. Figure 3.9 compares the effect of this changed gas ratio to the etching rates given previously in Figure 3.4. The rf power level was kept constant at 100 W and microwave power level was varied from 100 W to 250 W. It can be seen that the higher Ar flow produces a somewhat higher etch rate by ~7 nm/min at low microwave powers and no indication of saturation, unlike that seen at microwave powers above 200 W with the lower Ar ratio. This increase in etch rates can be explained from the fact that higher Ar-flow contributes to a higher sputtering yield compared to that of the low Ar-ratio. However, this increase in etch rate is accompanied by an increased sample temperature and higher residual polymer deposition, thus requiring longer polymer removal cycles involving oxygen-plasma.

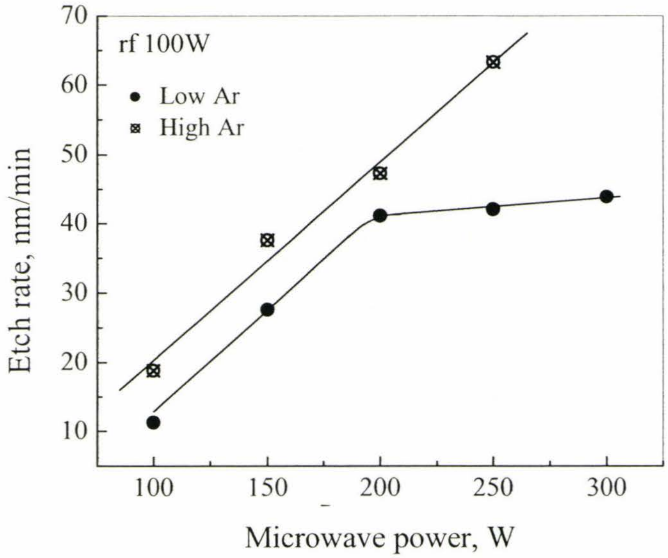

Figure 3.9: Dependence of etch rate on gas ratios. The filled circles represent gas ratios of CH_4:H_2:Ar = 4:16:7.6 (repeated from Figure 3.4), the crossed circles represent CH_4:H_2:Ar = 8:12:25. Chamber pressure is 2.0 mTorr in both cases.

Figure 3.10 shows SEM images taken for the etched mesas. The plasma etching resulted in very smooth surfaces and the side walls are abrupt and vertical at the lowest microwave power, but become less abrupt as the microwave power is increased. A weak 'trenching' effect is observed which is caused mainly by ions reflected off the side-walls [92]. Also observed are side-wall striations which are similar to those seen in Figure 3.2 (a and b) for mesas etched in a wet solution (citric acid.deionized water:hydrogen peroxide = 2:1). This suggests that these side-wall striations are most likely caused by the roughness of the chromium mask, similar to the observations in [97] and [118]. Increasing microwave and/or rf power results in some roughening of the surface (Figure 3.10(b), (c) compared to Figure 3.10(a)).

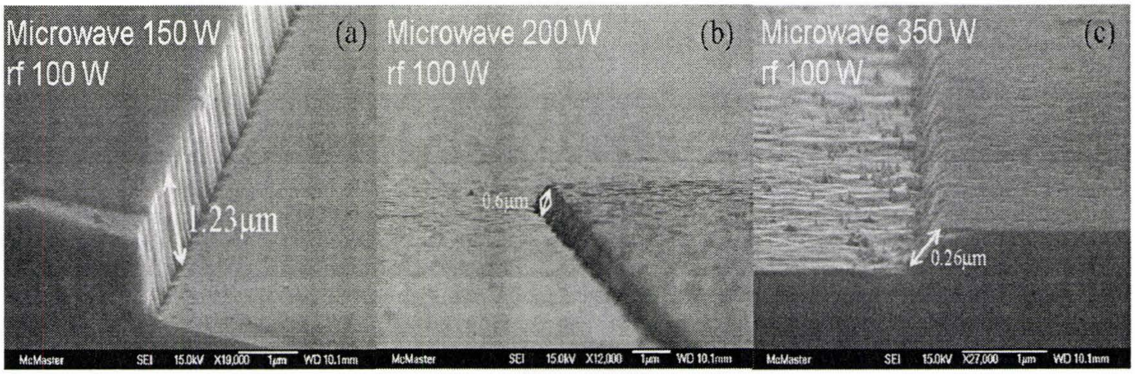

Figure 3.10: Scanning Electron Microscopic images of etched mesa structures. In all cases the rf power was 100 W. The microwave power was varied: (a) 150 W, (b) 200 W, and (c) 350 W.

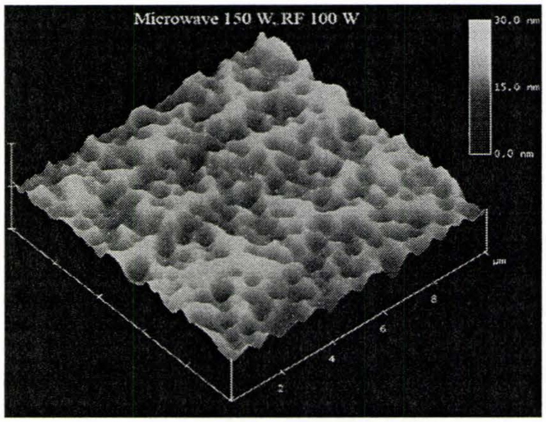

Figure 3.11: Atomic Force Microscopic image of a typical sample. Chamber pressure 2.0 mTorr and CH_4:H_2:Ar = 4:16:7.6.

Table 3.1: RMS roughness values (in nm) for different microwave and rf power levels. Corresponding etch depths (±10 nm) are shown in bracket.

	Microwave power		
RF power	*150 W*	*200 W*	*350 W*
100 W	0.9±0.2 (2200 nm)	_	3.6±0.2 (262 nm)
275 W	2.05±0.2 (430 nm)	4.1±0.2 (408 nm)	_

Table 3.2: RMS roughness values (in nm) for different chamber pressure and Ar-ratio (microwave 150 W and rf power 100 W). Corresponding etch depths (±10 nm) are shown in bracket.

Argon	Chamber pressure (mTorr)	
Ratio (sccm)	2	10
Low (7.6)	0.94±0.2 (1230 nm)	0.95±0.2 (225 nm)
High (25)	0.75±0.2 (1503 nm)	_

Table 3.1 presents the rms roughness values for the surfaces etched by different microwave and rf power levels. Table 3.2 presents the roughness data for different levels of chamber pressure and argon ratio for fixed microwave and rf power levels. The general trend shows that with higher rf power and/or higher microwave power, the surface tends to become more rough. The overall surface roughness is excellent with the given ranges of parameters that were used in this study. When compared to the SEM micrographs in reference [86], Figure 3.10 shows excellent surface quality. AFM results show a better surface morphology compared to that of InP after ECR [98]. Figure 3.11 depicts a typical AFM scan for one of the samples. Images in Figure 3.10 and Figure 3.11and data in Table 3.1 are taken from samples etched with identical parameters, such as chamber pressure (2 mTorr) and gas ratios (CH_4:H_2:Ar = 4:16:7.6).

A final note on the accuracy of measurements in this chapter: A variation of ±10 nm is observed in the measurements of the etch depths and is due to the error originating from the Alpha-step profilometer and from variations within a sample. This error, however, produces a maximum variation of ±2 nm/min on the smallest etch rates reported. For higher values of etch depths and rates, this error causes an insignificant variation of the data points.

3.4 Summary

Both wet and dry etching of GaSb-based materials has been studied in this chapter. Three different etchant solutions were experimented with. However, the resulting etch rates were slow and the resulting mesa sidewalls were not abrupt. Since metamorphic layers contain a large threading dislocation density, wet etching may result in preferential etch in certain directions. This could ultimately be detrimental to the final device characteristics. Hence, reactive ion etching of GaSb samples was investigated using $CH_4/H_2/Ar$ gas mixtures. Different etching parameters (e.g. microwave and radio-frequency (rf) power levels, gas ratios, chamber pressure etc.) were systematically varied to observe their effects on the etch characteristics. Excellent feature geometries were observed with vertical sidewalls and a smooth surface morphology. The maximum variation on the etch rates are estimated to be less than ±2 nm/min which is due to variation in the etch depths measured.

Chapter 4 Growth and Characterization of Metamorphic Buffers

We shall discuss the growth and characterization of metamorphic buffer layers in this chapter. The calibration results for the MBE, discussed in Chapter 2 are applied to the various growths. Once the metamorphic substrates (M-substrate) are grown in the MBE, a set of characterization techniques are applied to determine the in-plane lattice constant and the amount of relaxation of the terminal layer. This is of utmost importance, because typically the M-substrate is not fully relaxed, hence subsequent layer growths need to be lattice matched to the terminal layer. High resolution x-ray diffraction analysis (HRXRD) was used to determine the in-plane lattice constant of this terminal layer using a BEDE D1 high-resolution diffractometer. Cross-sectional transmission electron microscopy (XTEM), plan-view transmission electron microscopy (PVTEM) and atomic force microscopy (AFM) are used to further characterize these metamorphic layers. Cross-sectional TEM samples were prepared using conventional thinning processes including mechanical polishing and Ar-ion milling and the samples examined in a Philips CM12 TEM operating at 120 keV.

Initially, it was planned to grow a metamorphic substrate of GaSb on InP using $GaAs_xSb_{1-x}$ step graded from $x = 0.51$ to 0. The results of this work will be described in Section 4.3 and yielded useful data on the growth of metamorphic substrates. It was later decided to grow the InGaSb device structures on GaSb substrates to ease the growth requirements. However, this GaSb substrate can also be grown metamorphically as an M-substrate on InP.

4.1 Determination of Lattice Constants by X-Ray Diffraction

X-ray diffraction (XRD) analysis is a standard tool to characterize epilayers grown in MBE and is very important for characterizing the metamorphic layers. A general introduction to XRD techniques can be found in [78]. Useful reviews of this technique applied to semiconductor structures can be found in [101]-[103]. The perpendicular lattice constant of the epilayer ($a_\perp$), is calculated from the angular difference between the substrate peak and that of the metamorphic layer peak in an omega-2theta (Ω-2θ) scan around (004)-plane of reflection. The following definition has been used for $a_\perp$ [104]-[107]:

$$a_\perp = \frac{l \cdot \lambda}{2\sin\theta\ \cos\phi} \tag{4.1}$$

where h, k, l are the Miller indices of the plane of reflection [hkl], ϕ is the angle between the diffraction plane and the [001] surface plane, and λ is the wavelength of the x-rays (1.5406 Å). θ equals the Bragg angle of the substrate (θ_B) plus the incremental angle ($\partial\theta$) obtained from the peak separation of the epilayers from that of the substrate: $\theta = \theta_B + \partial\theta$.

A typical example of an Ω-2θ scan is shown in Figure 4.1 and the incremental angle $\partial\theta$ is indicated. Usually, for a layer where the composition is not precisely known and which may not be fully relaxed, the in-plane lattice constant ($a_\parallel$) of the layer is determined from the angular difference between the substrate peak and that of the metamorphic layer peak in an asymmetrical XRD scan, typically around (224)-plane reflection. However, asymmetric scans are difficult to perform due to the requirements for fulfilling the glancing incidence and glancing exit angle conditions. Also, it is hard to distinguish the metamorphic peak in such asymmetric scans and requires long x-ray scan times in conjunction with reciprocal space mapping [103],[111],[112].

An alternate way to calculate in-plane lattice constant from that of the perpendicular one is through Poisson's ratio [108],[109] using:

$$\frac{a_{\perp} - a(x)}{a_{\parallel} - a(x)} = -2\frac{C_{12}(x)}{C_{11}(x)} \tag{4.2}$$

where the value of $a(x)$ is the fully-relaxed lattice constant of the material of concern. Stiffness coefficients $C_{12}(x)$ and $C_{11}(x)$ are tabulated for binary compounds or can be obtained for ternaries or quaternaries by linearly interpolating between the constituent binaries. The correct value of the terminal composition (x) of the M-substrate needs to be known, otherwise eq.(4.2) will give incorrect results. The relaxation mechanism is complicated and dislocations may form to distort the tetragonal structure which may ultimately result in an incorrect terminal composition compared to what was expected. One way to circumvent this dilemma is to grow a single cap layer of a binary compound on top of the terminal M-layer, sufficiently thin that it remains fully strained, and perform one (004) scan which will exhibit peaks from the initial substrate, the M-substrate and the cap layer. This technique was reported by Czaban et al.[105],[110] and is followed here by using a thin layer of GaSb grown on top of the metamorphic structures (particularly with those of InGaSb) and requires only a single (004) scan. This GaSb cap-layer is tensile strained with respect to the metamorphic layer, and for analytical purposes, it must be sufficiently thin so that it remains fully strained.

An XRD rocking curve is shown in Figure 4.1 for an epilayer of GaAsSb grown on GaSb. The satellite peak, corresponding to the epilayer, is on the right side of the substrate peak indicating that it is under tensile strain. If the satellite peak is on the left then the layer is under compressive strain. The percentage relaxation in the M-layers compared to that of the substrate is defined as [109]:

$$\%\text{Relaxation} = \frac{a_{\parallel} - a_{\text{substrate}}}{a_{\text{fully-relaxed}} - a_{\text{substrate}}} \tag{4.3}$$

where $a_{\|}$ and $a_{\text{fully-relaxed}}$ correspond to the measured value of the in-plane lattice constant and its natural lattice constant for its composition.

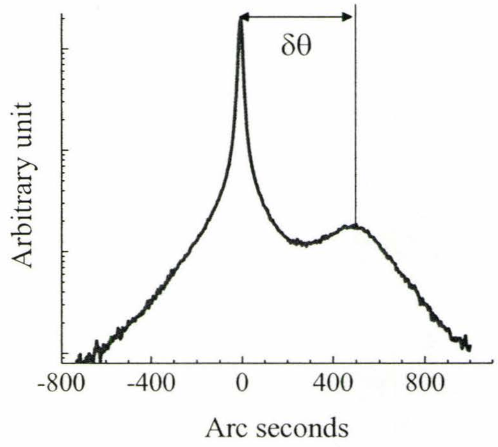

Figure 4.1: Typical X-ray rocking curve. The peak corresponds to the GaSb substrate and the satellite peak corresponds to the epilayer GaAsSb. The angular displacement ($\partial\theta \sim 495''$) of the two peaks corresponds to 2.9% arsenic in the epilayer.

The accuracy of the values of the lattice constants, relaxation values and compositions thus calculated, depend on the accuracy of the peak separation measurement. An error of $\partial\theta = \pm 20$ arc-seconds in the measurement of the peak separation results in a 0.016% error in the calculated a's ($a_{\perp}$ and $a_{\|}$). This will cause ±3% by fraction change in relaxation values and ±1% by fraction change in the composition values. Hence, extra care was taken to measure the peak separation values. These accuracy levels apply to calculations listed in Table 4.2 and Table 4.3.

4.2 Incorporation Study of Arsenic and Antimony

Before proceeding with the growth of GaAsSb buffer layers, many epilayers with varying concentrations of arsenic or antimony were grown in the MBE in order to calibrate the growth rates, the group-III cell temperatures and the group-V fluxes.

Table 4.1: Flux ratio calculations.

Samples grown on InP

Sample	x (As)	Antimony flux		Arsine flow	As-flux		Flux ratio
		× 10^{-6}, torr	ML/s	sccm	torr	ML/s	Sb/As+Sb
	(±0.01)		(±0.02)			(±0.06)	(±0.01)
LM to InP	0.513	1.88	1.23	2.28	5.04	1.23	0.50
#21	0.51	1.88	1.23	2.25	4.98	1.21	0.50
#22	0.50	1.88	1.23	2.14	4.76	1.15	0.52
#23	0.47	1.88	1.23	1.93	4.36	1.04	0.54
#25	0.42	1.88	1.23	1.54	3.57	0.83	0.6
#26	0.37	1.88	1.23	1.3	3.07	0.7	0.64

Samples grown on GaSb

Sample	x (As)	Antimony flux		Arsine flow	As-flux		Flux ratio
		× 10^{-6}, torr	ML/s	sccm	torr	ML/s	Sb/As+Sb
	(±0.01)		(±0.02)			(±0.01)	(±0.005)
#28	0.03	1.88	1.33	0.10	0.36	0.06	0.96
#29	0.09	1.88	1.33	0.31	0.86	0.18	0.88
#36	0.16	1.88	1.33	0.42	1.11	0.24	0.85

In order to understand the incorporation of group-V atoms, thin epitaxial samples were grown both on InP and GaSb substrates with changing arsenic fluxes. Growth temperatures for all these samples, except two, were around 500° C, as measured by the optical pyrometer. Samples #29 and #36, with 91% and 84% Sb respectively, were grown at 520°C and 540°C, respectively. All these samples were then characterized by x-ray diffraction to determine the composition. The required flux calculations are shown in Table 4.1. An arsenic flow of ~2 (±0.1) sccm, corresponding to a flux of ~1.0(±0.06) ML/s, was calibrated for samples grown on GaAs at ~1.0 μm/hr growth rate. The beam pressure of Sb, measured using an ionization gauge flux monitor, was fixed at ~1.88×10^{-6}

Torr (see Section 2.3, page 30). This pressure corresponds to an antimony flux of ~1.2 ML/s on InP and ~1.3 ML/s on GaSb.

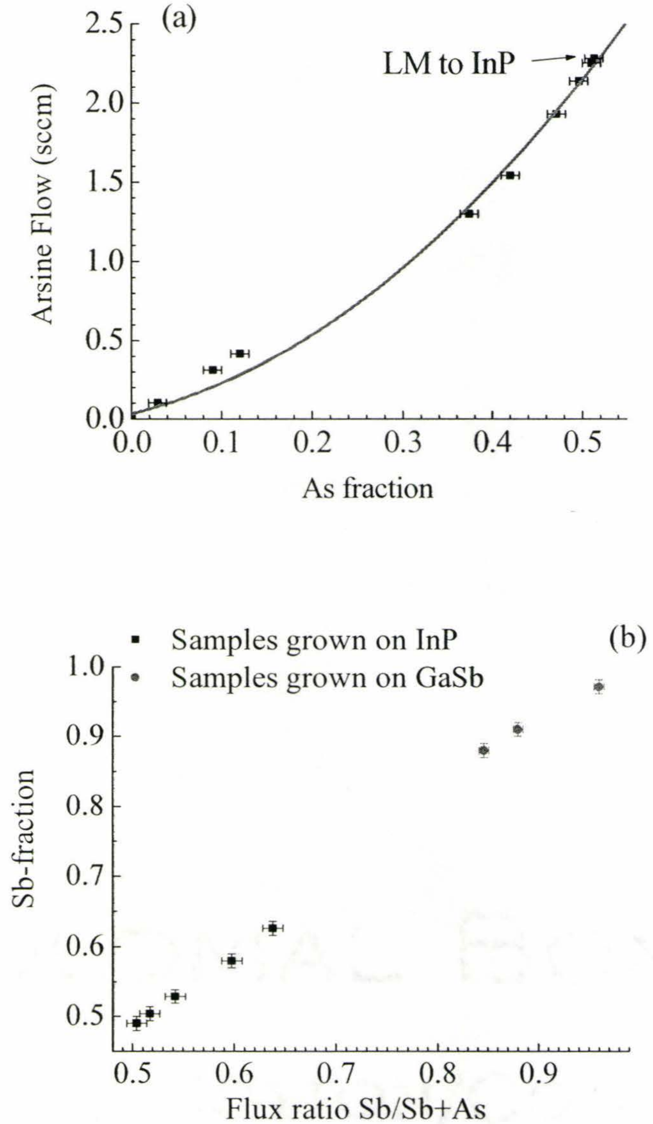

Figure 4.2: Incorporation study of group-V fluxes (Sb and As) for $GaAs_{1-x}Sb_x$ epitaxial layers.

This study, summarized in Figure 4.2, shows how the arsenic flow should be changed for growth of GaAsSb buffer layers (discussed in the next section) with diminishing As-fraction. Figure 4.2(b) suggests that arsenic and antimony are competing almost equally at these ranges of growth temperatures and flux ratios. Also, a higher growth temperature does not have any significant effect on the incorporation of As and Sb atoms on the GaSb-based epilayers. This incorporation data was then used for the growth of the GaAsSb metamorphic samples.

The accuracy of the data presented in this section depends on the error in the determination of epilayer compositions and the flow rates. An error of $\partial\theta = \pm 40$ arc-seconds will result in ±0.01 change in the arsenic fraction listed in Table 4.1, column2. Also the variation in arsenic flow of ~2 sccm is estimated to be ~ ±0.1 sccm due to approximations used in designing the orifice of the gas flow element. These data variations cause a variation in the flux ratios calculated in column 8, Table 4.1 and represented as error bars in Figure 4.2.

4.3 Growth and Characterization of GaAsSb Metamorphic Layers*

The epilayer structure for the GaAsSb metamorphic sample is shown schematically in Figure 4.3.

Growth

All the layers of the metamorphic samples were grown in the MBE machine discussed in Chapter 2. Gaseous AsH_3 was cracked at 950°C to provide As-dimer species. The beam pressure of Sb, measured by a flux monitor temporarily inserted in the position of the substrate holder, was fixed at $\sim 1.88 \times 10^{-6}$ Torr for the entire growth. This ensures an antimony overpressure of 1.23 ML/s on epilayers grown on InP substrates (see Section 2.3, page 30). The InP substrate, used for the growth of the metamorphic samples, was de-gassed at 250° C after loading in a preparation chamber and then the oxide was desorbed in the MBE growth chamber through exposure to a hydrogen plasma. The

---

* Part of this work was published in [115].

desorption temperature was 480° C with an overpressure of P_2 for 8 minutes. The substrate temperature was then ramped slowly up to the growth temperature to begin growth.

GaSb	100 nm	*Cap layer*
InAs	10 nm	*Quantum well*
GaSb	0.5 μm	*Metamorphic layer*
$GaAs_{1-x}Sb_x$, $x = 0.97$	83 nm	*Buffer layers*
16 layers of $GaAs_{1-x}Sb_x$, starting with $x = 0.52$ and in each layer As is reduced by 3%	Each layer 83nm	
$GaAs_{1-x}Sb_x$, $x = 0.49$ LM to InP	167 nm	
InP buffer	100 nm	
InP substrate		

Figure 4.3: Growth schematic for GaAsSb metamorphic layers.

Starting with an InP buffer on an InP substrate, the first layer of $GaAs_{1-x}Sb_x$ was grown with x = 0.49, which is lattice matched to InP. In the subsequent layers of $GaAs_{1-x}Sb_x$, the As-fraction has been reduced in steps of 0.03 to reach GaSb ($x = 1.0$) in the top layer. Figure 4.2(a) gives the calibration data for reducing the arsenic flow from the lattice-matching condition to InP (51%-As) to GaSb (0%-As).A total of 17 buffer layers, each 83 nm thick, were grown to reach the GaSb top layer. The total thickness of the buffer layers was 1.5 μm. A 0.5μm GaSb layer was then grown followed by an InAs quantum-well (QW) layer of 10 nm thickness which was capped by another 100 nm GaSb layer. The temperature for the entire growth process was maintained at ~490° C measured by the pyrometer. Our goal was to grow a type-II quantum-well to obtain some photoluminescence that could yield valuable information regarding the optical quality of the M-layer. In the present attempt, we used a source switching procedure in the growth that resulted in the formation of a GaAs-like interfacial layer on which the InAs layer was grown. Finally, it was capped by a 100 nm GaSb layer using source switching again that resulted in an InSb-like interfacial layer. The interface between InAs-QW and GaSb layer was highly defective, as clearly seen in XTEM images of Figure 4.6 and significant surface roughness was seen by AFM, hence no photoluminescence was observed.

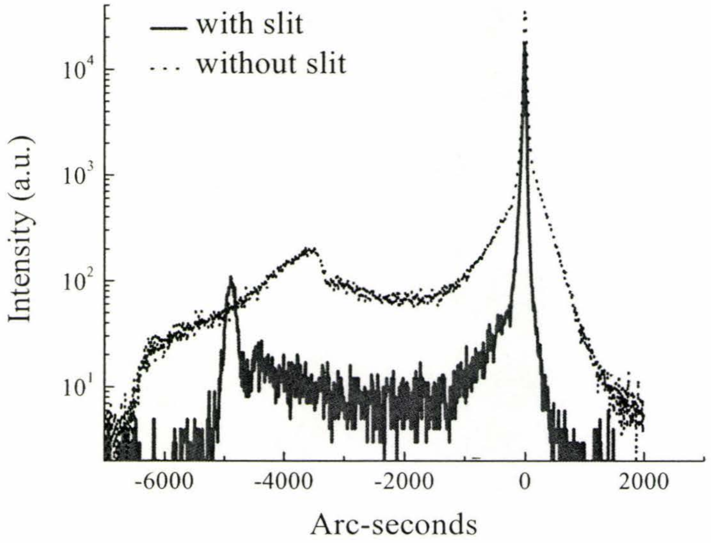

Figure 4.4: X-ray rocking curves (symmetric scan) for the as-grown sample in the [011]-direction, with and without slit.

Characterization

Post-growth Annealing – The sample with the metamorphic layer was cleaved into small pieces to perform 30 s rapid thermal anneals (RTA) on each piece at 500, 550 and 600° C. These samples were then characterized by HRXRD, XTEM and AFM.

HRXRD – We have used the standard symmetric scan around the (004)-plane to measure the lattice constant ($a_\perp$) perpendicular to the growth surface, in both the [011] and [0 $\bar{1}$ 1] directions. A narrow (0.5 mm) slit was positioned in front of the x-ray detector to define the peak due to the GaSb metamorphic layer more clearly, which would otherwise be greatly broadened due to the mosaicity [105] in the metamorphic buffer. Figure 4.4 shows how this arrangement improves the resolution and makes the GaSb peak clearly visible at ~4800 arc-s.

Table 4.2: Average values of $a_\perp$ and $a_\parallel$, obtained from x-ray analysis of the as-grown and annealed samples.

	Peak separation, $\partial\theta$ (arc-seconds)	$a_\perp$ (Å)	$a_\parallel$ (Å)
As-grown	-4921	6.107	6.083
500° C	-4823	6.102	6.088
550° C	-4866	6.104	6.086
600° C	-4865	6.104	6.086
Average		6.104	6.086

The in-plane lattice constant ($a_\parallel$) was determined from the measured values of $a_\perp$ and the use of Poisson's formula (see Section 4.1, eq.(4.2)). In this particular growth, since the terminal layer is a binary compound of GaSb, the stiffness coefficients are well known and there is no need to estimate the composition (x) in eq.(4.2). In Table 4.2, values of $\partial\theta$, $a_\perp$ and $a_\parallel$ are averaged over the [011] and [0$\bar{1}$1] directions. From Table 4.2, it is seen that the average value of $a_\parallel$ is within 0.2% of that of a relaxed GaSb layer (6.0954Å). Annealing has no effect on the value of $a_\parallel$.

XTEM – TEM micrographs from the overall grown areas (Figure 4.5) clearly show that dislocations are mostly confined into the GaAsSb buffer layers. The density of the dislocations threading through the GaSb metamorphic layer is small ($< 4\times10^7$ cm^{-2}) compared to those in the underlying buffer layers. The remaining dislocations in the metamorphic layer, seen in Figure 4.5 (a, b and c), are originated either from the underlying buffer layers or from the top rough interface. Post-growth annealing at 600° C reduces these dislocations in the metamorphic layer to less than 10^7 cm^{-2} (Figure 4.5(d)).

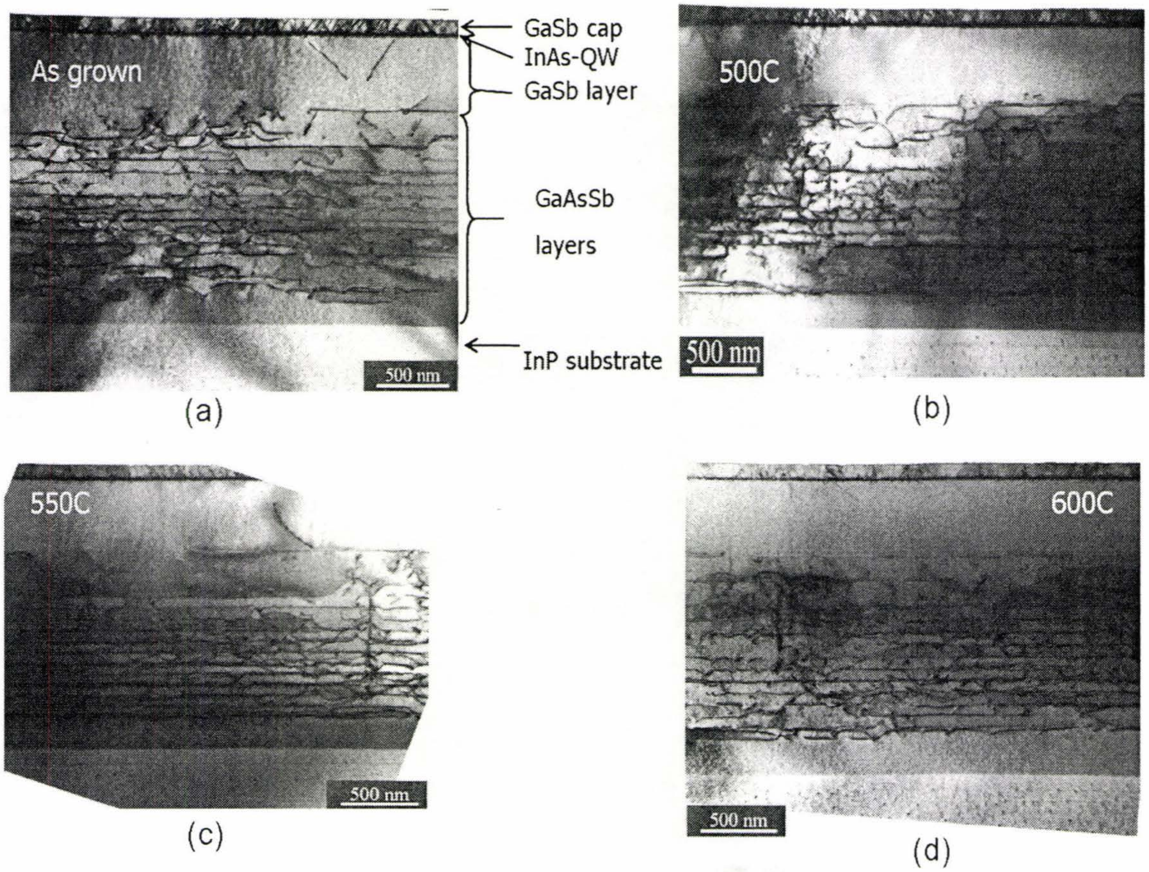

(a) (b)

(c) (d)

Figure 4.5: XTEM images of (a) as-grown and of samples post- annealed at (b) 500°C, (c) 550°C and (d) 600°C for 30s.

The roughness of the interface between the InAs-QW and metamorphically grown GaSb layers is due to non-optimum growth conditions of the InAs layer and an inadequate source switching procedure at the GaSb/InAs interface. On close observation through XTEM images of Figure 4.6, the InAs QW-layer appears to be the source of dislocations that propagate through the cap layer. Also, the roughness of this interface is the reason for the surface roughness seen in AFM. In Figure 4.6, the images show InAs-QW layer running across the figures as a dark thread. These images suggest that the interface is not improved by thermal annealing. Also, the interface roughness was seen in both cases of a sample grown directly on a GaSb substrate and on a metamorphic substrate. Irrespective of whether or not the QW-layer was grown on metamorphic layers, these QWs introduced dislocations propagating up and down. Certain growth conditions [3],[113]-[114], for example substrate temperature and growth pauses, have to be maintained to obtain a smooth interface between InAs and GaSb. This roughness and the fact that the interface is of 'broken-gap type,' were the main reasons for no convincing photoluminescence yield.

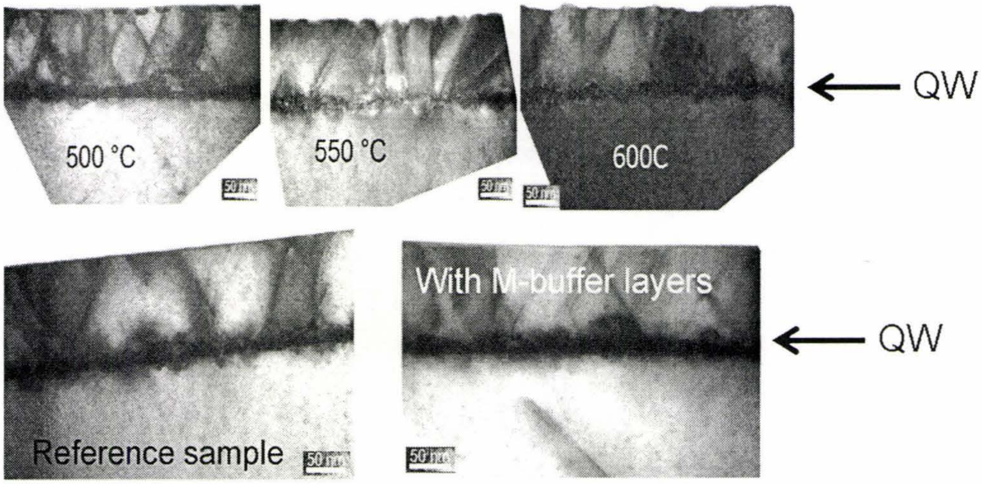

Figure 4.6: InAs quantum well on GaSb layers. Top three: annealed samples; bottom two: samples as grown on a reference sample and on a M-buffer layers.

AFM – Atomic force microscopy was used to study the surface morphology of the samples. The value of rms surface roughness for as-grown samples is 13.5Å because of the rough interfaces between InAs-QW and the GaSb layer. The surface seems to degrade with annealing temperature, e.g. for samples annealed at 600° C, the surface roughness increased to ~ 20 Å. This can be attributed to the presence of a high amount of anti-phase boundaries at the interface of InAs-QW with GaSb which formed due to the non-optimum growth of the interface. However, this roughness does not correspond to the actual surface of the metamorphic GaSb layer, as this layer is buried under the InAs-QW and GaSb cap layer.

The growth of InAs on GaSb, and vice-versa has been shown to be difficult [3] and since it was not required in our final device structures, this was not pursued further.

4.4 Growth and Characterization of InGaSb Metamorphic Layers[*]

The growth schematic for InGaSb metamorphic buffer layers are shown in Figure 4.7.

Growth

All the layers of the metamorphic samples were grown by MBE. The beam pressure of Sb was fixed at ~1.88×10^{-6} Torr, as before, for the entire growth. This pressure corresponds to an antimony flux of 1.3 ML/s on GaSb (see Section 2.3, page 30).

GaSb	40 nm	*Cap layer*
$In_xGa_{1-x}Sb$, $x = 0.15$	1.1 to 1.5 μm	*Metamorphic layer*
$In_xGa_{1-x}Sb$, $x = 0.12$	250 nm	*Buffer layers*
$In_xGa_{1-x}Sb$, $x = 0.09$	250 nm	
$In_xGa_{1-x}Sb$, $x = 0.06$	250 nm	
$In_xGa_{1-x}Sb$, $x = 0.03$	250 nm	
GaSb buffer layer	0.1 to 0.25 μm	
GaSb substrate		

Figure 4.7: Schematic of the InGaSb metamorphic epitaxial structure.

Growth for all samples was initiated on Zn-doped, (001) oriented GaSb substrates and the Ga and In effusion cell temperatures were adjusted to provide a nominally constant

---

[*] Part of this section has been published in [116].

growth rate of ~ 1.0 μm/hr (~0.91 ML/s) for the entire growth. This nominal rate is not corrected for Poisson effects due to strain and partial relaxation to a larger lattice constant during the growth of InGaSb layers. The V/III ratio on GaSb would be ~1.5. Each substrate was de-gassed at 250° C after loading in a preparation chamber and then transferred into the growth chamber where the residual surface oxide was desorbed through exposure to a hydrogen-plasma for 10 minutes with an overpressure of Sb.

Surface reflectivity during desorption was monitored using the SVTA IS4K optical pyrometer. We observed that a reduction in reflectivity values by amounts of $\Delta R \approx 0.03$ to 0.04 are indicative that the substrate surface is contamination-free and ready for epitaxial growth. An example is shown in Figure 4.8 from points 'c' to 'd'. This provides an in-situ monitoring of the surface quality during epitaxy through reflectance measurements. The subtle change observed from 'c' to 'd' has been confirmed with most of the growth runs and hence is not an artifact of the equipment. Along with the reflectivity reduction and time elapsed during desorption, the temperature also plays a crucial role. Carrying out desorption at a substrate temperature of 540-550° C results in a near perfect interface between the substrate and the first grown buffer layer. For example, compared to samples #429 or #359, sample #347 (see XTEM images later in Figure 4.13) was desorbed at about 40° C lower temperature and had a somewhat rougher interface. Thus, complete contaminant removal was established by a reduction in the surface reflectivity along with the substrate temperature of 540-550° C. After desorption, the substrate temperature was adjusted slowly to reach the desired growth temperature. Growth was carried out at temperatures (T_G = 450 – 540 °C) for the various samples as given in Table 4.3 (column 2).

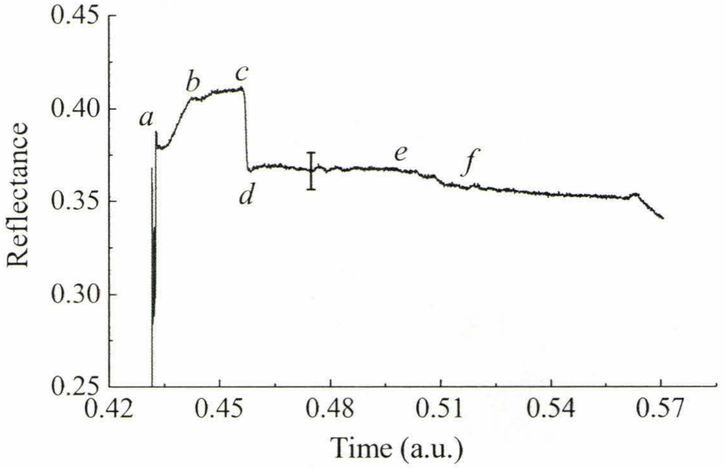

Figure 4.8: In-situ monitoring of reflectivity data for a typical metamorphic growth of InGaSb on GaSb. Desorption starts from 'b', reflectance drops from 'c' to 'd' during desorption, reflectance change between 'e' and 'f' is due to changes in composition during graded buffer growths.

The epitaxial layer structure for the metamorphic sample (see Figure 4.7) starts with a GaSb buffer (0.1 to 0.25 μm) on the GaSb substrate, followed by a sequence of four buffer layers of $In_xGa_{1-x}Sb$ grown at the various temperatures, where the In fraction was incremented in steps of $x = 0.03$. Each buffer layer had a thickness of 250 nm. The step-graded buffer layers were terminated by the final metamorphic layer with composition $x = 0.15$. The thickness of the top metamorphic layer was between 1.1 and 1.5 μm. Finally, a fully strained 40 nm GaSb cap-layer was grown on top of the metamorphic layer for the x-ray characterization as previously described. Sample #61 was grown undoped while the rest of the samples were nominally 2×10^{18} cm^{-3} p-doped by with beryllium (see Section 2.4 for doping details).

Characterization

HRXRD – The composition and degree of relaxation of the metamorphic layers was determined using HRXRD as previously discussed in Section 4.1. In [110], it was shown that a cap layer of thickness as high as 80 nm (approximately four times higher than that permitted by critical thickness) can still remain pseudomorphic on a partially relaxed metamorphic layer. Here, we used a 40 nm GaSb cap layer ($\Delta a/a < 0.7\%$ with respect to the underlying metamorphic layer) to ensure a pseudomorphic layer allowing simple (004) XRD measurements to determine the in-plane lattice constants of the underlying metamorphic layer. Figure 4.10 shows a typical x-ray rocking curve showing two distinct peaks resulting from the partially relaxed InGaSb metamorphic layer and the highly tensile GaSb cap-layer on the left and right of the substrate peak respectively.

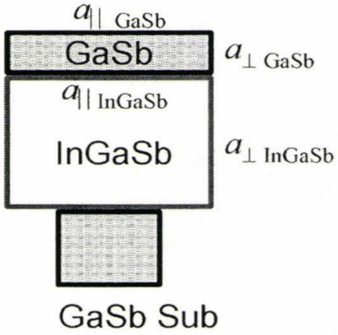

Figure 4.9: A schematic showing the relative lattice constants for the substrate, the metamorphic and the cap layers.

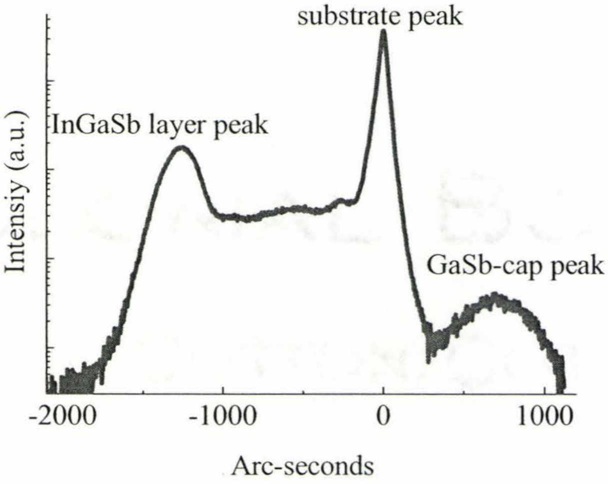

Figure 4.10: Typical x-ray rocking curve (symmetric scan) for InGaSb metamorphic samples.

Since the elastic stiffness constants (C_{11} and C_{12}) are known for GaSb, the position of the peak resulting from the GaSb cap layer relative to the substrate can be used to establish the in-plane lattice constant ($a_{\parallel}$) of the metamorphic layer. Also, the position of the peak resulting from the metamorphic layer allows the perpendicular lattice constant ($a_\perp$) to be determined. These lattice constants are given for each sample in Table 4.3 (columns 3 and 4) averaged over the [011] and $[0\bar{1}1]$ directions. From these lattice constant values, the natural (fully relaxed) lattice constant $a(x)$ for each metamorphic layer can be determined using eq.(4.2) with Vegard's law to interpolate for $a(x)$, $C_{12}(x)$ and $C_{11}(x)$ between the values for GaSb and InSb (see Appendix 1). Solution of eq.(4.2) leads to determination of the composition (x), and then in turn to $a(x)$ and degree of relaxation for the metamorphic layers. The composition and relaxation values are shown in columns 5 and 6 of Table 4.3 respectively. Dynamic simulation of the rocking curves by RADS (rocking analysis by dynamic simulation) software (supplied by BEDE) also confirms the values presented in columns 3 to 6 of Table 4.3.

Table 4.3: Growth temperatures (T_G), layer thicknesses, average values of $a_\perp$ and $a_\parallel$, composition, and relaxation values for InGaSb samples.

T_G (°C)	$a_\perp$ (Å)	$a_\parallel$ (Å)	Composition (x)	Relaxation	RMS surface roughness (nm)	Misfit dislocation density $\times 10^8$ cm^{-2}	Sample
540	6.1622	6.1365	0.142	76%	0.8±0.1	2.4±0.2	#429
530	6.1618	6.1309	0.134	69%	1.0±0.2	2.4±0.2	#359
495	6.1601	6.1336	0.135	74%	_	3.3±0.1	#61
470	6.1653	6.1316	0.140	67%	3.1±0.1	4.9±0.2	#360
460	6.1675	6.1272	0.137	60%	_	_	#347
450	6.1673	6.1288	0.139	63%	3.9±0.4	_	#361

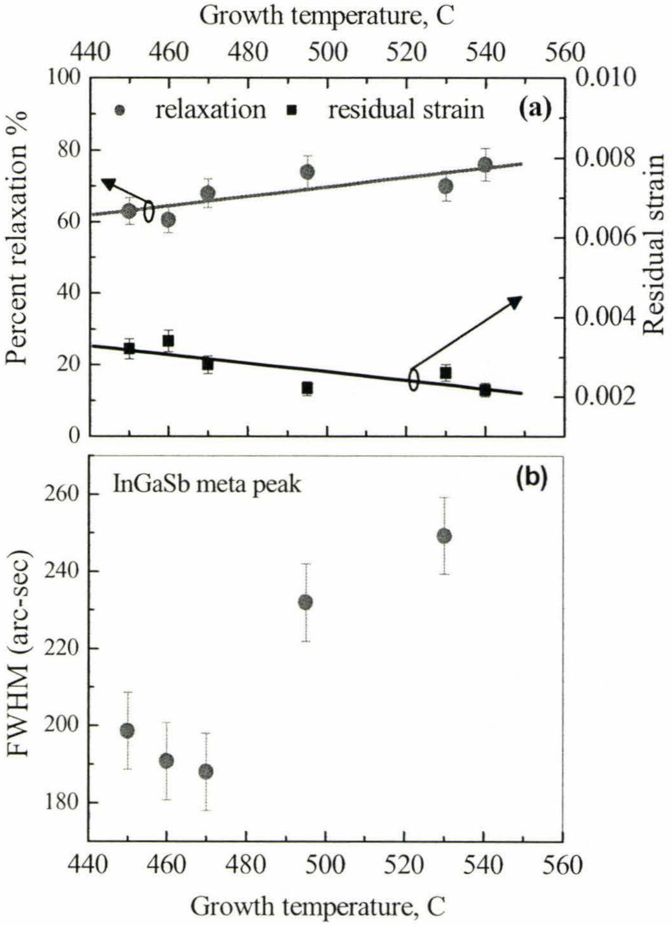

Figure 4.11: (a) Variation of percent relaxation and residual strain with growth temperature for all samples, except #61 and #524. (b) X-ray peak-broadening of InGaSb metamorphic layer with growth temperature.

Figure 4.11(a) shows a plot of the percent relaxation and residual strain with growth temperature for all samples grown (except #524). It can be seen that the relaxation values increase and residual strain decrease linearly as the growth temperature increases from 450° C to 540° C. The full width at half maximum (FWHM) values for the InGaSb metamorphic layer x-ray peaks are plotted with T_G in Figure 4.11(b). A variation of ±10 arc-seconds is observed for these data points due to measurement variations in the directions of [011] and $[0\bar{1}1]$. This figure shows that the peaks broaden significantly for

T_G greater than ~490° C due to increased mosaicity in the metamorphic layers. A similar trend was reported in [117] for InGaSb layers grown on GaSb without any buffer layers.

XTEM and PVTEM – XTEM of each sample was carried out and the resulting micrographs are shown in Figure 4.13 along with their respective growth temperatures. As observed in the previous Section 4.3, dislocations resulting from the lattice mismatch are mostly confined within the buffer layers. It can be observed from these images that dislocation density is lower at higher growth temperature (up to 540° C).For example, samples #429, 61, 360 and 347 (top four micrographs in Figure 4.13) show no observable dislocations penetrating up into the metamorphic layers; whereas, samples #347 and #361 (samples with lower growth temperature) contain a considerable number of threading dislocations as well as stacking faults. This result is consistent with other metamorphic growths, e.g. InAsP/InP [110], InAlAs/InP [31] and InGaP/GaP [78] and was explained in [31] by way of an exponential increase in dislocation velocity with growth temperature which reduces the threading dislocation density promoting better relaxation and surface quality for the metamorphic layer. Also, the buffer layers help to create bigger misfits and hence fewer threading dislocations [105]. This is very different from that reported for InGaAs/GaAs [78], where low temperature growth is prescribed for better quality in terms of reduced dislocation density. Misfit dislocation densities, tabulated in Table 4.3 (column 8) and shown in Figure 4.13 for corresponding samples, were calculated from plan-view TEM (PVTEM) images.

The PVTEM study shows clearly that the misfit dislocation density originating in the buffer layers is considerably reduced for samples #429 and #61 (~ 2.4×10^8 cm^{-2}) grown at higher temperature compared to the sample #360 (~5×10^8 cm^{-2}) grown at lower T_G. The PVTEM image taken at low T_G (sample #347 in Figure 4.13) demonstrates that the nature of the defects is either of threading dislocations or stacking faults. Thus, with increasing T_G, the threading dislocations gradually disappear and misfit dislocations become dominant (see PVTEM micrographs in Figure 4.13). The observed measurement errors in column 7 and 8 of Table 4.3 is due to variation of surface roughness and dislocation density observed across each sample.

AFM –AFM images were taken to study the surface morphology of the samples. Table 4.3 presents the root-mean-square (rms) surface roughness values calculated from 5 μm × 5 μm scan dimensions for each sample. These values show that the surface becomes smoother as the growth temperature is increased. This can be explained in terms of the observed reduction of threading dislocations with growth temperature. Overall surface roughness, when grown with a higher T_G (e.g. samples #429 and #359), is quite smooth (of the order of 1 nm or less) and is comparable to metamorphic layers grown on GaAs reported in [27]. Figure 4.12 shows two AFM images for samples #429 and #360. With a higher growth temperature, the surface of sample #429 looks very smooth; whereas sample #360 has a rough surface with surface pits and troughs resulting from a higher dislocation density. Cross-hatched patterns are also clearly seen on both surfaces which are characteristic for metamorphic layers.

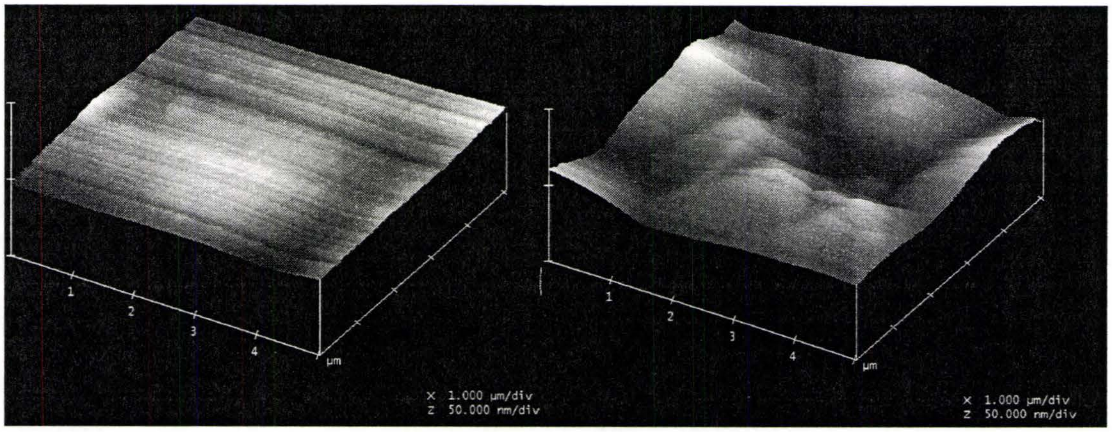

(a) (b)

Figure 4.12: AFM micrographs for samples (a) #429 and (b) #360.

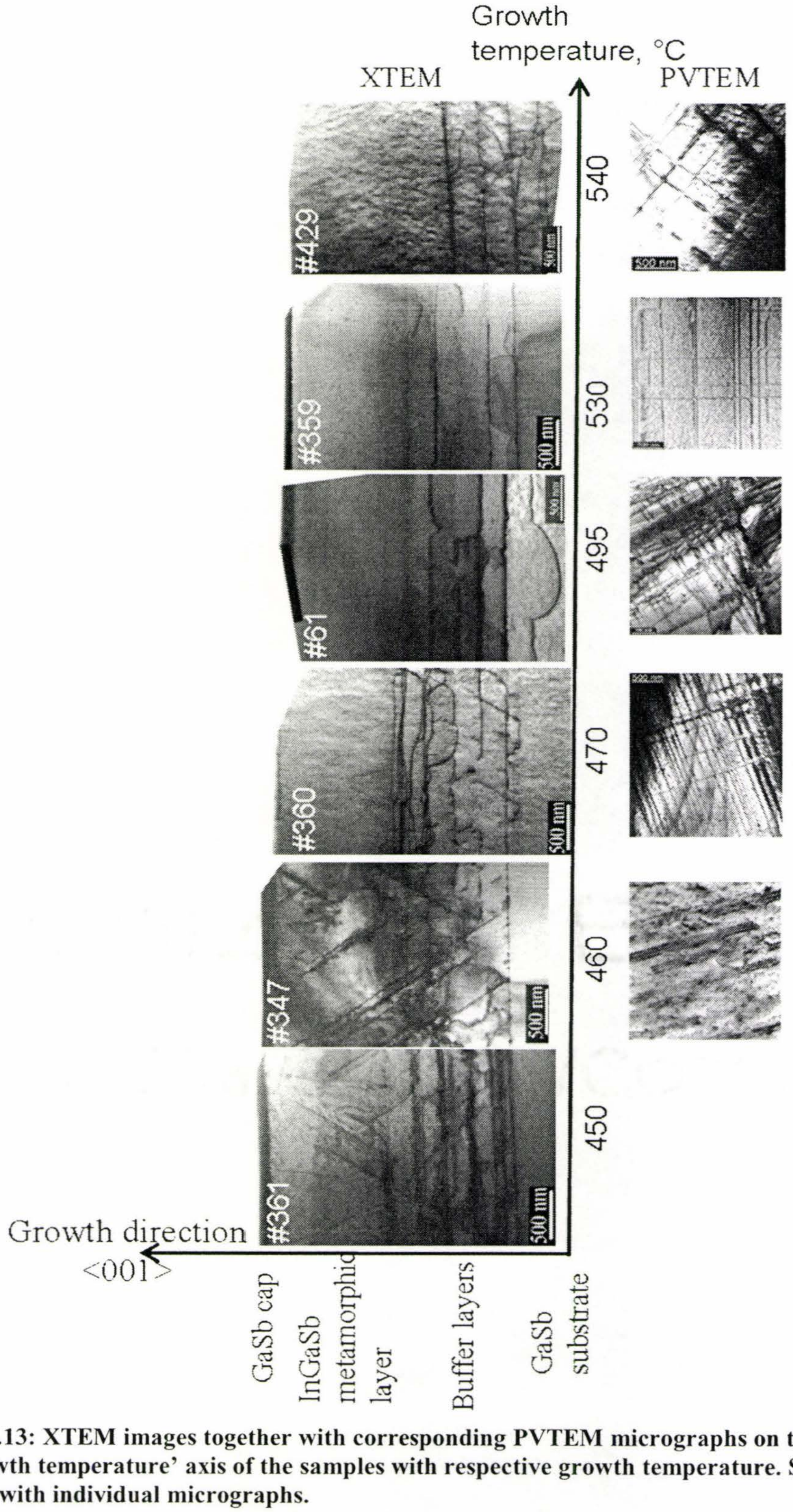

Figure 4.13: XTEM images together with corresponding PVTEM micrographs on the right-side of the 'growth temperature' axis of the samples with respective growth temperature. Sample names are inserted with individual micrographs.

Sample #524

Metamorphic sample #524 was used specifically for the fabrication of photodetectors to operate at wavelengths above 2 μm. This required a target composition for the terminal layer with a somewhat higher In-fraction than the InGaSb samples analyzed above. The buffer layer schematic was also different to allow more gradual change in composition and hence lattice constant. A total of ten buffer layers were grown – each layer had a 2.5% indium increment and was 100 nm thick nominally.

The terminal layer (target composition $x = 0.25$) was nominally 1.0 μm thick ending with a 25 nm GaSb cap layer. The XTEM for this sample is shown in Figure 4.14. The lattice parameters for this sample, inferred from the rocking curve of Figure 4.15, are: $a_\perp = 6.2009$ Å and $a_{||} = 6.1661$ Å, composition (x) – 0.233, relaxation – 80%. All the growth conditions including the growth temperature were similar to that of #429. The XTEM micrographs show that the bulk of the M-buffer was still visibly free from threading dislocations. However, since the strain between the M-buffer and the cap layer was relatively large ($\Delta a/a \approx 1.45\%$ with respect to the underlying 80% relaxed metamorphic layer), the cap layer contained dislocations visible in Figure 4.14. Nevertheless, the x-ray rocking curves were very similar to those in Figure 4.10 and the peaks are still clearly visible in Figure 4.15. Since there are visible presence of dislocations present in the GaSb cap, $a_{||} = 6.1661$ Å calculated from the cap-layer peak will be an underestimate for the actual $a_{||}$ of the underlying M-substrate. RADS simulation suggests that the cap layer is 1% relaxed. This provides a value of in-plane lattice constant (6.1668 Å) for the M-layer. Hence, the subsequent layers grown on top will be lattice-matched with a 18% indium composition.

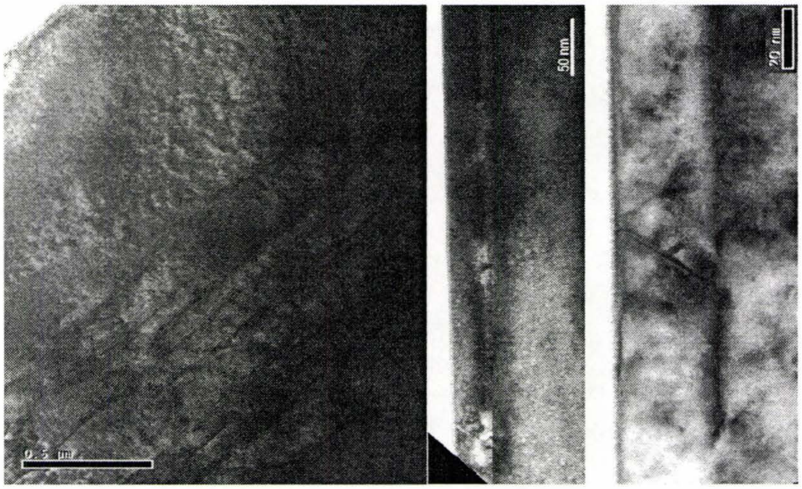

Figure 4.14: XTEM for sample #524. Left micrograph shows the bulk metamorphic layer. The other two, on the right, are showing the cap layer.

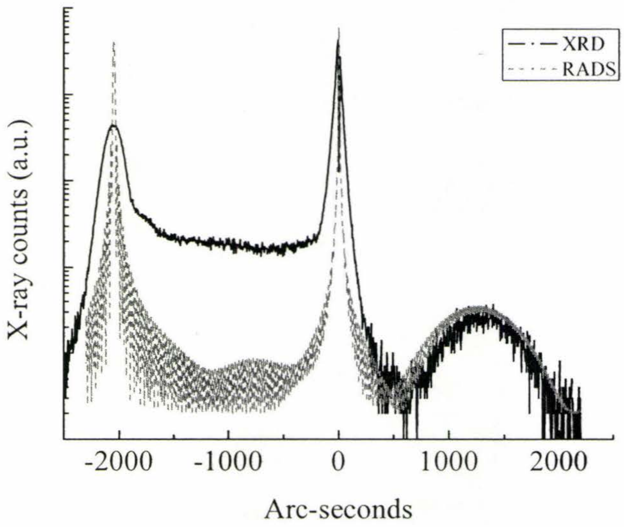

Figure 4.15: XRD data and RADS simulation results for sample #524.

4.5 Summary

The x-ray diffraction technique to characterize the in-plane lattice constants was discussed in this chapter. It is important to know the in-plane lattice constants and the composition for the metamorphic substrates. Once the composition is known, a regrowth of active device layers lattice matched to the underlying M-substrate becomes possible, which opens an opportunity to explore the promising potentials of the 6.1 Å family, as it enables one to grow a ternary or quaternary alloy of arbitrary composition, which suits a particular application, on commercially available substrates. We have successfully grown and characterized the buffer layers of GaAsSb creating a GaSb M-substrate. This technique was then extended to growing metamorphic substrates of InGaSb. Our findings suggest that the growth temperature greater than 500^{o} C results in improved materials quality of the resulting M-substrate by reducing both the threading dislocations and the surface roughness. Care has been taken to measure the peak separation from the rocking curves, so that the resulting error is not greater than $\partial\theta = \pm 20$ arc-seconds that causes an error in the calculated composition by 1% of In-fraction.

Chapter 5 Growth, Fabrication and Characterization of Junction Diodes

In this chapter, growth and fabrication of the InGaSb p-i-n homojunction diodes are described. The growth issues regarding the metamorphic layers (M-buffer) have been discussed in the previous chapter. Active device layers were grown on the metamorphic substrates described and mesa diodes fabricated. The devices were characterized by their I-V dark current behavior and surface leakage with various surface passivation techniques using polyimide and silicon nitride. Our findings indicate that silicon nitride produced better passivation than the polyimide. Theoretical components of the dark current were calculated. Finally, a comparison was made between similar diodes reported in the literature and the present diodes. Optoelectronic characteristics are discussed in the next chapter.

5.1 Growth of InGaSb Diodes on Metamorphic Layers

A total of three diode samples were grown in the MBE – samples #439, #510 and #528. Five sets of diodes were fabricated from these samples and were subjected to different processing steps. Sample #439 was a regrowth of device layers on metamorphic sample #429 (see Section 4.4). Other samples were grown on metamorphic layers very similar to that of sample #429 without any interruption in the MBE chamber. This was done with the expectation that metamorphic layers, grown with MBE conditions similar to #429, will also have similar in-plane lattice constants and hence similar compositions. This assumption was confirmed by post-growth x-ray diffraction study on the final device layers (see later in Figure 5.1 and related discussions). Sample #528 had a higher indium fraction corresponding to the underlying metamorphic layer – to be the same as sample #524 (see page 78). Sample #510 was grown on an n+-GaSb substrate, while the other two were on p$^+$-GaSb. The GaSb substrates were purchased from Wafer Technology Ltd, UK and their doping levels were ~2.4×10^{18} cm^{-3} and ~8.5×10^{17} cm^{-3} for the p- and n-type samples, respectively. Several sample properties are mentioned in Table 5.1. The nominal doping levels throughout were Be – 2×10^{18} cm^{-3} and Te – 1.5×10^{18} cm^{-3} for p and n-type layers, respectively. The gallium telluride crucible was held at 740° C while 850° C was the cracking temperature at the tube. The i-layer was un-intentionally doped and was a p-type layer with background doping density ~ 2.4×10^{16} cm^{-3}.

A cleaved portion of sample #429 was loaded into the MBE after a full materials characterization. Hence, sample #439 was a regrowth on sample #429 and contained active device layers on an already characterized M-substrate. The regrowth was performed without any additional chemical processing of the surface. The desorption temperature was about 540° C as discussed in page 70. This desorption temperature was followed for all samples. For diode samples #510 and #528, the device layers were grown on top of M-substrate with only a short interruption to adjust the In/Ga flux ratio consistent to grow InGaSb with a composition having the identical lattice constant to the M-substrate. After the growth of the M-substrate, the growth temperature was slowly ramped down to ~ 520° C for the device layer growths. For #510, the M-substrate had similar growth parameters to #429 and as such no further materials characterization was performed. The thicknesses of the device layers grown are shown in Table 5.1.

Table 5.1: Details of the diode samples fabricated and the surface passivation technique applied.

Sample #	%In	Mesa height, um	Passivation	Device structure	
#439	10.0	3.9±0.1 μm	Si_3N_4	1.5 μm n^+-layer 2.0 μm UD-layer 0.5 μm p^+-layer	n-i-p
#510	10.0	2.8±0.1 μm	Si_3N_4	1.5 μm p^+-layer 1.2 μm UD-layer 0.1 μm n^+-layer	p-i-n
#510-PI	10.0	2.8±0.1 μm	Polyimide	Same as above	p-i-n
#528	18.2	4.3±0.2 μm	Si_3N_4	1.5 μm p^+-layer 1.5 μm UD-layer 1.0 μm n^+-layer	n-i-p
#528-PI	18.2	4.1±0.2 μm	Polyimide	Same as above	n-i-p

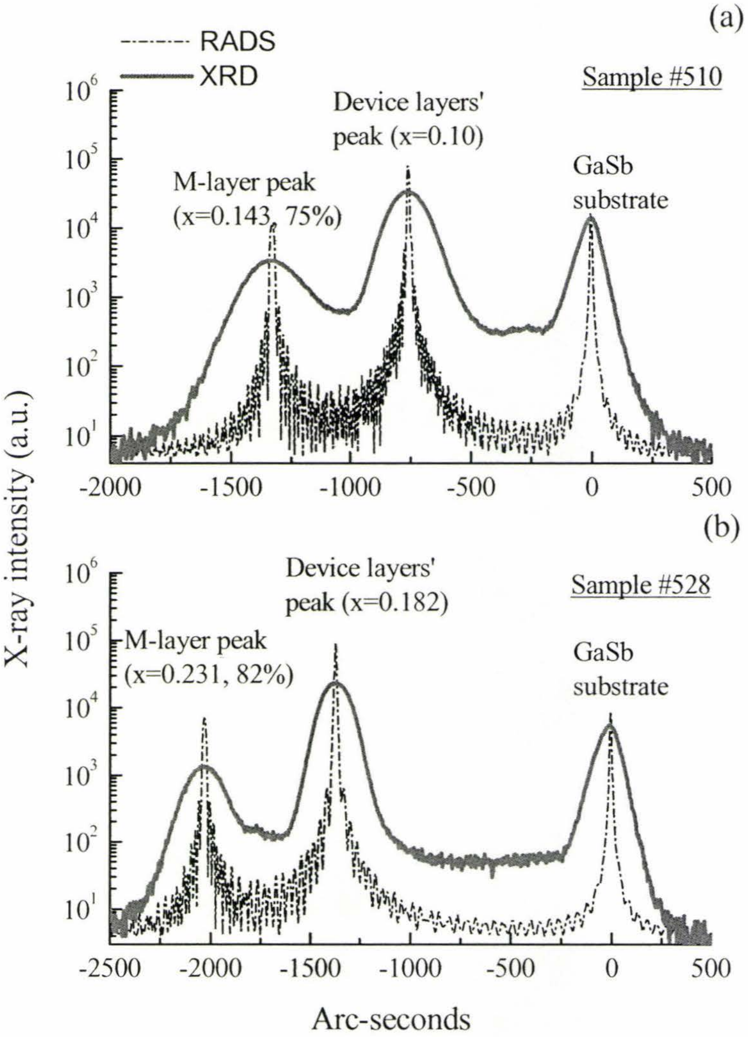

Figure 5.1: X-ray rocking curves and RADS simulation results for samples (a) #510 and (b) #528. Indium fraction and percent relaxation are given in bracket for the M-layer and device layer peaks.

After growth of the device layers, the samples were again characterized by x-ray diffraction using simple (004)-scans. Figure 5.1 (a, b) shows typical rocking curves for samples #510 and #528. The high central peaks corresponds to the thick device layers, the major peaks to the left of this corresponds to the 1.0 μm metamorphic layer, and the major peaks on the right are from the GaSb substrate. The solid line is the actual rocking curve while the dashed lines correspond to the RADS fitting curves. The best fit of the measured peaks to the RADS data for sample #528 yields an 82±0.2% relaxed M-substrate with 23.1±0.2% indium and a device layer containing 18.2±0.2% indium. For sample #510, analysis suggests the device layers have a composition of 10±0.2% indium grown on a 75% relaxed 14.3±0.2% indium containing M-substrate. The composition of the device layers, thus obtained, is shown for each sample in Table 5.1. These values are in close agreement with our previous estimates of the lattice-matched compositions for the device layers discussed in relation to samples #429 in Table 4.3 (page 73) and #524 in page 78. This close match between the estimated and measured values of the compositions confirms the usefulness of the previously discussed x-ray technique for determining in-plane lattice constants and relaxations in the metamorphic layers.

5.2 Mesa Diode Fabrication

The diodes were fabricated using the standard lithography techniques. The process steps are described in detail in Appendix 2. A three-step mask set was used for this process. The mask-set used for this allowed for the fabrication of diodes of different geometry and sizes. Figure 5.2 shows the first-level mask layout along with the corresponding diode sizes. Diodes D3 – D8 had a constant perimeter (400 μm) and D9 – D13 were constant area (10^4 μm^2) diodes. The mask-set contained three separate masks corresponding to three fabrication steps. The first step in the fabrication process was the deposition of a 350 nm thick SiO_2 layer by plasma-enhanced chemical vapor deposition (PECVD). The first mask was then used to define the mesa geometry (Figure 5.3, steps (i) to (ii)). Reactive ion etching was then used (Figure 5.3, step (iii)). The recipe for RIE for all three samples was the same: 150 W microwave power, 100 W rf power, 2.0 mTorr chamber pressure, CH_4:H_2:Ar = 4:16:8 sccm. Time of etching was determined according to the etch depth required: 125 min for sample #439, 85 min for sample #510, 150 min for sample #528. Before taking the samples out of the etching chamber, they were exposed for 30-40 minutes to an O_2 plasma to remove any polymer build-up. A buffered hydrofluoric acid (BHF) etch was used to remove the SiO_2 remaining on top of the mesa structure.

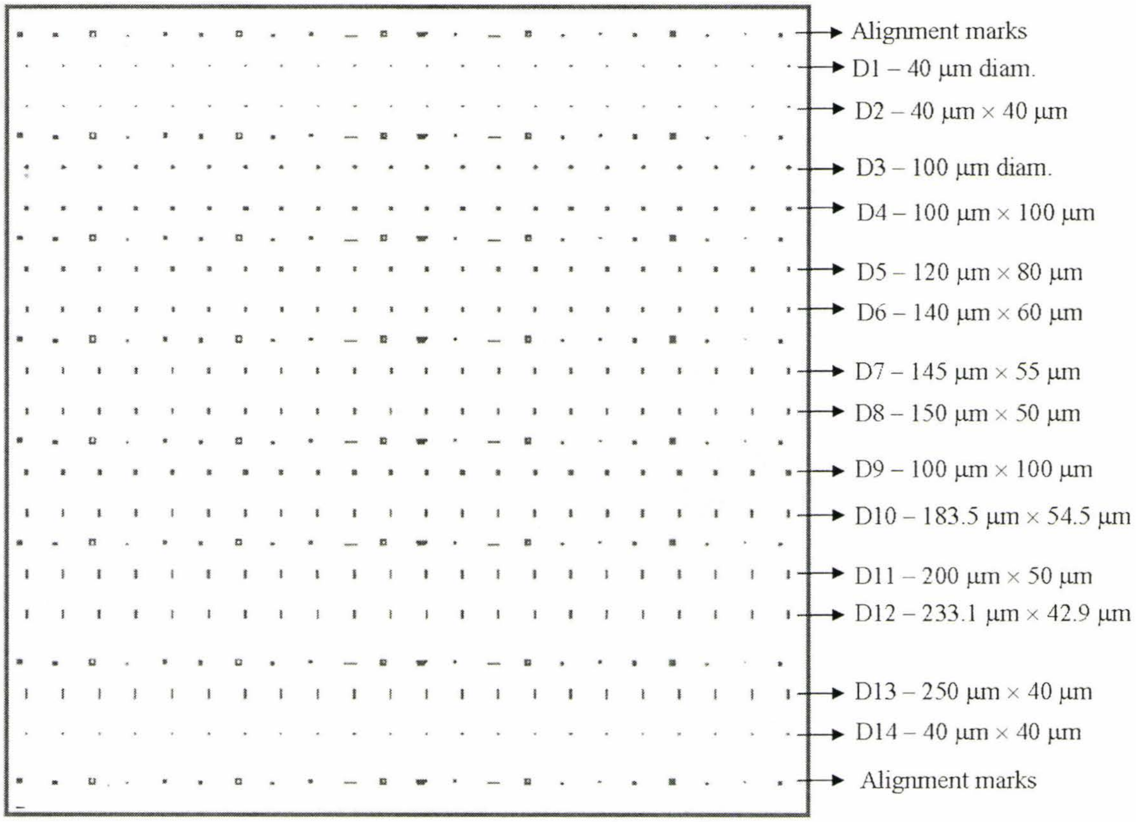

Figure 5.2: A typical mask layout showing the first-level mask along with the diode rows with their corresponding areas. Interspersed with the diode rows are the alignment marks.

At this stage, a 150 nm nominally thick layer of Si_3N_4 was deposited by PECVD for passivating the exposed sidewalls. The second mask was used to define the top optical window with a provision for 5 μm dielectric coverage around the periphery of the mesa. Positive photo-definable polyimide (HD8820 from HD Microsystems) was used at this stage to planarize and encapsulate some diode samples. The third mask was used to define the electrical contact using the lift-off technique which extended 10 μm in from the periphery. This resulted in diodes having a 5 μm of dielectrics along the edge and another 5 μm strip of metal inside the dielectric cover. The rest is the optical window. An example device micrograph for a circular diode is shown in Figure 5.4.

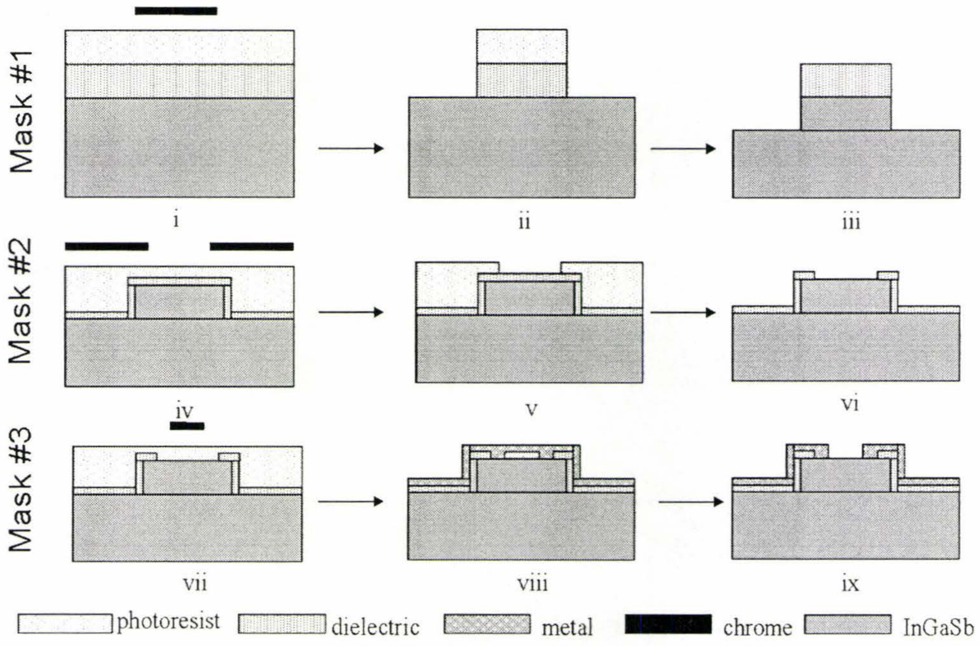

Figure 5.3: Mask set and processing steps for the diode fabrication.

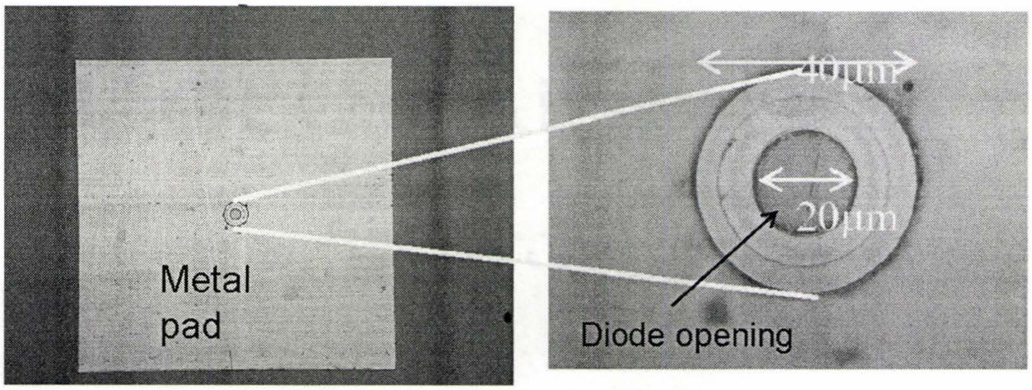

Figure 5.4: Micrograph showing the final device with metal probing pads.

After the third mask process, the device is ready for metallization for the n and p-type contacts. We used Ni/Ge/Au = 250/500/1200Å for n-type contact and Ti/Pt/Au = 250/500/1200Å was deposited for p-type contact. After top-metallization, metal lift-off from the top side of the device was initiated by dipping the device in acetone for overnight soak. Photoresist stripper seems to attack GaSb and produced no improvement on the lift-off process. Q-tips, dipped in acetone, were used to mechanically remove the metals from the optical window area of the devices. After top metal lift-off, the back contact metallization was deposited over the entire back surface of the substrate. The contacts were then annealed in a rapid thermal annealing (RTA) furnace in dry a nitrogen environment and silicon proximity caps to alloy the metal contacts. The annealing temperature was 350° C, being careful to keep below the Au-Si eutectic temperature of 370 °C, for 20 (or 30s). Steps 1 to 12 in Appendix 2 were followed with appropriate adjustments for both mask #1 and #2. For mask #3, which was for metal lift-off, steps 13 to 17 in Appendix 2 were followed.

5.3 Characterization of Junction Diodes

Mesas of different heights (see Table 5.1) were etched by reactive ion etching. A schematic of the device layers are shown in Figure 5.5 along with top and bottom ohmic contacts. Some mesa diodes had their sidewalls passivated by sulfur treatment followed by encapsulation with HD8820 polyimide (from HD Microsystems). Samples #510-PI and #528-PI were passivated and encapsulated with polyimide. Sample #510-PI had additional sulfur passivation of the surface prior to polyimide deposition; this was carried out after the RIE process by rinsing in BHF and de-ionized water followed by immersion in an ammonium sulfide solution ($(NH_4)_2S:H_2O = 1:4$) with a pH-level of 9.5 for 25 min at room temperature. This was followed by routine procedure (as in Appendix 2) with the second mask with the photoresist replaced by HD8820. After exposure (~ 305 mJ) and development in TMAH (MF319), the polyimide was cured on a hot plate: at 200°C for 10 min, then ramped to 350° C and held for 1 min followed by a gradual cool-down to room temperature. Sample #528-PI was processed without sulfide passivation, so the polyimide was in direct contact of the sidewalls.

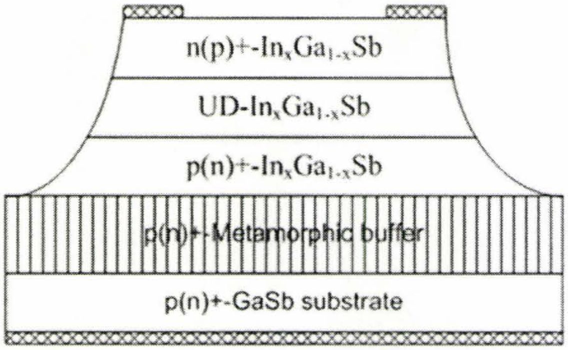

Figure 5.5: A generic device schematic.

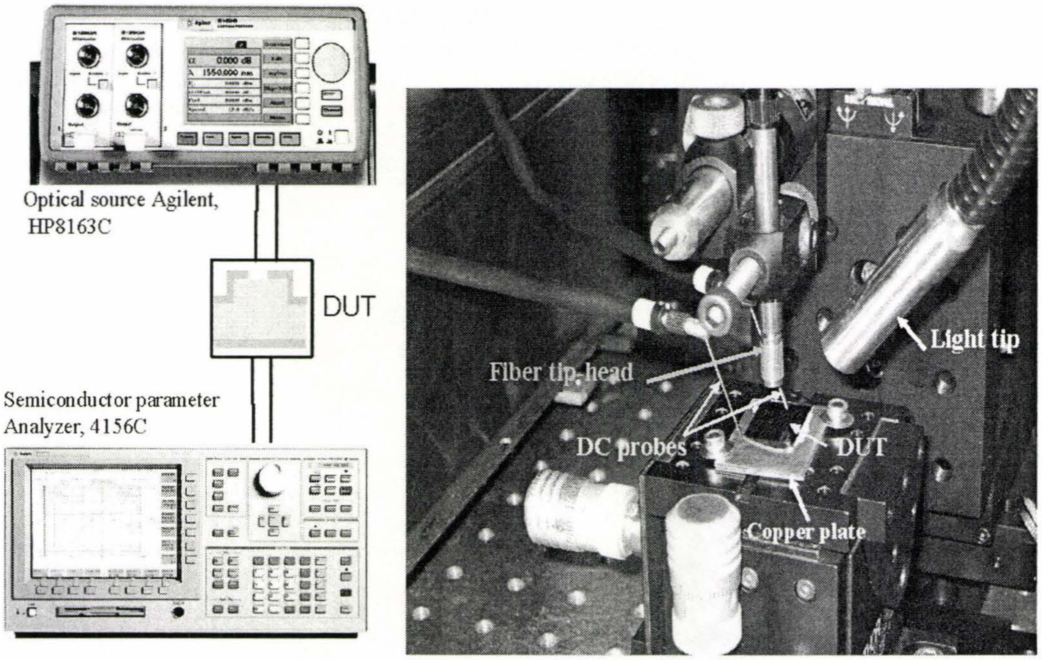

Figure 5.6: Experimental set-up for diode measurements.

The sample with the devices was then mounted on a copper chuck with conductive silver epoxy which served as bottom contact. Probes were applied to the top metal pads. Current-voltage measurements were performed by an Agilent 4156C precision semiconductor parameter analyzer. The experimental set-up is shown in Figure 5.6.

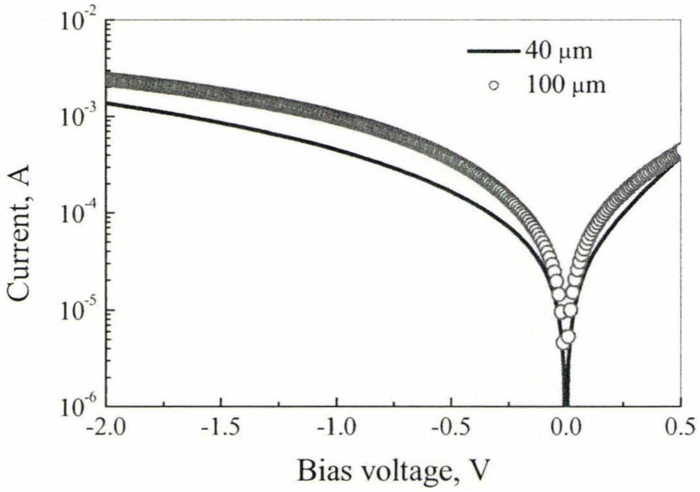

Figure 5.7: Current-voltage characteristics for two square diodes of 40 μm (D2) and 100 μm (D4) size for sample #439.

Figure 5.7 shows typical current-voltage curves for 40 μm and 100 μm square diodes having the largest and the smallest perimeter-to-area ratio (*p*/*A*) respectively among the diodes fabricated with sample #439. Current-voltage curves for a 100 μm × 100 μm square diode from all five diode samples described in Table 5.1 are shown in Figure 5.8 for comparison. It is evident that the dark current characteristics for the polyimide processed samples (#510-PI and #528-PI) were identical to each other and exhibited a higher leakage current than those passivated with silicon nitride. Neither the sulfur passivation nor the polyimide encapsulation could improve the surface leakage.

Figure 5.8 shows that silicon nitride passivation improves the dark current density by passivating the exposed reactive mesa sidewalls. Dark currents were almost the same for samples #439 and #528 which were grown on the same p-substrates. Also, the dark current was somewhat higher for diodes grown on an n-substrate (sample #510) which is seen by comparison to dark current characteristics for samples #528 or #439. This may be attributed to small variations in the process steps and/or to the difference in the substrate doping (see Figure 5.15 and the following discussion on page 97).

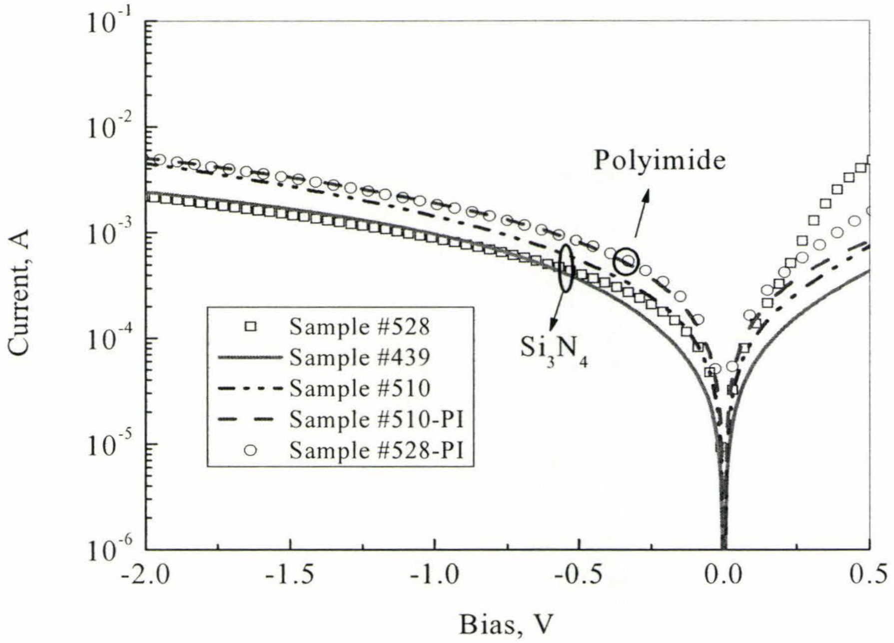

Figure 5.8: Current-voltage curves for all five sets of diodes at room temperature with diode area 100 µm × 100 µm.

Temperature, Capacitance and Reliability

Effect of temperature on current density was also measured. The heating was performed by putting the device-under-test (DUT) on a flexible heater (KHR-2/10). The temperature was monitored by a thermistor. The dark currents both at room temperature and 90° C are shown in Figure 5.9 indicating that higher temperature increases the dark current.

Capacitance-voltage measurements are done by a HP4194A impedance analyzer and shown in Figure 5.10 for a 40 µm × 40 µm square diode. For comparison, capacitance values for diodes with polyimide passivation from reference [138] are also shown. It seems that Si_3N_4 passivation results in a more uniform junction capacitance under reverse bias than polyimide.

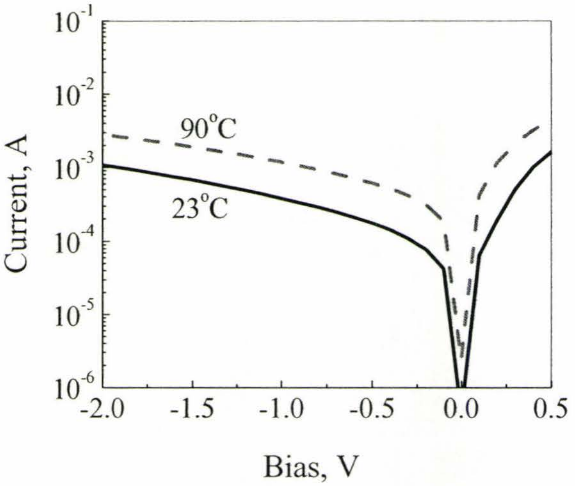

Figure 5.9: Temperature effect on dark current for 100 μm × 100 μm diode.

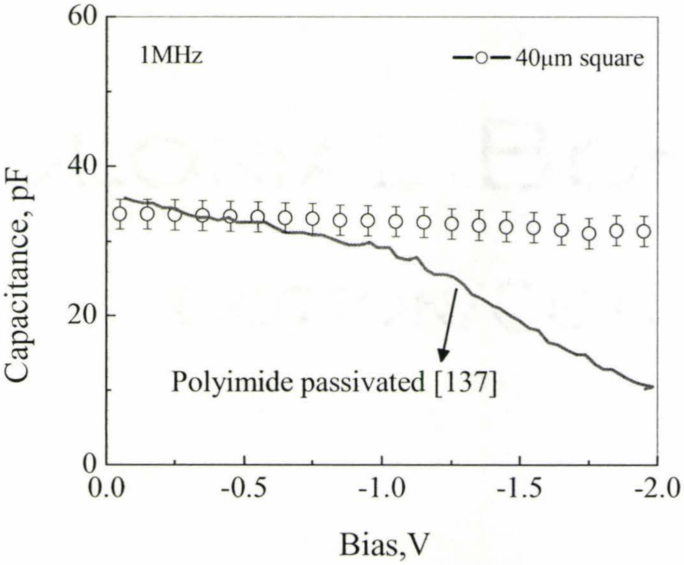

Figure 5.10: Measured capacitance for diode D14 in sample #439 along with those from ref[138].

Stability of the diodes over time was also tested. The inverse zero-bias-resistance-area product for a typical 100 μm × 100 μm square diode is plotted in Figure 5.11 for devices immediately after fabrication and after ~4 months sitting at room temperature. This shows that the silicon nitride passivation results in reproducible diode behavior.

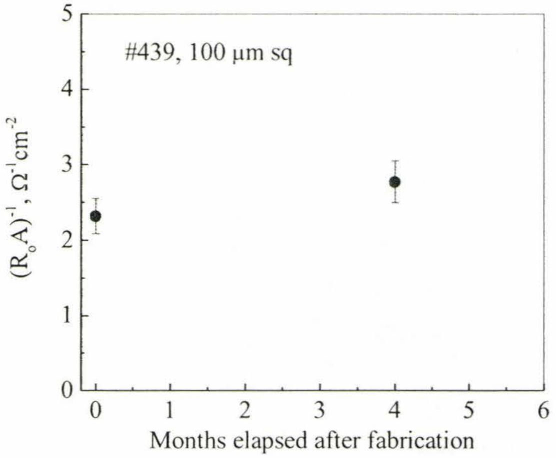

Figure 5.11: Reliability of the silicon nitride passivated diodes.

5.4 Extraction of Area/Perimeter Components and Surface Passivation

One way to estimate the surface or perimeter related losses is to calculate the zero-bias-resistance-area product (R_oA), which is defined as the inverse-slope of the J-V curve [108]:

$$\frac{1}{R_oA} = \left.\frac{dJ}{dV}\right|_{0V} \tag{5.1}$$

This resistance R_0 consists of a combination of shunt resistances across the junction. These shunt paths can be caused by various transport mechanisms, such as diffusion of minority carriers, generation-recombination of thermally generated carriers in the depletion region, tunneling (band-to-band or trap-assisted), and surface leakage [130]-[131]. For an ideal diode, the reverse leakage current is minimal, hence the slope of the J-V curve would be zero or very small (Figure 5.12(a)). Whereas, for a leaky diode where the reverse leakage is high, the slope is high, as illustrated in Figure 5.12(b). Accordingly, a diode with higher leakage in the reverse bias is characterized by a small R_oA product. Typically, a high value of R_oA ensures high injection efficiencies. Thus, R_oA parameter can be used to estimate the surface leakage component for leaky diodes.

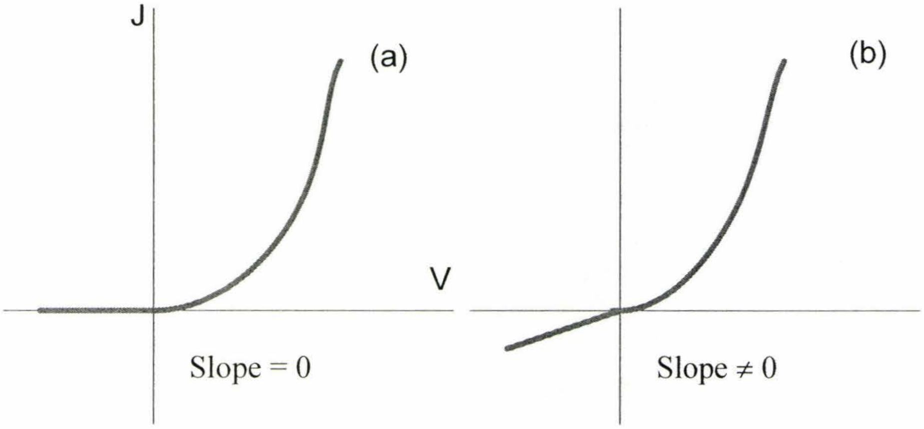

Figure 5.12: Current-density variation with voltage for (a) ideal and (b) leaky diodes. Slopes are drawn at the origin.

The perimeter-related current is associated with a high density of surface or interface states at the semiconductor-air or semiconductor-passivation interface. Thus, smaller-area diodes will be more sensitive to perimeter or surface effects than diodes of the same shape but a larger size. The perimeter-to-area ratio (*p/A*) is inversely proportional to the diode feature sizes and hence magnifies the surface or perimeter related issues when parameters such as current densities or $1/R_oA$, are plotted against *p/A*. Figure 5.13 shows the variation of the reciprocal zero-bias-resistance-area product ($1/R_oA$), with perimeter-to-area ratio for four sets of diodes. This shows that for smaller diodes, the surface leakage dominates the dark current behavior [133]. The total or effective zero-bias-resistance-area product for the diodes are given by [135]:

$$\frac{1}{R_o A} = \frac{1}{\left(R_o A\right)_{\text{bulk}}} + \frac{1}{r_s} \cdot \frac{p}{A} \tag{5.2}$$

where r_s is the surface resistivity in Ω-cm for the diode and is obtained from the inverse-slope of the linear fit for data points for $1/R_oA$-vs-*p/A*. Whereas, the intercept of the linear fit with the $1/R_oA$-axis gives the value of the bulk component of the total R_oA ; i.e. $(R_o\mathrm{A})_{\text{bulk}}$.

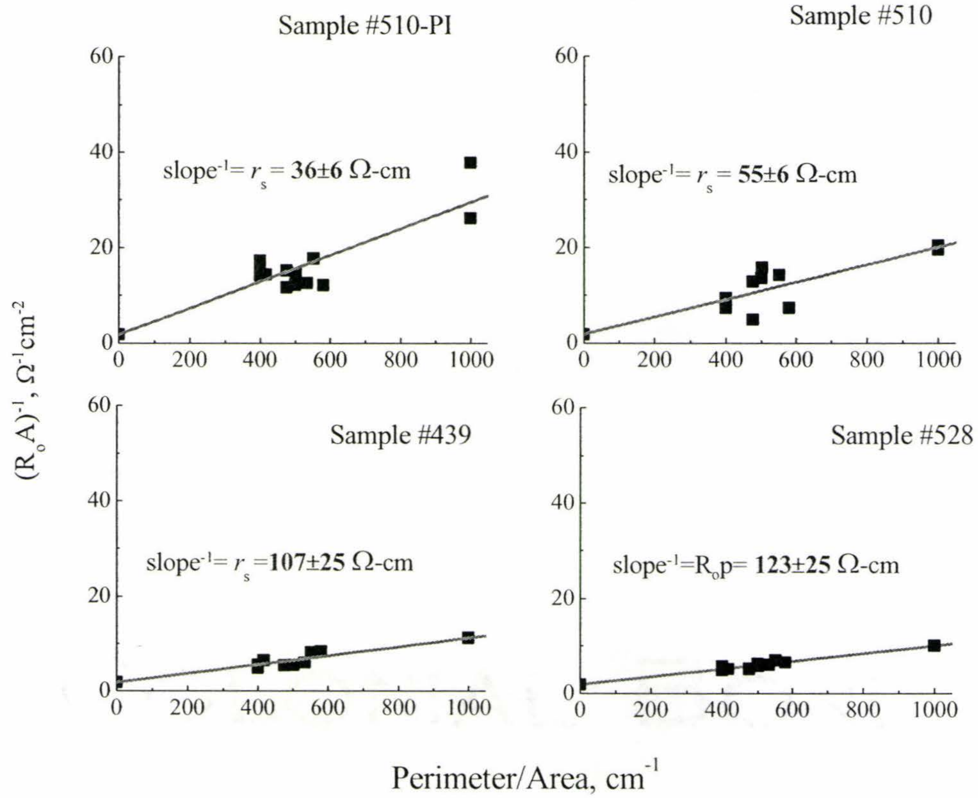

Figure 5.13: Inverse R_oA product vs the perimeter-to-area ratio for four diodes. Lowest surface resistivity (r_s) occurred for the polyimide encapsulated diodes. The bulk-R_oA value was 0.53 Ωcm^2.

For the measured diodes, the bulk component ($(R_oA)_{bulk}$) is fixed at 0.53 Ω-cm^2. This value is obtained, following the procedure outlined in [137], from the diode sets of sample #528, which resulted in the lowest current densities and highest R_o values, and was fixed for all other sets. When compared to those diodes with SiO_2 passivation ($(R_oA)_{bulk}$ = 0.08 Ω-cm^2) in [135], the present value is high. As seen in Figure 5.13, surface resistivity (r_s) was lowest for the polyimide passivated diodes (sample #510-PI) and increased significantly for the Si_3N_4 passivated diodes belonging to samples #439 and #528. Both of these diode-sets were grown on p-substrate. The diodes (sample #510) grown on an n-substrate (which had a lower doping density) exhibited a higher leakage current. This could arise from a higher defect density present in the substrate (etch pit density: 923 cm^{-2} for n-substrate and 803 cm^{-2} for p-substrate) or from less complete cleaning of the substrate prior to the epitaxial growth. Also, the noticeable reduction in data-point scatter is noted arising from the more effective passivation using the Si_3N_4. Within a sample, the R_oA values vary from one diode to another of the same area and perimeter, causing variability in the slopes of $1/R_o$A-vs-p/A curves. For example, values of R_oA vary by 10% from the average for D4 diodes (with smallest p/A-ratio), and 20% for D2 diodes (with highest p/A-ratio) in samples with Si_3N_4 passivation (#439 and #528). Whereas, this variation is 20% for D4 and D2 diodes in samples with polyimide passivation (#510). This error has been estimated for the diodes of Figure 5.13 and shown as a variation in r_S. Within a sample, the variation observed in R_oA from diode-to-diode is caused by improper cleaning during fabrication, damage during lift-off, non-uniform plasma damage during etching etc.

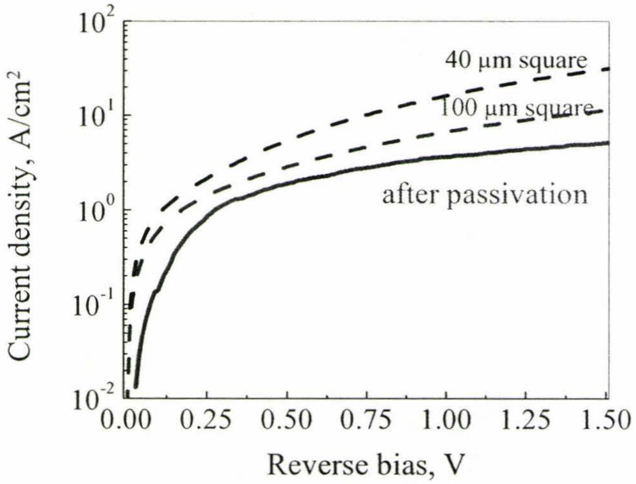

Figure 5.14: For diodes of sample #439: extracted area component in comparison with the measured current densities.

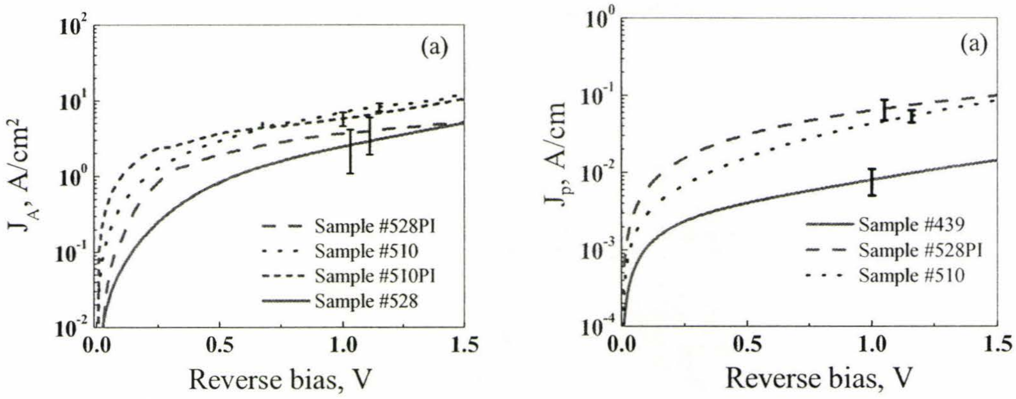

Figure 5.15: Area (a) and perimeter (b) component extraction.

An alternative approach for isolating the perimeter component of the diodes is to solve the following equation [136]:

$$I = J_A A + J_p P \tag{5.3}$$

here, I is the total current at voltage V, J_A and J_P are the area and perimeter current density components, respectively; A being the area and P the perimeter of the diodes. This equation can be solved for two or more diodes of different area and perimeter and the area and perimeter components can be determined. Once the perimeter component is extracted from the total current, the bulk component (J_A) of the dark current density, free of any surface leakage, can be estimated using eq.(5.3). Figure 5.14 shows the bulk component of the dark current density that would result from a leakge-free fabrication process in relation to the actual current densities measured for #439. Figure 5.15(a) shows the area component (J_A) for four diodes. This shows that the area leakage component for the diodes from samples #510 grown on an n-substrate (both for Si_3N_4 and polyimide passivated samples) were higher compared to those from #528 which were on p-substrate. The n-substrate doping was 8.5×10^{17} cm^{-3}. Figure 5.15 (b) shows the perimeter component (J_P) for three diodes. This shows that the perimeter leakage was higher for diodes grown on an n-substrate (#510) and those with polyimide passivation grown on p-substrate (#528-PI) compared to those grown on p-substrate and Si_3N_4 passivated (#439).

This study shows that for diodes on n-substrate (#510 and #510-PI), both the area and the perimeter component of the leakage current were higher. This is the reason why dark I-V (Figure 5.8) from sample #510 was higher even though they were Si_3N_4 passivated. High perimeter leakage for the polyimide passivated #428-PI in Figure 5.15 (b) confirms that polyimide passivation resulted in significant perimeter leakage. This observation confirms the results of Figure 5.13 and the discussions therein.

Surface leakage

Surface leakage is an important issue regarding GaSb-based photodetectors. Bulk GaSb typically has a high concentration of Ga_{Sb} anti-site defects which act as a dominant residual acceptor, making it p-type if undoped [73]. The dark current in diodes fabricated in GaSb and its compounds are dominated by leakage mechanisms that originate from the reactive GaSb surface. This issue has been discussed in the literature with some possible remedies [119]-[123],[135],[137],[138]. As discussed in [120], an oxide layer forms at the GaSb surface through the following reaction:

$$2GaSb + 3O_2 \rightarrow Ga_2O_3 + Sb_2O_3$$

This antimony oxide then reacts with more GaSb to create elemental Sb on the surface through the reaction:

$$2GaSb + Sb_2O_3 \rightarrow Ga_2O_3 + 4Sb$$

This is a spontaneous reaction that can occur in room temperature. Hence "a GaSb surface exposed to air will form a native oxide layer and a fraction of a monolayer of free Sb"[120]. This free antimony results in a conducting channel around the junction, thereby causing a possible low resistance shunt path. The oxide dangling bond remaining on the surface, if not neutralized, creates interface states in the forbidden gap which act as additional generation-recombination centers. Thus, a highly reactive surface increases the dark current and reduces the zero-bias resistance of the diode. Foreign absorbents and process contaminants can further deteriorate the dark current characteristics by introducing additional trap levels. In order to prevent the formation of a conducting antimony channel and to neutralize the dangling oxide bonds (which are exposed by etching and process steps), researchers have introduced "chemical, chalcogen-based passivation, dielectric passivation (SiO_2, Si_3N_4), and high bandgap semiconductor regrowth passivation. The chalcogen-based passivation, though initially effective, does not address the practical issue of physical protection and encapsulation of the device [and there are some reports] on the temporal instability of such a passivation layer. Dielectric passivation [on the other hand] presents the challenge of developing high-quality, low-fixed, and interfacial charge density dielectrics at process temperatures substantially below the material growth temperature... . Arguably the most elegant solution is the subsequent regrowth of a lattice-matched, large bandgap semiconductor over etched mesa diodes. This technique, however, requires very careful surface cleaning and preparation prior to the regrowth step and its feasibility in very high fill-factor focal plane arrays has not been demonstrated" [137].

We have experimented with sidewall passivation by SiO_2 (used to passivate highly leaky GaSb diode prototypes not included in this thesis), Si_3N_4 and polyimide. It is our finding that Si_3N_4 results the best passivant among these three. The observed leakage even after the Si_3N_4 passivation is due to processing steps involved in the fabrication. Particularly the RIE process, subsequent annealing at high temperatures are the likely candidate for leakage observed in the present sets of diodes. There is a controversy about polyimide passivation – some groups [135], [137],[138] have claimed to have better performance after polyimide passivation and encapsulation. While in other work polyimide capping has not been found to be successful, possibly due to carbon contamination on the side-walls that increases leakage currents [139]. Our observation also supports this view. Polyimide provides an encapsulation around the exposed mesa-walls against mechanical damage and requires a simple spin-on to be deposited on the diodes, and is thus advantageous compared to silicon nitride that requires a CVD-type deposition technique.

Comparison

Dark current densities are compared in Figure 5.16 between one sample of the present diodes of area 100 μm × 100 μm with that from Ref [133]. The observed difference is mainly process-related and due also to the presence of misfit dislocations in the present diodes as a result of their growth on a metamorphic epitaxial substrate. PN junction diodes of InGaSb with various compositions were previously reported either grown on GaSb by the MOCVD technique [134] or directly on an InGaSb substrate by the vertical Bridgman technique [133]. At -1.0 V reverse bias, current densities from 0.59 to 1.55 A/cm^2 are reported in reference [134] and 0.7 A/cm^2 for a 150 μm diode reported in reference[133]. The present homojunctions with a longer mesa-sidewall had a current density of 3.4 A/cm^2 at -1.0 V reverse bias for the 100 μm square diode shown in Figure 5.16. However, the present diodes have current densities comparable to those reported in [142].

Further comparisons are shown in Table 5.2. It has been established that for GaSb-based materials, surface leakage is the main contributing mechanism for dark current [119]-[123]. Also, the misfit and/or threading dislocations in the bulk metamorphic layers contribute to the dark current we measured. These two mechanisms are responsible for our measured higher dark current density. However, with a suitable surface passivation technique (page 98), it is possible to fabricate diodes with better dark current characteristics on a metamorphic platform.

Table 5.2: Comparison of diode parameters.

	Current density at -1.0 V, A/cm^2	Surface resistivity r_s, Ω-cm	R_oA, Ω-cm^2	Comments
Present diodes	3.4±1.0	123±25	0.203±0.02	100 μm square mesa p-i-n InGaSb on metamorphic layers
Ref [133]	0.7	813	3.85	150 μm diameter mesa PN InGaSb on custom substrate
Ref [142]	3.93	_	_	180 μm diameter disk mesa N+P-$In_{0.4}Ga_{0.6}Sb$ on GaSb

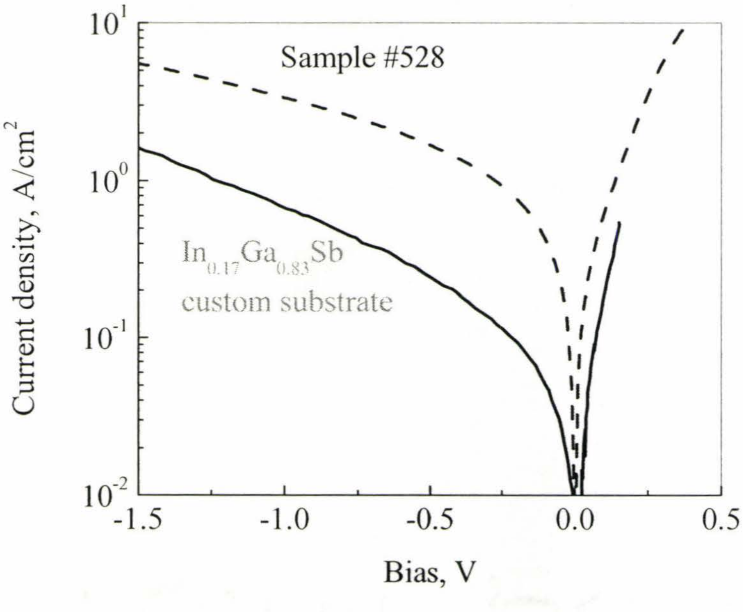

Figure 5.16: Comparison of dark current density between present diodes and a 150 μm diameter circular diode in Ref [133].

Diodes reported in [133] are fabricated on a custom-made substrate of InGaSb with similar compositions. The present diodes are limited by surface leakage, which is evident from the comparison of the surface resistivity (r_s) in Table 5.2. In addition, the misfit and/or threading dislocations in the bulk metamorphic layers also contribute to the dark current for the present diodes. These two mechanisms are responsible for higher dark current density on the reverse bias and a high series resistance in the forward bias of the diodes. However, if the surface passivation technique can be further improved, it should be possible to fabricate diodes with good dark current characteristics on a metamorphic platform.

5.5 Theoretical Analysis of Dark Current Components

This section deals with the calculation of theoretical currents for the various mechanisms that contributes to the dark current on reverse bias. The main mechanisms of carrier transport in a reverse bias homojunction diode is diffusion of minority carriers (J_{diff}), generation current (J_{GR}), tunneling (trap-assisted and band-to-band) and surface leakage (J_{shunt}). In the literature, the following equations are used to calculate each current component [124] – [129]:

$$J_{\text{diff}} = qn_i^2\left(\frac{1}{N_A}\sqrt{\frac{D_n}{\tau_n}}+\frac{1}{N_D}\sqrt{\frac{D_p}{\tau_p}}\right)\left(\exp\left({}^{qV}\!/_{kT}\right)-1\right) \tag{5.4}$$

$$J_{\text{GR}} = \frac{qn_iW}{\tau_{GR}}\left(\exp\left({}^{qV}\!/_{2kT}\right)-1\right) \tag{5.5}$$

$$J_{\text{Shunt}} = \frac{B_sVT^{3/2}}{A}\exp\left({}^{-E_g}\!/_{2kT}\right) \tag{5.6}$$

where A is the area, W is the depletion width at a bias voltage V, n_i is the intrinsic carrier concentration, N_A ($2.4\pm0.2\times10^{16}$) and N_D ($1.5\pm0.2\times10^{18}$) are acceptor and donor densities respectively, E_g the bandgap energy, D's and τ's are minority carrier diffusion constants and lifetimes, $F(V)$ is the field over W and B_s is a fitting parameter. The mobilities, measured at the corresponding donor and acceptor concentrations, are: μ_p = 740±40 cm^2/V.s and μ_n = 2164±30 cm^2/V.s (see Section 2.4). The corresponding D's and diffusion lengths L's can be calculated using the Einstein relation: $D/\mu = kT/q$, where $\tau_{n,p}$ = 1.0 ns [143] was used.

While there is no comprehensive formulation to model the leakage current originating from the dislocations, some researchers [144] model them as possible recombination center and then investigate their effect on lifetime. This shortened lifetime affects the recombination velocity. The carrier recombination velocity in unpassivated and passivated GaSb are 8×10^4 cm/s and 5×10^2 cm/s respectively [2]. Assuming threading dislocations increase this velocity, we have estimated the lifetime due to dislocations as 0.7/N (s) for n-type and 2.5/N (s) for p-type material where N (cm^{-2}) is the dislocation density [145]. This lifetime was related to surface recombination velocity through: $\frac{1}{\tau} = \frac{1}{\tau_0} + 2\pi masN$. The generation-recombination lifetime is τ_o = 15 ns (GaSb). Here m = 1, indicating that the radius of dislocation is equal to lattice constant a. The contribution to dark current, from a layer of thickness t, is [144]: $\frac{1}{R_s} = {2\pi q^2 n_i smat}/{kT}$. If there are dislocations of density N, within this thickness, then: $\frac{1}{(R_o A)_s} = \frac{N}{R_s}$. The current density component originating from this contribution to the total R_oA is:

$$J_{\text{disl}} = \frac{V}{(R_o A)_s} \tag{5.7}$$

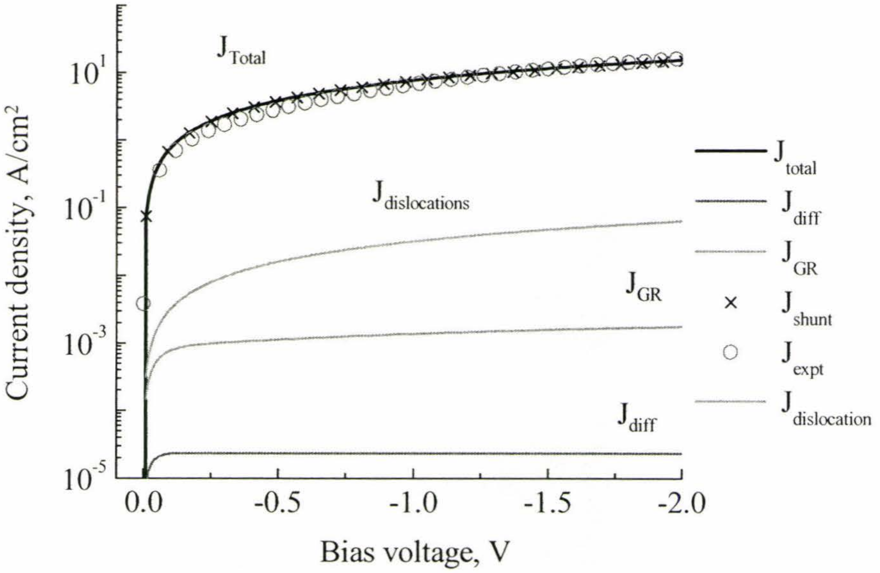

Figure 5.17: Calculated theoretical components of the dark current.

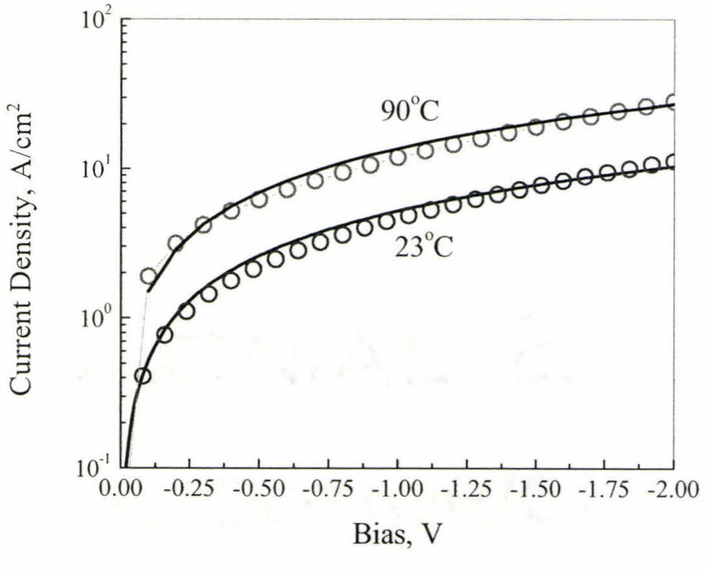

Figure 5.18: Dark current density at room temperature and at 90°C. Theoretical calculations are shown in solid lines.

The current densities calculated through equations (5.4) to (5.7) are shown in Figure 5.17. This shows that the principal mechanism for carrier transport under reverse bias is surface leakage for these diodes. All other components are orders of magnitude lower than the surface leakage. This also confirms our findings in the previous section (see Figure 5.13). These calculations were extended to include the current components for elevated temperature of 90° C as well and are shown in Figure 5.18. The measured current densities are those from Figure 5.9. The fitting parameters (B_s) for the shunt component are shown in Table 5.3 and are compared with that from reference [128] showing similar variation with temperature. All the four current components are higher at elevated temperature resulting in a higher dark current. We have found no significant contribution from the trap-assisted tunneling or the band-to-band tunneling mechanisms within the ranges of bias voltages investigated.

Table 5.3: Comparison of fitting parameter B_s in eq.(5.6).

Fitting parameter B_s			
Present diodes		InSb [128]	
363 K	2.5 (±0.2) $\times 10^{-7}$	125 K	5×10^{-3}
296 K	1.8 (±0.1) $\times 10^{-6}$	100 K	5×10^{-2}

5.6 Summary

This chapter described the fabrication and characterization of InGaSb homojunctions metamorphically grown on GaSb substrates. Several diode test-structures were fabricated using standard lithography. Polyimide and Si_3N_4 were used for surface passivation. It is our finding that the latter is a better passivant improving dark current characteristics of the diodes. The zero-bias-resistance-area (R_oA) products were determined for the diodes and were plotted against perimeter-to-area ratios to extract the effects of the periphery. The effects of temperature on the dark currents were investigated. Theoretical calculations show that the diode dark current was dominated by shunt components originating from the imperfect interface of the exposed mesa sidewalls. Present diodes were then compared with similar ones from the literature. The R_oA-product for the present diodes need further improvement by optimizing the process related steps involved. This will then improve the diodes' dark and optical characteristics. Diode characteristics were measured after four months of fabrication and still showing excellent reliability.

Chapter 6 Optoelectronic Characterization: Responsivity, Detectivity and Ionization Coefficients

This chapter describes the optical characterization of the photodiodes mentioned in the previous chapter. The optical responsivity, and the temperature and bias dependence of the detectivity of the diodes were measured. Also the electron and hole ionization coefficients were determined and their dependence on temperature and composition was investigated. Finally, the temperature dependence was modeled to extrapolate the ionization properties at any arbitrary temperature.

6.1 Optical Response

Optical measurements were done by pulsed illumination of the top window of the diodes. Figure 6.1 shows the resulting current pulse generated. This measurement was done by guiding 1545.7 nm of laser light from Agilent 8163A Lightwave Multimeter by Corning SMF28 fiber through a copper tube holder clamped on top of the diodes (see Figure 5.6). The current pulses were measured as function of time while the detector was at 0 V bias. Figure 6.1(a, b, c) show examples of the photocurrent dependence on detector area (Figure 6.1(a)), temperature (Figure 6.1(b)) and bias voltage (Figure 6.1(c)). Figure 6.1(b) shows that the dark current increases with temperature while the current under illumination decreases at the higher temperature. The increase in dark current is discussed in relation to Figure 5.9 and Figure 5.18. The photocurrent decreases due to the shortening of the minority carrier diffusion lengths and this is the reason why responsivity also decreases at high temperature (see Figure 6.4). Figure 6.1(c) shows a large increase of the dark current with bias as the surface leakage increases through the shunt paths. The larger currents under illumination are due to the optically generated current which increases as the bias is increased.

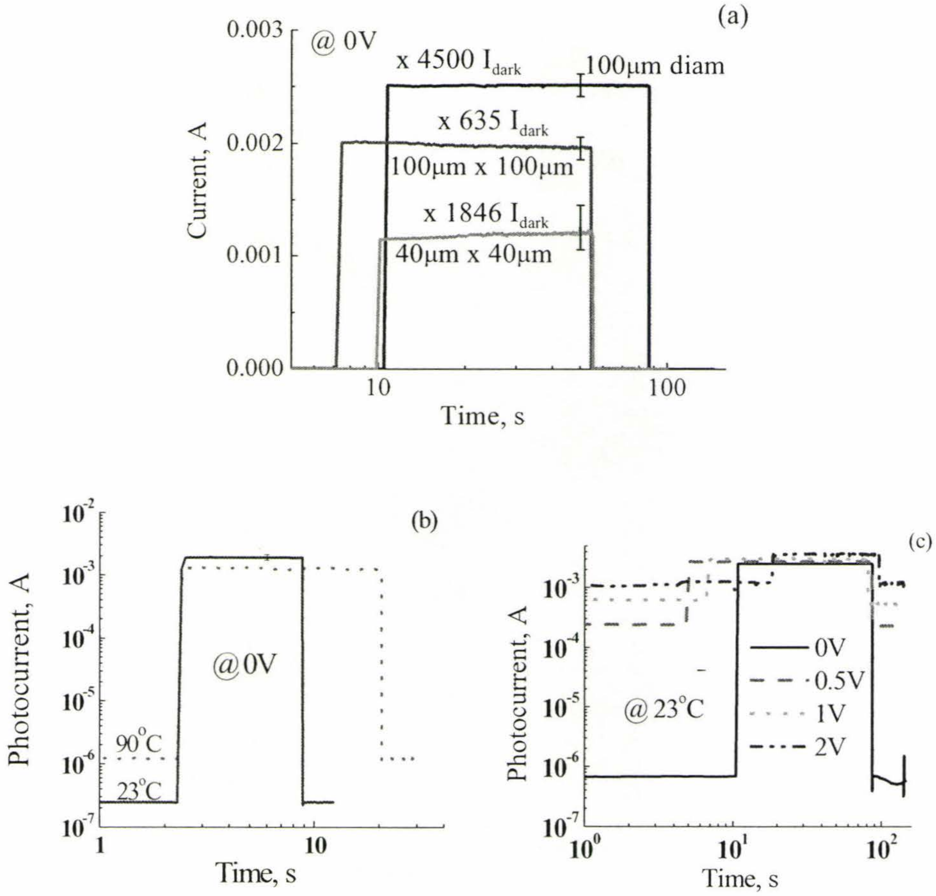

Figure 6.1: Photocurrent pulse under illumination as a function of (a) detector size, (b) temperature and (c) bias.

Responsivity

Responsivity (R) is a measure of the ability of the device to convert light into current at different wavelengths (λ) and is measured as the ratio of current output (I_{ph}) to the input optical power (P_{opt}) incident on the detector:

$$R = \frac{I_{\mathrm{ph}}}{P_{\mathrm{opt}}} \quad . \tag{6.1}$$

Quantum efficiency (η) and responsivity (R) are related by:

$$R = \eta \frac{q\lambda}{hc} \quad . \tag{6.2}$$

where q is electronic charge, h is Planck's constant and λ is wavelength of the incident light.

Sample #528 was designed for detection of light at wavelengths of 2.0 μm and beyond. The absorption coefficients for similar compositions are reported in [133]. Using these values the device layer thicknesses allowed detection of about 60% of the incident light of 2.0 μm and beyond. Responsivity was measured by using the experimental set-up shown in Figure 6.2. A broad spectral output 100 W xenon lamp source (Newport 6257) was used in conjunction with an Oriel 74100 motorized monochromator as the light source. The whole arrangement was set-up in a dark room. A reference detector (J23-18I-R01M-2.4 supplied by Judson Technology) is used to measure the power output in the wavelength range of interest.

Figure 6.3 gives the responsivity (dashed line) provided by the manufacturer along with the measured power density as a function of wavelength (solid line) over the active area of the 1.0 mm circular reference diode. The observed dip in the measured power density around 1900 nm is due to absorption by the water lines present in the ambient. The reference diode was then replaced by a DUT (sample #528 – a Si_3N_4 passivated n-i-p device) and the photocurrent was measured which was in turn converted to responsivity by eq.(6.1). Sample #528 had an indium fraction of 18.2% which corresponded to a bandgap of 0.558 eV. Hence, the cut-off for these detectors is expected to be around 2220 nm at room temperature. The responsivity curves in Figure 6.4 show a room temperature cut-off wavelength at 2270±5 nm. At 50° C the cut-off shifts toward a higher wavelength since the bandgap shrinks from its room temperature value. Also, between wavelengths of 1400 – 2100 nm, the average responsivity at 50° C (0.454) is lower than that of room temperature (0.483) due to the shortening of the diffusion lengths [133].

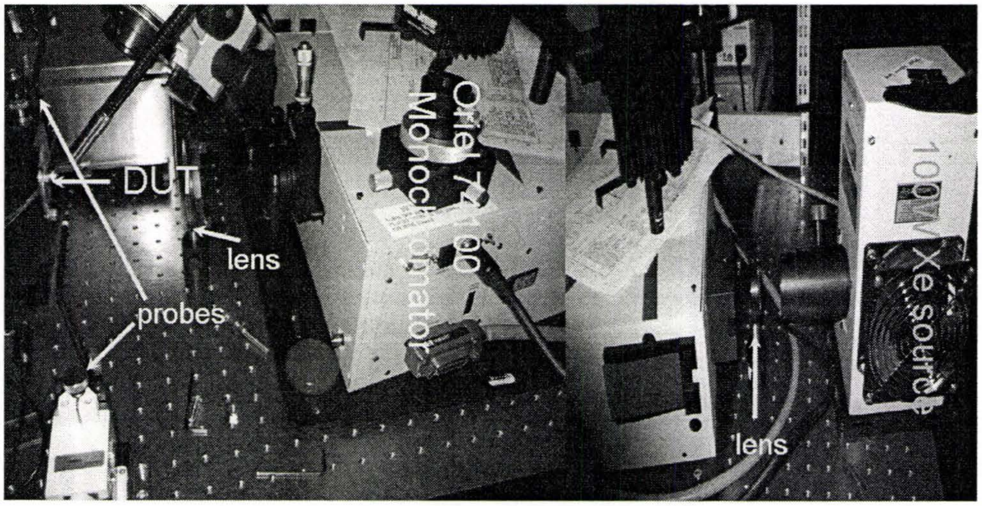

Figure 6.2: Set-up for responsivity measurements.

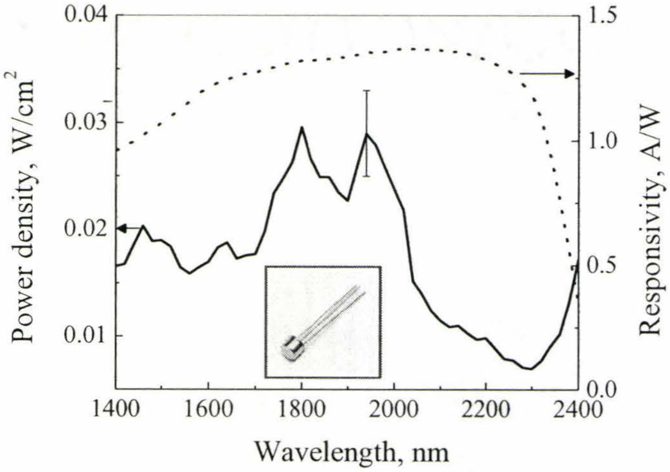

Figure 6.3: Responsivity curve of the reference as supplied by the supplier and the power density measured by the 1.0 mm circular detector. Inset shows a picture of the diode.

Detectivity

Detectivity (D*) is defined as [140]:

$$D^* = R\sqrt{\frac{R_o A}{4kT}} . \tag{6.3}$$

where, R is the responsivity (eq.(6.2)) and R_oA is the zero-bias-resistance-area product (eq.(5.1)). Detectivity for the same diodes is calculated using eq.(6.3) as a function of wavelength and is shown in Figure 6.5. The R_oA used in the calculation was 0.177 Ωcm^2 and 0.113 Ωcm^2 measured for this DUT at 23° C and 50° C, respectively. At higher temperature, the detectivity decreased because of the decrease in responsivity, the increase in the slope of the J-V curve (inverse of R_oA) for the DUT and due to the $1/\sqrt{T}$ - dependence of the detectivity seen in the above equation.

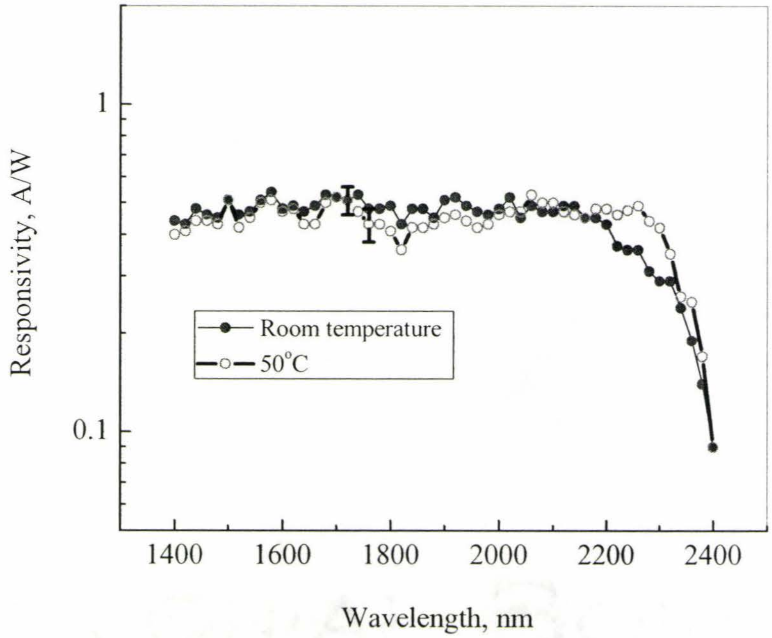

Figure 6.4: Measured responsivity curves for a 100 μm x 100 μm diode from sample #528. Both room temperature and 50°C responsivity are shown.

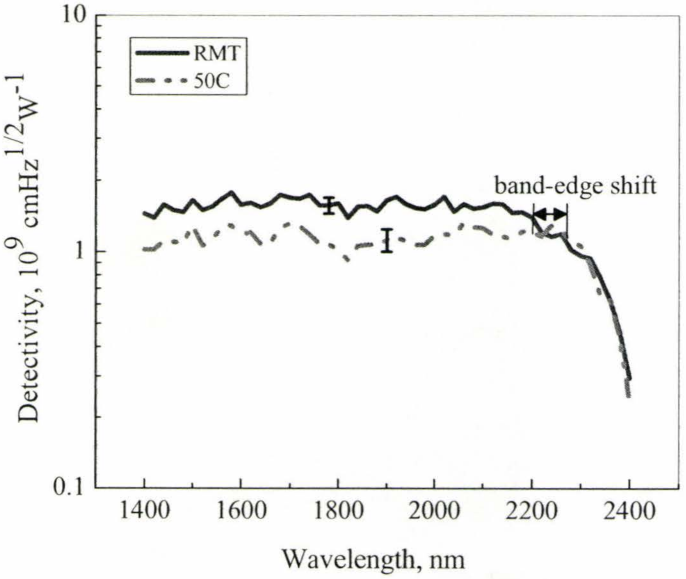

Figure 6.5: Detectivity extracted from Figure 6.4.

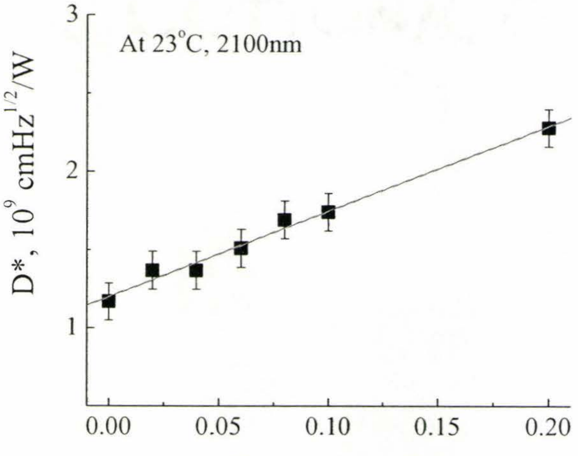

Figure 6.6: Detectivity as a function of reverse bias.

Variation in detectivity, at a wavelength of 2100 nm, with bias voltage was also investigated at room temperature and is shown in Figure 6.6. With increasing bias, carriers get multiplied in the applied field and are swept across the diodes. This also increases the responsivity.

The responsivity measurements for the DUTs require that the incident optical power is determined accurately. Hence, the accuracies of the data presented in this section depend on the accuracy of the power measured by the reference detector. The calculation of quantum efficiency and detectivity all in turn depend on the values of responsivity (see equations (6.1) and (6.3)). The observed variation in the measured power density is about 15% around the average power density. This variation is caused by subtle changes in the optical path, e.g. temperature and humidity changes, losses and reflections in the lenses etc. However, the accuracy of the responsivity of the reference detector was not provided by the supplier. The observed variation in the measured power density causes an estimated error of ±0.05 in responsivity values, ±3% in values of quantum efficiency and $\pm0.1\times10^9$ in detectivity.

Comparison

Responsivity, detectivity and quantum efficiencies for the present photodiodes are compared in Table 6.1 to other InGaSb photodiodes grown in various ways reported in the literature. Ref [133] used a custom-made compositionally-graded substrate and the junction was formed by Zn-diffusion while in [142] the detector structure was grown on GaSb without any composition-grading using the MOCVD technique. Reference [146] reports a similar MBE grown InGaSb detector on a "high-quality graded InAlSb digital alloy buffer layer on GaSb substrates," but has a detectivity more than two-orders of magnitude lower than that of the present diodes at 100 K. In Figure 6.7, the room temperature detectivity of the present diodes are compared to those of InGaAs, InAs and PbSe at similar wavelengths [141]. Although the present diodes are superior to uncooled InAs and PbSe detectors, $In_{0.97}Ga_{0.03}As$ on InAs has better detectivity. This is due to the better photodetector design implemented in that reference that resulted in much lower surface leakage current. It is estimated that for the present diodes, if the perimeter leakage component were minimized, the detectivity would have a three-fold increase from the reported values. With a better and optimized processing technique, the present diodes have the potential to compete with the best InGaAs detectors that were reported in [141]. If this becomes a reality, the present diodes can then rival those from the MCTs operating at cryogenic temperatures.

Table 6.1: Comparison of responsivity, quantum efficiency and detectivity.

		Responsivity, A/W	Detectivity, cmHz$^{1/2}$/W	Quantum efficiency, η	Comments
Present diodes	1550 nm	0.47±0.05	1.6(±0.1) ×10^{9}	38±3%	100 μm square mesa P-I-N $In_{0.18}Ga_{0.82}Sb$ on metamorphic layers,
	2000 nm	0.44±0.05	1.5(±0.1) ×10^{9}	28±3%	
Ref [133]	1550 nm	0.59	4.1x10^{10}	_	150 μm diameter mesa PN $In_{0.17}Ga_{0.83}Sb$ on custom substrate
	2000 nm	0.56	3.9x10^{10}	35.5%	
Ref [142]	1550 nm	0.4	_	35%	180 μm diameter disk mesa $N^{+}P$-$In_{0.4}Ga_{0.6}Sb$ on GaSb
	2000 nm	0.6	_	40%	

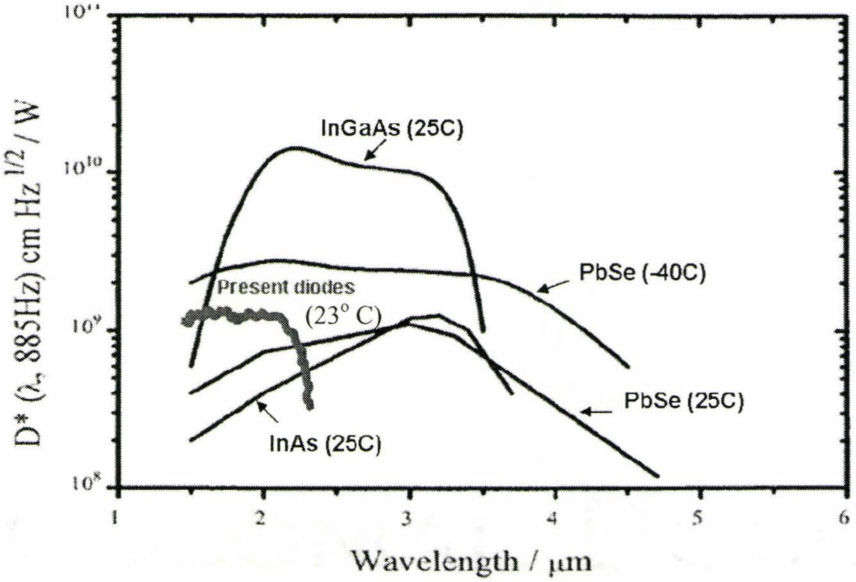

Figure 6.7: Detectivity comparison of the present diodes with some other commercially available materials for mid-IR diodes, only for the III-V semiconductors [141].

6.2 Ionization in Antimony Materials

Materials containing antimony are important for long wavelength (2 – 5 μm) applications. Low-noise, high-sensitivity, high-speed avalanche photodetectors require unequal electron (α) and hole (β) ionization coefficients ($\alpha \neq \beta$) [147]–[150]. But in some important widely-used III-V semiconducting materials (GaAs, InP, InGaAs), these coefficients are almost equal ($\alpha = \beta$) and hence, their ratio ($k = \beta/\alpha$) being nearly unity. However, it has been shown in [150],[152],[154], that III-V alloys based on GaSb and InAs possess highly asymmetric ionization ($k \neq 1$). These ionization properties are sensitive to the device structure, geometry, fabrication and the way they are extracted. Hence, the results exhibit a wide range of values.

Experimental determination for ionization coefficients are reported for GaSb, AlGaSb and InGaAsSb [150]. For InGaAsSb, it has been reported that $\beta > \alpha$. There has been quite a bit of interest, both theoretical and experimental, on ionization properties of AlGaSb. Hildebrand et al.[157] first reported the ionization asymmetry ($\beta >> \alpha$) in AlGaSb and showed that this phenomenon is composition dependent, and the name "bandgap resonance effect" was proposed. Figure 6.8 shows the results of Hildebrand et al.: The figure (a) shows that at a certain composition of AlGaSb when $\Delta_{so} = E_g$, where Δ_{so} is the split-off band energy, the ratio k becomes very high and hence the "resonance"; the (b) figure shows the variation of α and β with electric field. This was followed by similar claims and counter-claims by other groups of researchers. Later, one theoretical work [156] showed that this "resonance effect" is also field-dependent[156]. For high fields, there is no "resonance" effect and $\beta = \alpha$. But for low fields, the "resonance" can be observed. In the case of GaSb, theoretical arguments for a symmetric ionization ($k = 1$) was put forward in [154]-[155], at least for high electric field ($q\lambda F > E_r$) in [156], where λ is mean free path and E_r is the phonon energy. Measurements showing asymmetric ionization ($k \neq 1$) have been reported in [153],[157]-[158]. Hildebrand et al.[157] reports that for GaSb at room temperature $k < 1$ (Figure 6.8 (b)), whereas Zhingarev et al. [158] reports that $k > 1$. The case for $k > 1$ was argued, because the band structure of GaSb allows Δ_{so} (split-off band) to be approximately equal to E_g (bandgap). This bandgap "resonance" effect is then thought to give rise to hole ionization from the split-off band [150],[157]. The condition, $k > 1$ was theoretically argued and experimentally verified for InAs and alloys of AlGaSb [150],[153],[158].

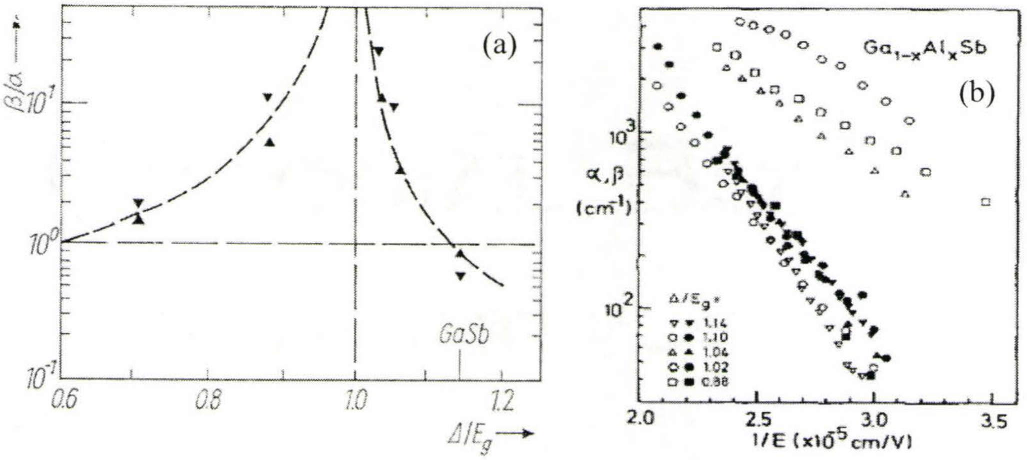

Figure 6.8: (a) The "bandgap resonance effect" and (b) electron and hole ionization coefficients for AlGaSb and [157]. Hollow and filled symbols correspond to holes and electrons, respectively.

Hole ionization coefficients have previously been determined for $In_xGa_{1-x}Sb$ with x = 0, 0.06, 0.12 and 0.18 at 77 K [153]; however, the values for α were not given. Figure 6.9 shows the results from reference [153]: the gain curves and the hole ionization data for various compositions measured at 77K. The authors argued that, like GaSb, InGaSb should also have a preferential hole initiated ionization. Hence α was not reported. The present work shows the opposite trend, that is, α > β for InGaSb in agreement with that in [157].

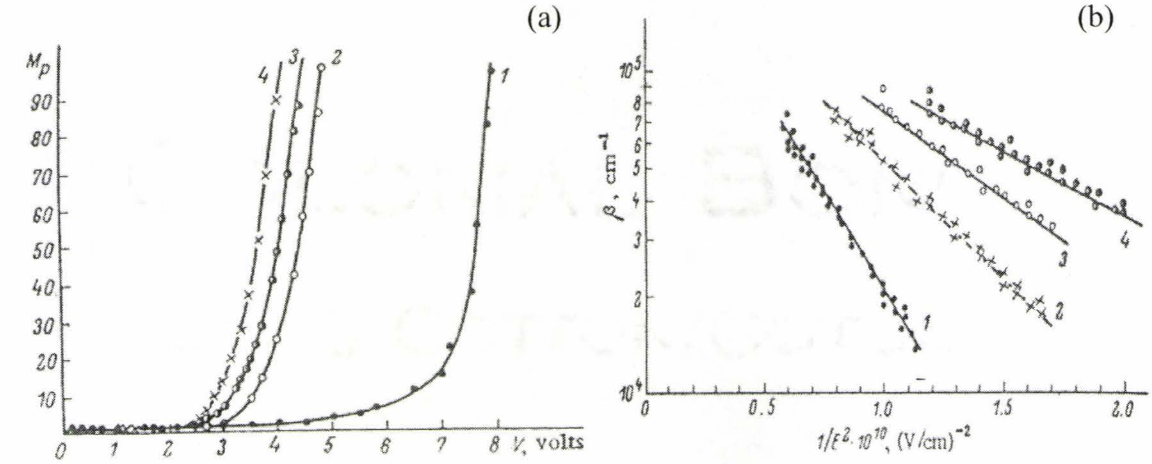

Figure 6.9: (a) Gain curves and (b) hole ionization coefficients in $In_xGa_{1-x}Sb$ at 77K for 1) x = 0, 2) x = 0.06, 3) x = 0.12, 4) x = 0.18 reproduced from [153].

6.3 Extraction of Ionization Coefficients

The standard procedure for extracting ionization coefficients [147] involves opening a back window by etching through the substrate. Together with the front window, this allows both electron and hole ionization to be measured in one device. Back window etching was not possible for the current devices due to the presence of strain and the highly dislocated buffer layers. Hence, complementary n-i-p and p-i-n structures were fabricated. The thickness of the top layers was chosen so that they absorbed ~70% of the incident light at 1545 nm [133].

Ionization Extraction

Ionization coefficients were extracted from samples #439, #510 and #528. Samples #439 and #510 had 10% indium composition, whereas sample #528 had 18% indium, see Table 5.1 for details. Hole ionization was dominant in samples #439 and #528 (n-i-p) and electron ionization was dominant in #510 (p-i-n) because of the diode structure. Photocurrents were extracted from diodes of 100 μm × 100 μm square geometry. The experimental set-up used in these measurements was that of Figure 5.6. Optical illumination was provided on the top open window of the diodes using a ~6.0 mW laser operating at 1545.7 nm. The normalized gain is defined as the ratio of the photocurrent (I_{ph}) to the unmultiplied photocurrent at 0 V ($I_{\text{ph,0V}}$):

$$M = \frac{I_{\text{ph}}(V)}{I_{\text{ph,0V}}} \tag{6.4}$$

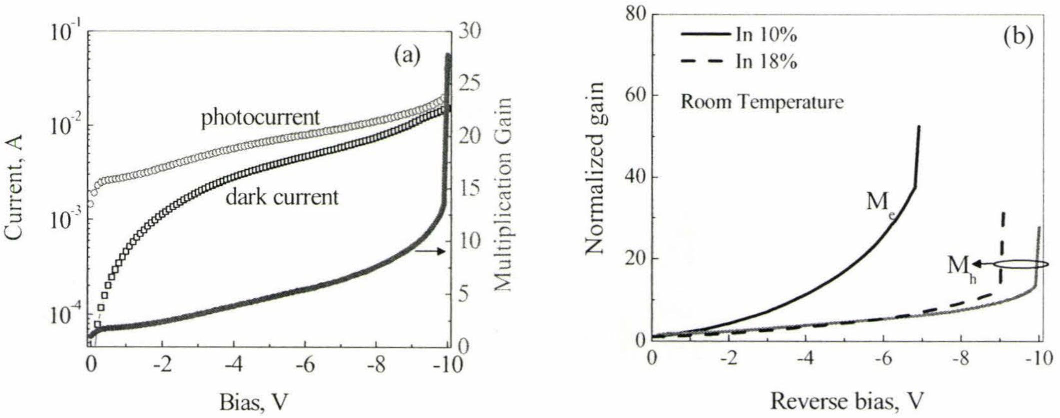

Figure 6.10: (a) Photocurrent, dark current and normalized gain for #439. (b)Gain for electron (#510) and hole (#439 and #528) for two compositions.

Figure 6.10 (a) shows an example of room temperature photocurrent, dark current and the multiplication gain as a function of bias voltage as defined in the above equation. Figure 6.10 (b) shows the normalized gains M_e (for electrons) and M_h (for holes) with bias extracted at room temperature from the p-i-n and n-i-p diodes, respectively. This figure also shows the composition dependence of the gain which is similar to those seen in [153] and discussed in the previous section (see Figure 6.9 (a)). The continuous values of the gain, before the vertical rise, were used to extract ionization coefficients shown later.

The gain curves were in turn used to calculate the ionization coefficients [147]:

$$\beta(F) = F\frac{1}{M_e(V)M_h(V)}\frac{dM_h}{dV} \tag{6.5}$$

The electric field is given by F, and for hole ionization, electrons are assumed not to be ionizing ($M_e = 1$). Replacing β for α and M_h for M_e in eq.(6.5) gives the electron ionization coefficient. The field and depletion width variation with reverse voltage is shown in Figure 6.11 and calculated using the values mentioned in Appendix 1 and assuming an abrupt junction. The ionization curves for electrons and holes, at both temperatures are shown in Figure 6.12 for $In_{0.10}Ga_{0.90}Sb$. The present data show that electron ionization is higher than hole ionization for both temperatures; i.e. $k = \beta/\alpha < 1$ and tends to support the earlier claim by Hildebrand et al.[157]. The addition of 10% indium does not perturb the band-structure significantly and hence $In_{0.10}Ga_{0.90}Sb$ should be similar to GaSb. The values of the ionization threshold energies for electrons (E_{ie}) and holes (E_{ih} – from the heavy-hole band and E_{so} – from split-off band) are calculated as suggested in references [153] and [157], noting that for $In_{0.10}Ga_{0.90}Sb$: Δ_{so} (0.756 eV) > E_g (0.63 eV) at room temperature:

$$E_{\mathrm{i,e}} = \frac{2m_e + m_h}{m_e + m_h}E_g \tag{6.6}$$

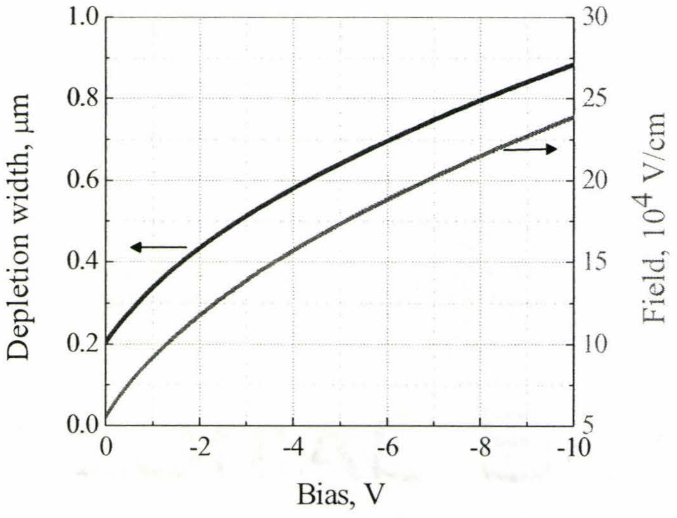

Figure 6.11: Depletion layer width and field intensity variation with reverse bias.

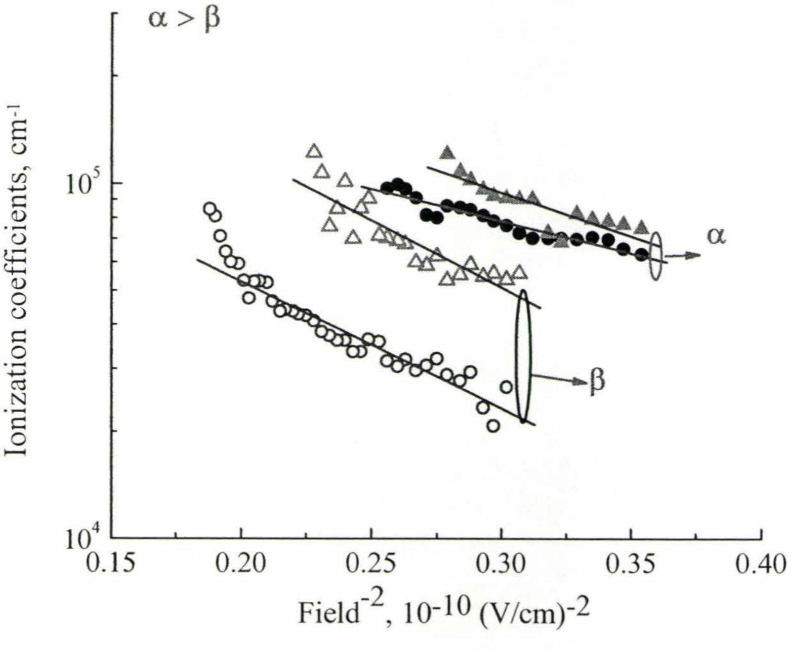

Figure 6.12: Electron and hole ionization coefficients for $In_{0.10}Ga_{0.90}Sb$ both at room temperature (circles) and at 90° C (triangles). Filled and hollow symbols are for electrons and holes respectively. The fitting lines, according to eq.(6.10), are also shown.

$$E_{\mathrm{i,h}} = \frac{2m_h + m_e}{m_h + m_e} E_g \tag{6.7}$$

$$E_{\mathrm{i,so}} = \Delta_{\mathrm{so}} \tag{6.8}$$

The threshold energies are calculated according to the above relations and are shown in Table 6.2 along with bandgap energies and the effective masses for room temperature and 90° C and for two compositions. The phonon energies are calculated from longitudinal optical phonon wavenumbers. These values are calculated using Appendix 1 and references [2], [162]. A comparison of the values of the respective threshold energies from Table 6.2 shows that electron ionization threshold energy is about 100 meV smaller than that for holes from split-off band, at both temperatures. Hence, it is expected that electron ionization would dominate in $\mathrm{In_{0.10}Ga_{0.90}Sb}$.

Figure 6.13 shows the measured hole ionization versus F^{-2} dependence on composition and temperature. Calculations of band-structural properties for $\mathrm{In_{0.18}Ga_{0.82}Sb}$ (E_g = 0.558 eV) are shown in Table 6.2 using the values in Appendix 1. The fitting parameters and the mean free paths are shown in Table 6.3. Since for the 18%-composition the bandgap is lower, this results in a lower threshold, which in turn causes the hole ionization to increase. This fact is also shown in the gain curves in Figure 6.10. According to Shockley [159], at high field energies, the dominant scattering mechanism for carriers arises from optical phonons. The mean free path for each carrier is then determined by the phonon energy E_r. Hence, the phonon energy E_r is an important parameter in ionization calculations. The value of longitudinal optical phonon energy (E_r = 28.4 meV) was obtained by linearly interpolating for those of GaSb and InSb.

The mean free path is calculated from [153]:

$$\lambda^2 = \frac{E_i E_r}{q^2 E_o^2} \tag{6.9}$$

here, E_o is a fitting parameter obtained by fitting the ionization data to the following relation (eq.(6.10)) and is tabulated in Table 6.3 for electrons and holes at both temperatures.

Table 6.2: Band structure properties for InGaSb [2], [143], [162].

	296 K	**363 K**	Indium fraction
Bandgap E_g, eV	0.63	0.611	10%
	0.558	0.542	18%
Split-off band Δ_{so}, eV	0.756		10%
	0.754		18%
Threshold energies			
Electron, $E_{i,e}$	0.682	0.661	10%
	0.601	0.584	18%
Holes, $E_{i,h}$	1.21	1.17	10%
	1.073	1.04	18%
Split-off holes, E_{so}	0.756		10%
	0.754		18%
Phonon energy E_r, meV	28.4		10%
	28.1		18%

Fitting and Temperature Dependence

A linear fit (correlation coefficient 0.94±0.02) of the following form to the values of ionization coefficients are also plotted in Figure 6.12:

$$(\alpha,\beta) = (\alpha_o,\beta_o)\exp\left[-\left(\frac{E_o}{E}\right)^m\right] \tag{6.10}$$

The value of m can be 1 or 2 depending on the electric field [157]. Values of α_o, β_o and E_o are deduced from a fit with $m = 2$, since our measurements are in the high field regime ($q\lambda F > E_r$).

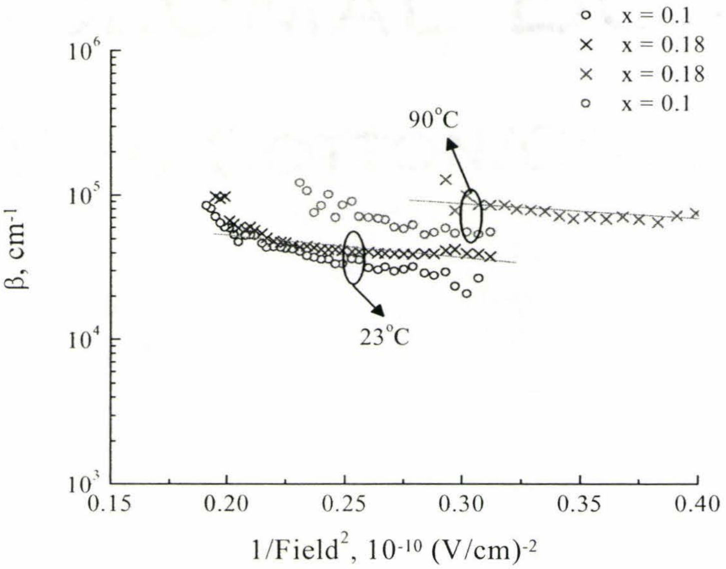

Figure 6.13: Composition and temperature dependence of hole ionization coefficient extracted from samples #439 ($x = 0.10$) and #528 ($x = 0.18$).

The fitting parameters extracted from the ionization data are listed in Table 6.3 for both composition and temperature. The accuracy in the fitting parameter values and the calculated mean free paths arise from the accuracy of the correlation factors of fitting. The resulting error limits are listed in Table 6.3. Electron and hole mean free paths are calculated using eq.(6.9) and Table 6.2. This allows an easy comparison between those values reported in [153] at 77K, also shown in Table 6.3, for the same material with similar compositions. However, it is to be noted that in [153], the threshold energy was assumed to be 0.8 eV for all cases. In Table 6.3, the tabulated mean free paths were calculated using a room temperature hole threshold energy of 0.756 eV in eq.(6.8). The bandgap (and hence the ionization threshold E_i) shrinks by about 3% due to the 67° C increase in temperature. As a result, the ionization coefficients increase with the increase of temperature. The λ_h calculated at 90° C is lower than at room temperature and this can be explained by the ~ 3% decrease in E_g. Electron transport is complicated in GaSb and its related materials due to the small energy difference between the L-band to the Γ-band minima. At higher temperatures, there are more electrons in the L-band than those in Γ-band (see Section 2.4). This explains the relatively small increase in α at 90° C.

Table 6.3: Values of α_o, β_o, E_o and mean free paths extracted from the ionization data of Figure 6.12 for $x = 0.11$ and from Figure 6.13 for $x = 0.19$. Data for LPE grown $In_{0.12}Ga_{0.88}Sb$ at 77 K given in ref [153] are shown for comparison.

		363 K	296 K	77 K [153]	% In
Electron	α_o, $(\pm0.04)\times10^5$ (cm^{-1})	5.17	2.73	_	10%
Hole	β_o, $(\pm0.04)\times10^5$ (cm^{-1})	6.97	2.75	2.8	10%
		1.79	1.1	2.6	18%
Electron	E_{o_α}, $(\pm0.03)\times10^5$ (V/cm)	1.57	1.34	_	10%
Hole	E_{o_β}, $(\pm0.03)\times10^5$ (V/cm)	1.95	1.89	1.09	10%
		1.02	0.91	1.0	18%
Electron	λ_e, (Å)	87±2	104±2	_	10%
Hole	λ_h, (Å)	75±1	78±2	150	10%
		143±5	160±5	160	18%

The temperature dependence of the ionization coefficients are very important for designing practical receiver systems. Receivers may be employed in diverse environments requiring very low temperature operation. In such cases, it is important to be able to predict the temperature dependence of the ionization properties, which in turn will dictate the receiver performance. Okuto and Crowell [159] proposed an analytical formula to numerically calculate α and β at various temperatures. This formula was based on an "empirical one-point fitting" of the Baraff curves for ionization, such that once a single value of α is measured at some electric field and temperature, one can estimate α at any temperature and electric field [159]. The following formula was proposed:

$$(\alpha,\beta)=\frac{qF}{E_i}\exp\left\{0.217\left(\frac{E_i}{E_r}\right)^{1.14}-\sqrt{\left[0.217\left(\frac{E_i}{E_r}\right)^{1.14}\right]^2+\left[\frac{E_i}{qF\lambda}\right]^2}\right\} \tag{6.11}$$

$$\frac{E_r}{E_{ro}}=\frac{\lambda}{\lambda_o}=\tanh\left(E_{ro}\Big/2kT\right) \tag{6.12}$$

Here, F is the electric field, E_i is the threshold energy, λ and λ_o is the mean free path and E_r and E_{ro} is the optical phonon energy at temperatures T° K and 0° K, respectively. By keeping E_{ro} = 28.4 meV as fixed, we fitted the experimental curves of Figure 6.12 by changing the value of λ for various cases such that eq.(6.12) is maintained all the time. This ensures that the values of λ_o vary only by ±2 Å.

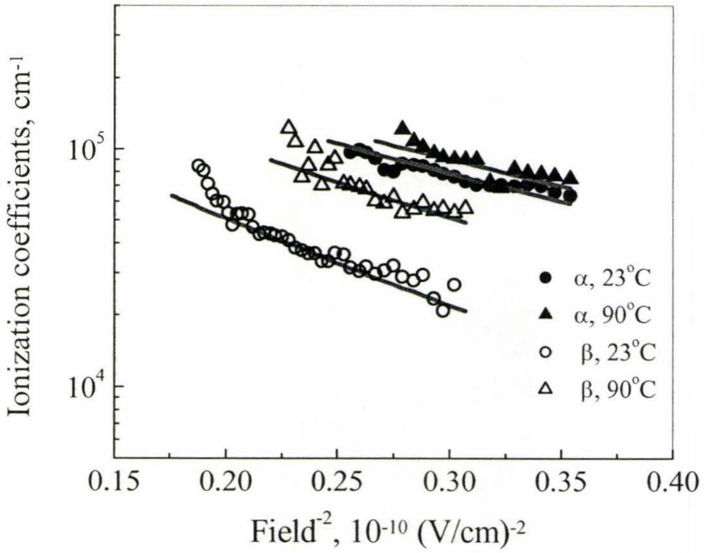

Figure 6.14: Fitting according to eq.(6.11). Electron and hole ionization coefficients for $In_{0.10}Ga_{0.9.0}Sb$ both at room temperature (circles) and at 90° C (triangles). Filled and hollow symbols are for electrons and holes respectively.

The results are shown in Figure 6.14 and the fitting parameters are quoted in Table 6.4. Table 6.4 shows that the zero temperature values for mean free paths (λ_o's) are reasonably constant, given the fact that for the well-studied InP alone and at room temperature, there is a considerable spread in the values of λ_o's from one research group to another (from as low as 37.5 Å and 41.7 Å for electrons and holes respectively to as high as 59.1 Å for both carriers; see [160] for a complete review). These parameters depend on the device structure and geometry of the DUT, the field distribution and the way the measurements were carried out. Consequently, these values differ from one research group to another. However, to obtain a good fit, it was necessary to use a high hole threshold energy for room temperature which is attributed to holes from the heavy hole band (eq.(6.7)). A similar high threshold was used for AlGaSb to explain its ionization behavior [161]. This cannot be explained from fitting procedures only. Band-structure calculations by a full-band Monte-Carlo simulation procedure that takes into account phonon scattering, threshold energy variation and the occupancy of the energy bands etc. are needed for a complete understanding.

The effective value of $k = \beta/\alpha$ can be determined from the following relation of excess noise and multiplication [147],[150]:

$$F = M\left\{1 - \left[\left(1 - k_{\mathrm{eff}}\right)\left(\frac{M-1}{M}\right)^2\right]\right\} \tag{6.13}$$

The excess noise is the additional noise created from the multiplication process. For typical receiver systems applications, a detector with lowest possible excess noise is preferable. Figure 6.15 shows the calculated excess noise figures against multiplicative gain for various values of k calculated from eq.(6.13). The values for excess noise for the present diodes (x = 0.10) were calculated using eq.(6.13) and the ratio $k = \beta/\alpha$ was extracted from Figure 6.12. Figure 6.15 shows the calculated and the measured results. This shows that $k_{\mathrm{eff}} = 0.2$ for the room temperature and its value increases to 0.5 for the higher temperature. This result shows that at room temperature, these $In_{0.10}Ga_{0.90}Sb$

diodes have an excess noise less than ~4 for gains up to 10. So avalanche detectors using this particular material will result in a low-noise, high-sensitivity receivers. However, the excess noise increases at high temperature and there is a considerable spread in the data, indicating more noisy operation.

Table 6.4: Fitting parameters for temperature fitting in eq.(6.11).

		363 K	**296 K**
		$In_{0.10}Ga_{0.90}Sb$	
Electron	λ_e, (Å)	53±1	55±1
	λ_o, (Å)	124±2	110±2
	$E_{i,e}$, (eV)	0.661	0.682
Hole		$In_{0.10}Ga_{0.90}Sb$	
	λ_h, (Å)	47±1	56±1
	λ_o, (Å)	110±2	112±2
	$E_{i,h}$, (eV)	0.756	1.2
		$In_{0.18}Ga_{0.82}Sb$	
	λ_h, (Å)	58±1	60±1
	λ_o, (Å)	137±2	120±2
	$E_{i,h}$, (eV)	0.754	1.2
Phonon energy	E_r, (eV)	0.0121	0.0142

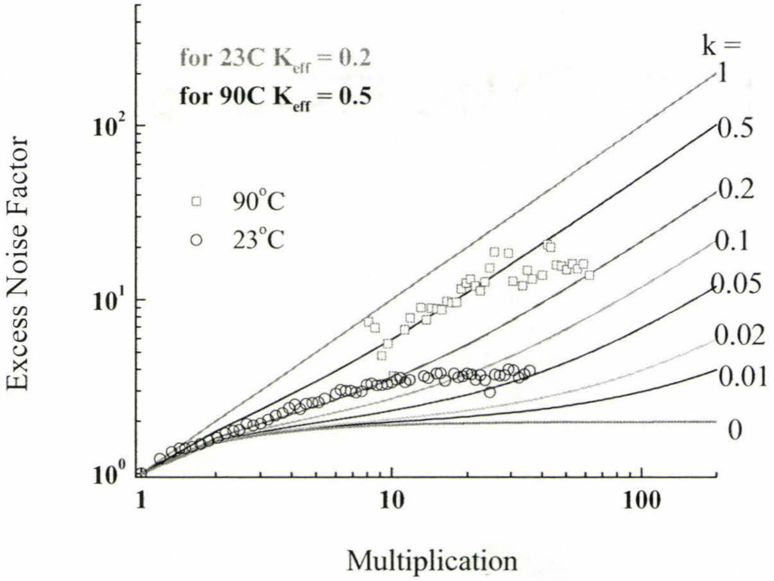

Figure 6.15: Extraction of K_{eff} and its temperature dependence.

It is very difficult to estimate errors for the ionization coefficients. These coefficients (see eq.(6.5)) are sensitive to the gain profiles of the respective test-structures. Particularly, the slopes of gain-voltage curves at high electric fields play a key role. As a numerical example, for a small variation in gain (M) by ±2.0, the ionization coefficient changes by $\pm 1.2\times 10^4$ cm^{-1}. This, however, does not account for the variation in slopes in the electric field region of interest. The gain profile depends on the geometry, doping levels, presence of defects and dislocations, electric field profile in the test-structures used and the way the measurements were carried out. As a result, there is a considerable spread in the ionization coefficients values measured even for well-studied materials, e.g. InP, as mentioned before.

6.4 Summary

The optoelectronic characterizations carried out on the diodes, discussed in the previous chapter, are described in this chapter. Responsivity measurements were successfully carried out to show that the present DUTs have a cut-off wavelength of 2270 nm. This means that the metamorphic growth technology can indeed be applied to the materials of 6.1 Å family and fabricate devices with reasonable performance for mid-infrared detection. Also, the bias and temperature dependence of detectivity were investigated. Electron and hole ionization coefficients were extracted from the test-structures and our findings suggest that electrons dominate the ionization in $In_{0.10}Ga_{0.90}Sb$, i.e. $\alpha > \beta$. The temperature fittings carried out to the measured ionization coefficients will help in extrapolating device properties at any other temperature.

Chapter 7 Conclusion and Future Recommendations

This chapter summarizes the key findings of this research and provides recommendations for possible future development of long wavelength GaSb-based photodetectors and sensing systems.

7.1 Conclusion

Metamorphic growth technology provides a convenient and inexpensive way to fabricate device layers containing semiconductor layers of required composition, for a specific device application whilst minimizing strain effects, using a metamorphic pseudo-substrate with a suitably adjusted lattice constant on a readily available binary substrate. This technology has been implemented on GaAs and InP substrates and optoelectronic integrated circuits containing photodetectors and amplifiers have been successfully fabricated. In the present research project, we have extended this growth technology for the antimony containing materials thereby allowing access to devices utilizing the 6.1 Å family of semiconductors. This allows the device designer to grow semiconducting layers suitable for devices operating in the mid-infrared wavelength range on commercially available substrates, e.g. InP or GaAs (see Section 1.3) allowing cost reductions per device, since these substrates are currently available in 4-inch or 6-inch diameter sizes.

A gas source molecular beam epitaxy machine was used in this research project. The required calibration of the various cells, i.e. group-III and –V cells, the flow rates of arsine and phosphine and the dopant cells (GaTe and Be) were calibrated. This study is summarized in Chapter 2. The results obtained from this chapter were then applied to the subsequent growths in Chapter 4 and Chapter 5.

It is important to know the etching characteristics of GaSb thoroughly before fabrication is attempted. Hence, we have studied the wet and reactive ion etching characteristics of GaSb in Chapter 3. Our findings show that reactive ion etching using a $CH_4/H_2/Ar$ mixture produces abrupt mesa side-walls and better surface morphology compared to that using wet chemical etching. A systematic study of the RIE process is reported through evaluating the etch rates, mesa sidewall verticality and surface morphology demonstrating how these parameters are affected by the experimental conditions: plasma microwave power and rf bias power levels, gas ratios, chamber pressure etc. It was determined that the RIE process also etched the SiO_2 mask, but at a slower rate, so this had to be calibrated and adjusted for in order to achieve the required mesa height. A final process was established that yielded mesas with good vertical sidewalls with an excellent surface morphology at the mesa base. The particular recipe (microwave power 150 W, rf power 100 W, chamber pressure 2 mTorr, and gas ratio $CH_4/H_2/Ar = 4:16:7.6$) that was used for the device fabrications, discussed in Section 5.2, resulted in good quality mesa and low-damage etched surfaces with reproducible etch rates. This study shows that the same gas mixture which are typically used for GaAs or InP based materials are also applicable to GaSb and InGaSb. However, etch rates are functions of chamber geometry and hence can be significantly different from machine to machine. Also, etch rate variations are subject to the equipment being used, the purity of the gases, pre-treatment of the samples etc.

We have successfully grown metamorphic layers of GaSb on InP and InGaSb on GaSb (Chapter 4) using MBE growth. The metamorphic pseudo-substrates were extensively characterized by x-ray diffraction analysis, cross-sectional and plan-view transmission electron microscopy etc. X-ray diffraction was used to determine the in-plane lattice constants of the metamorphic layers. Transmission electron microscopy was used to establish suitable growth conditions which resulted in a low density of dislocations threading through the metamorphic pseudo-substrate and to quantify their density. It was determined that a growth temperature greater than 500° C ensures that few dislocations thread through the top metamorphic layer, the misfit dislocation densities are reduced and the surface morphology improves. Also, it was found that the highest quality epitaxial layers could be grown on the GaSb substrates when the substrate was exposed, prior to growth, to a hydrogen plasma at a temperature around 540 to 550° C. This ensures a high quality interface between the first buffer layer grown on the substrate.

InGaSb photodiodes have been fabricated on top of InGaSb metamorphic pseudo-substrates (Chapter 5) grown by MBE on GaSb substrates. Photodiodes were produced with variable area-constant perimeter or constant area and variable perimeters allowing extraction of the area and perimeter component of the leakage current. It is shown that the dark current in small-area diodes is dominated by surface leakage. In order to reduce this surface leakage, we have investigated surface passivation using polyimide and silicon nitride. Our findings suggest that silicon nitride results in better surface passivation than polyimide. Theoretical modeling also confirms that the dark current in the present diodes was dominated by a surface shunt current component. This shows that processing parameters have a significant effect on the final current-voltage characteristics through the zero-bias-resistance-area-product of the diodes.

Optoelectronic measurement results (Chapter 6) show that the fabricated diodes with $In_{0.18}Ga_{0.82}Sb$ have a cut-off wavelength at 2270 nm. We also calculated the detectivity of these diodes and its temperature dependence by measuring responsivity at room temperature and at 50° C. The bias dependence of detectivity was also investigated. Finally, we have extracted the electron and hole ionization coefficients for $In_{0.10}Ga_{0.90}Sb$ homojunction diodes and hole ionization from $In_{0.18}Ga_{0.82}Sb$ diodes (Section 6.3). The temperature dependence was also investigated at two temperatures (23° C and 90° C). We have found that electron ionization dominates over hole ionization, i.e. ($\alpha > \beta$), at both temperatures for this material. The excess noise figures for these diodes suggest that at room temperature the noise figure is less than 4 for gains up to 10. Thus, InGaSb avalanche detectors can potentially be used as a low noise front-end component in an integrated optoelectronic receiver system.

7.2 Recommendations for Future Work

In this section, the future improvements and/or extensions based on the findings of the present research will be described. The present research laid the foundation for growth and fabrication of antimony-based materials in the facilities used. Following paragraphs will enumerate the ways and possible means to further the findings of this research.

Various process related parameters can be fine-tuned to improve the diode I-V curves by increasing the R_oA-product of the diodes. For example, the Ohmic contacts implemented in this project were not optimized for GaSb. In the literature, there are other metal combinations (e.g. Pd, W and Sn) used for this purpose, and further research has to be done to investigate their effects on the final R_oA-product. Besides, different polyimides with lower curing temperatures can be investigated that will successfully passivate the side-walls. At the same time, they will encapsulate the mesas and planarize the sample so that the metal lift-off process becomes smooth. Also, mesa capping by a wide-bandgap lattice-matched III-V material has been suggested [137] for better surface passivation. This procedure can be explored to effectively reduce the leakage currents by exploring MBE growths of the suitable materials. Wet chemical etching can be explored to find a better etching solution that yields high etch rate and at the same time results in low damage abrupt mesa sidewalls without any undercuts. The steps recommended will improve the detectivity of the diodes through increasing the R_oA-product of the diodes.

The present diodes have a cut-off up to 2270 nm. In order to extend the cut-off wavelength, other compositions of InGaSb with higher In-fraction can be explored with the present metamorphic growth technique. Further growth studies and materials characterizations are needed for the compositions greater than 30%-In. Particularly, the x-ray techniques used in this research were based on single (004)-scans in a time-saving fashion. However, this technique is limited to the ability of growing a cap layer that is fully strained. Compositions greater than 25%-In result in threading dislocations through the cap layer, making the present technique unreliable. Hence, compositions of InGaSb having more indium will require sophisticated x-ray techniques involving multiple scans in asymmetric planes (e.g. 224-scans) (see [66],[163]). However, there are other members of the 6.1 Å family that can be explored with the metamorphic growth technique for still longer wavelength applications.

The test-structures used in this research for ionization coefficients extraction were not optimized. It is better to have both the electrons and holes ionize in the same diode structure. This can be done by opening a backside window by etching through the substrate. This can be implemented by redesigning the present mask layout. Needless to say, it will be a challenging task to etch GaSb-substrate all the way to the p-i-n diode. This is because of the presence of threading dislocations in the M-substrate.

Avalanche photodetectors with optimized designs can be implemented, taking into account of the asymmetric ionization coefficients of InGaSb, or antimony based materials in general. This will result in high-gain, high-sensitivity and low-noise operation of the detectors. Furthermore, the present metamorphic growth technique can be used to extend the operational wavelength of these avalanche photodetectors to still longer wavelengths. Antimony materials are reported to have high mobility, and hence, suitable candidates for high speed electronic devices. As such, high electron mobility transistor (HEMT) structures incorporating GaSb-based materials can be thoroughly studied. Following the findings in ref[29] and other references in Section 1.3, where HEMT structures were metamorphically grown on GaAs substrates, these Sb-containing HEMT structures can also be grown on M-substrates without any degradation in device properties. Ultimately, avalanche photodetectors and HEMT structures can be combined in a single optoelectronic integrated circuit (OEIC) for low-noise, high-speed and high-sensitivity operation in low-light environment. It will be possible to fabricate this single module on 6-inch GaAs substrates with the help of the metamorphic growth technology. This will, then, serve as a low-cost solution to a complete sensing system for the mid-infrared.

Furthermore, other interesting device structures can be explored as well. For example, antimony containing materials are able to provide type-II or –III band alignments (see Figure 1.2), which opens up the possibility of achieving inter sub-band transitions. These type-II superlattice structures can be investigated for their possible inclusion in mid-IR laser or photodetector structures [3]. Antimony based materials can also be used in growing highly strained quantum dot systems, and thereby fabricate quantum dot photodetectors, which have reasonable detectivity at room temperature for long infrared wavelength applications [38],[164]. Hence, the fabrication of such interesting and exotic device structures can be investigated in future by furthering the technological experience achieved by the present thesis regarding the MBE growth and device fabrication.

For light sources in the mid-IR wavelengths, light emitting diodes or lasers can also be fabricated incorporating antimony ternaries or quaternaries [3]. Unlike intraband quantum cascade lasers, Sb-based type-II interband-cascade lasers use interband transitions for photon emission without involving fast phonon scattering, making it theoretically possible to achieve very low threshold current densities, at the same time reducing power consumption. Continuous wave operation of such a laser at 3.3 μm has recently been reported [165]. Light emitting diodes are also reported using antimony materials for emission in 2 – 5 μm range [47],[166]. Similar lasers or light emitting diodes can now be fabricated with improved performance with the technological advances made by the present research project.

References

[1] H. Kroemer, "The 6.1 Å family (InAs, GaSb, AlSb) and its heterostructures: A selective review," *Physica E*, **20**, p.196 (2004).

[2] P. S. Dutta, H. L. Bhat and V. Kumar, "The physics and technology of gallium antimonide: An emerging optoelectronic material," *Journal of Applied Physics*, **81**, p.5821 (1997).

[3] M. O. Manasreh (ed.), *Antimonide-related Strained-Layer Heterostructures*, Optoelectronic Properties of Semiconductors and Superlattices, Vol. 3, Gordon and Breach Science Publishers, Amsterdam, (1997).

[4] B. R. Bennett, R. Magno, J. B. Boos, W. Kruppa and M. G. Ancona, "Antimonide-based compound semiconductors for electronic devices: A review," *Solid-State Electronics*, **49**, 1875 (2005).

[5] T. Whitaker, *Compound Semiconductor*, January and September, (2004).

[6] J. R. Meyer, J. I. Malin, I. Vurgaftman, C. A. Hoffman, L. R. Ram-Mohan, "Antimonide-based quantum heterostructure devices," in *Antimonide-Related Strained -Layer Heterostructures*, M. O. Manasreh (ed.), p. 235, Gordon and Breach Science Publishers, Amsterdam, (1997).

[7] A. Rogalski, "Infrared detectors: status and trends," *Progress in Quantum Electronics*, **27**, p.59-210, (2003).

[8] J. Gowar, *Optical Communication Systems*, p.71-89, Prentice Hall, London, (1984).

[9] J. M. Senior, *Optical Fiber Communications: Principles and Practice*, 2nd Ed., p.84-153, Prentice Hall, U.K., (1992).

[10] G. P. Agrawal, *Fiber-Optic Communication Systems*, 3rd ed., Wiley Interscience, N.Y., (2002).

[11] I. D. Aggarwal, G. Lu, *Fluoride Glass Fiber Optics*, p. xi-xiv, Academic Press, (1991).

[12] James A. Harrington, *Infrared Fibers and their Applications*, p.5-7, SPIE Press, (2004).

[13] Ed. S. Campion, Release No. 01-57, Goddard Space Flight Center, Greenbelt, MD, June 4, (2001).

[14] N. P. Prasad, *Introduction to Biophotonics*, John Wiley & Sons Canada, Ltd., (2003).

[15] M. N. Abedin, T. F. Refaat, O. V. Sulima, S. Ismail and U.N. Singh, "Two-micron detector development using Sb-based material systems," *Proceedings of the Sixth Annual NASA Earth Science Technology Conference*, ESTC-2006, (2006). Available at : http://www.esto.nasa.gov/conferences/ESTC2006/ .

[16] S. D. Humphries, K. S. Repasky, P. Nachman, J. A. Shaw, J. L. Carlsten, L. H. Spangler, "Atmospheric carbon dioxide measurements using a tunable laser based system," *6th Annual Conference on Carbon Capture & Sequestration*, Pittsburgh, Pennsylvania, (2007).

[17] P. Norton, "Infrared sensors in spacecraft that monitor planet Earth," *Opto-Electron. Rev.*, **16**, p.105-117, (2008)

[18] W. E. Hoke, P. J. Lemonias, J. J. Mosca, P. S. Lyman, A. Torabi, P. F. Marsh, R. A. McTaggart, S. M. Lardizabal, K. Hetzler, "Molecular beam epitaxy growth and device performance of metamorphic high electron mobility transistor structures fabricated on GaAs substrates," *J. Vac. Sci. Technol. B*, **17**, p.1131-1135, (1999).

[19] W. E. Hoke, P. S. Lyman, C. S. Whelan, J. J. Mosca, A. Torabi, K. L. Chang, K. C. Hsieh, "Growth and characterization of metamorphic Inx(AlGa)1-xAs/InxGa1-xAs high electron mobility transistor material and devoces with x=0.3-0.4," *J. Vac. Sci. Technol. B*, **18**, p.1638-1641, (2000).

[20] D. Lubyshev, W. K. Liu, T. R. Stewart, A.B. Cornfeld, X. -M. Fang, X. Xu, P. Specht, C. Kisielowski, M. Naidenkova, M. S. Goorsky, C. Whelan, W. E. Hoke, P. F. Marsh, J. M. Millunchick, S. P. Svensson, "Strain relaxation and dislocation filtering in metamorophic high electron mobility transistor structures grown on GaAs substrates", *J. Vac. Sci. Technol. B*, **19**, p.1510-1514, (2001).

[21] J. -H. Jang, G. Cueva, W. E. Hoke, P. J. Lemonias, P. Fay, I. Adesida, "Metamorphic graded bandgap InGaAs-InGaAlAs-InAlAs double heterojunction P-i-I-N photodiodes," *J. Lightwave Technol.*, **20**, p.507-514, (2002).

[22] Y.M. Kim, M.J.W. Rodwell, A.C. Gossard, "Thermal characteristics of InP, InAlAs, and AlGaAsSb metamorphic buffer layers used in $In_{0.52}Al_{0.48}As/In_{0.53}Ga_{0.47}As$ Heterojunction Bipolar Transistors grown on GaAs substrates," *J. Electron. Mater.*, **31**, p.196-199, (2002).

[23] W. E. Hoke, T. D. Kennedy, A. Torabi, C. S. Whelan, P. F. Marsh, R. E. Leoni, S. M. Lardizabal, Y. Zhang, J. H. Jang, I. Adesida, C. Xu, K. C. Hsieh, "Properties of metamorphic materials and device structures on GaAs substrates," *J. Crys. Growth*, **251**, p.803-810, (2003).

[24] Y. Zhang, C. S. Whelan, R. Leoni III, P. F. Marsh, W. E. Hoke, J. B. Hunt, C. M. Laighton, T. E. Kazior, "40-Gbit/s OEIC on GaAs substrate through metamorphic buffer technology," *IEEE Electron. Dev. Lett.*, **24**, p.529-531, (200)3.

[25] Ch. Heyn, S. Mendach, S. Löhr, S. Beyer, S. Schnüll, W. Hansen, "Growth of shallow InAs HEMTs with metamorphic buffer," *J. Crys. Growth*, **251**, p.832-836, (2003).

[26] Y.-C. Xin, L. G. Vaughn, L. R. Dawson, A. Stintz, Y. Lin, L. F. Lester, and D. L. Huffaker, "InAs quantum-dot GaAs-based lasers grown on AlGaAsSb metamorphic buffers," *J. Appl. Phys.*, **94**, p.2133-3125, (2003).

[27] W.E. Hoke, T.D. Kennedy, A. Torabi, C.S. Whelan, P.F. Marsh, R.E. Leoni, S.M. Lardizabal, Y. Zhang, J.H. Jang, I. Adesida, C. Xu, K.C. Hsieh, "Properties of metamorphic materials and device structures on GaAs substrates," *J. Crys. Growth*, **251**, p.804-810, (2003).

[28] J. H. Jang, G. Cueva, R. Sankaralingam, P. Fay, W. E. Hoke, I. Adesida, "Wavelength dependent characteristics of high-speed metamorphic photodiodes," *IEEE Photon. Technol. Lett.*, **15**, p.281-283, (2003).

[29] W. E. Hoke,R. E. Leoni, C. S. Whelan, T. D. Kennedy, A. Torabi, P. F. Marsh, Y. Zhang, C. Xu, K. C. Hsieh, "Material properties and performance of metamorphic optoelectronic integrated circuits grown by molecular beam epitaxy on GaAs substrates," *J. Vac. Sci. Technol. B*, **22**, p.1554-1557, (2004).

[30] D. Lubyshev, J. M. Fastenau, X.-M. Fang, Y. Wu, C. Doss, A. Snyder, and W. K. Liu, M. S. M. Lamb, S. Bals, C. Song, "Comparison of As- and P-based metamorphic buffers for high performance InP heterojunction bipolar transistor and high electron mobility transistor applications," *J. Vac. Sci. Technol. B*, **22**, p.1565-1569, (2004).

[31] M. Noori, R. S. Sandhu, S. L. Hayashi, E. D. Meserole, V. Hardev, A. Cavus, M. Lange, C. Monier, R. Hsing, D. Sawdai, M. Wojtowicz, T. R. Block, A. Gutierrez-Aitken,, M. S. Goorsky, "Strain relaxation and surface roughness of $In_xAl_{1-x}As$ graded buffer layers grown on InP for 6.05Å applications," *J. Vac. Sci. Technol. B*, **22**, 5, p.2303-2308, (2004).

[32] A. Rogalski, K. Adamiec, J. Rutkowski, *Narrow-Gap Semiconductor Photodiodes*, SPIE Press, Washington, (2000).

[33] J. Piotrowski and A. Rogalski, "Uncooled long wavelength infrared photon detectors," *Infrared Physics & Technology*, **46**, p.115–131, (2004).

[34] B. F. Levine, "Quantum-well infrared photodetectors," *J. Appl. Phys.*, **74**, p.R1-R81, (1993).

[35] J. L. Pan, C. G. Fonstad Jr., "Theory, fabrication and characterization of quantum well infrared photodetectors," *Mater. Sci. Eng.*, **28**, p.65-147, (2000).

[36] A. Rogalski, "Assessment of HgCdTe photodiodes and quantum well infrared photoconductors for long wavelength focal plane arrays," *Infra. Phys. Technol.*, **40**, p.279-294, (1999).

[37] A. Rogalski, "$InAs_{1-x}Sb_x$ infrared detectors," *Prog. Quant. Electron.*, **13**, p.191-231, (1989).

[38] S. Krishna, A. D. Stiff-Roberts, J. D. Phillips, P. Bhattacharya and S. W. Kennerly, "Hot dot detectors," *IEEE Circuits and Devices Magazine*, p.14-24, January (2002).

[39] J. Phillips, ""Evaluation of the fundamental properties of quantum dot infrared detectors," *J. Appl. Phys.*, **91**, p.4590–4594, (2002).

[40] B. Kochman, A. D. Stiff-Roberts, S. Chakrabarti, J. D. Phillips, S. Krishna, J. Singh and P. Bhattacharya, "Absorption, carrier lifetime, and gain in InAs–GaAs quantum-dot infrared photodetectors," *IEEE J. Quant. Elec.*, **39**, p.459-467, (2003).

[41] V. Ryzhii, I. Khmyroval, M. Ryzhii, V. Mitin, "Comparison of dark current, responsivity and detectivity in different intersubband infrared photodetectors," *Semicond. Sci. Technol.*, **19**, p.8-16, (2004).

[42] S. Hoogland, G. Konstantatos and E. H. Sargent, "Paint-on optoelectronics," *Optics and Photonics News*, **17**, p.18-23, November (2006).

[43] A. Jahanzeb C. M. Travers, Z. Celik-Butler, D. P. Butler, S. G. Tan, "A semiconductor YBaCuO microbolometer for room temperature IR imaging," *IEEE Trans. Electron Devices*, **44**, p.1795-1801, (1997).

[44] S. P. Watkins, O. J. Pittsa, C. Dalea, X. G. Xu1, M. W. Dvorakb, N. Matineb and C. R. Bolognesia, "Heavily carbon-doped GaAsSb grown on InP for HBT applications," *J. Crys. Growth*, **221**, p.59-65, (2000).

[45] G. J. Brown, S. Houston and F. Szmulowicz, "Type-II InAs/GaSb superlattices for very long wavelength infrared detectors," *Physica E,* **20**, 471 (2004).

[46] F. Fuchs, U. Weimear, W. Pletschen, J. Schmitz, E. Ahlswede, M. Walther, J. Wagner, and P. Koidl, "High performance InAs/Ga1-xInxSb superlattice infrared photodiodes," *Appl. Phys. Lett.,* **71**, 3251 (1997).

[47] A. Krier, V. V. Sherstnev and H. H. Gao, "A novel LED module for the detection of H_2S at 3.8 μm," *J. Phys.* D , **33,** p.1656-61, (2000).

[48] M. J. Yang, W. J. Moore, B. R. Bennett and B. V. Shanabrook, "Growth and characterization of InAs/InGaSb/InAs/AlSb infrared laser structures," *Electronics Lett.*, **34**, No. 3, 5th February (1998).

[49] Chih-Hsiang Lin, Rui Q. Yang, S. J. Murry, S. S. Pei, Chi Yan, D. L. McDaniel Jr., and M. Falcon, "Room-temperature low-threshold type-II quantum-well lasers at 4.5 μm," *IEEE Photonics Technology Letters*, **9**, 12, p. 1573-75, (1997).

[50] M. A. Herman, W. Richter, H. Sitter, *Epitaxy: Physical Principles and Technical Implementation*, Springer, p.131-169, (2004).

[51] R. R. Lapierre, *M.Sc. Thesis*, Department of Engineering Physics, McMaster University, (1994).

[52] E. Hall, R. L. Naone, J. E. English, H. R. Blank, J. Champlain and H. Kroemer, "Operational experience with a valved antimony cracker source for use in molecular beam epitaxy," *J. Vac Sci. Technol. B*, **16**, p.2660-2664, (1998).

[53] Q. Xie, J. E. Van Nostrand, R. L. Jones, J. Sizelove and D. C. Look, "Electrical and optical properties of undoped GaSb grown by molecular beam epitaxy using cracked Sb_1 and Sb_2," *J. Crys. Growth*, **207**, p.255-265, (1999).

[54] P. D. Brewer, D. H. Chow and R. H. Miles, "Atomic antimony for molecular beam epitaxy of high quality III–V semiconductor alloys," *J. Vac. Sci. Technol. B*, **14**, p.2335-2338, (1996).

[55] G. J. Davies and D. Williams, "III-V MBE growth systems," in *The Technology and Physics of Molecular Beam Epitaxy*, E.H.C. Parker (ed.), p.15-46, Plenum Press, N.Y., (1985).

[56] C. Raisin, A. Rocher, G. Landa, R. Carles and L. Lassabatere, "GaSb/GaAs heteroepitaxy characterized as a stress-free system," *Appl. Surf. Sci.*, **50**, p.434-439, (1991).

[57] W. Qian, M. Skowronski and R. Kaspi, "Dislocation density reduction in GaSb films grown on GaAs substrates by molecular beam epitaxy," *J. Electrochem. Soc.*, **144**, p.1430-1434,(1997).

[58] D. K. Schroder, *Semiconductor Material and Device Characterization*, John Wiley and Sons, 3rd Ed., (2006).

[59] M. J. Deen, F. Pascal, "Electrical characterization of semiconductor materials and devices — a review," *J. Mater. Sci.*, **17**, p.549-575, (2006).

[60] M. Ilegems, "Properties of III-V Layers" in *The Technology and Physics of Molecular Beam Epitaxy*, E. H. C. Parker (ed.), Plenum Press, N.Y.p.83-142, (1985).

[61] W. E. Spicer, P.W. Chye, P. R. Skeath, C. Y. Su and I. Lindau, "New and unified model for Schottky barrier and III-V interface states formation," *J. Vac. Sci. Technol*, **16**, p.1422-1433, (1979).

[62] J. F. Chen and A.Y. Cho, "Tellurium doping study of GaSb grown by molecular beam epitaxy using SnTe," *J. Crys. Growth*, **111**, p.619-622, (1991).

[63] G. W. Turner, S. J. Eglash and A.J. Strauss, "Molecular-beam epitaxial growth of high-quality n-GaSb," *J. Vac. Sci. Technol. B*, **11**, p.864-867, (1993).

[64] S. Subbana, G. Tuttle and H. Kroemer, "N-type doping of gallium antimonide and aluminum antimonide grown by molecular beam epitaxy using lead telluride as a tellurium dopant source," *J. Electron. Mater.*, **17**, p.297-303, (1988).

[65] B. R. Bennett, R. Magno, N. Papanicolauo, "Controlled n-type doping of antimonides and arsenides," *J. Crys. Growth*, **251**, p.532-537, (2003).

[66] E. Selvig, *Ph.D. Thesis*, Department of Electronics and Telecommunications, Norwegian University of Science and Technology, (2004).

[67] D. Martin and C. Algora, "Temperature-dependent GaSb material parameters for reliable thermophotovoltaic cell modeling," *Semicond. Sci. Technol.*, **19**, p.1040-1052, (2004).

[68] A. Sagar, "Experimental investigation of conduction band of GaSb," *Phys. Rev.*, **117**, p.93-100, (1960).

[69] M. W. Heller and R. G. Hamerly, "Hole transport in gallium antimonide," *J. Appl. Phys.*, **57**, p.4626-4632, (1985).

[70] A. Mezerreg, C. Llinares and A. Montaner, "Optical determination of carrier concentration and mobility in p and n bulk GaSb by infrared reflectivity spectral analysis," *Phys. Stat. Sol. B*, **169**, p.121-130, (1992).

[71] V. W. L. Chin, "Electron mobility in GaSb," *Solid-State Electron.*, **38**, p.59-67, (1995).

[72] P.S. Dutta, V. Prasad and H. L. Bhat, "Carrier compensation and scattering mechanisms in p-GaSb," *J. Appl. Phys.*, **80**, p.2847-2853, (1996).

[73] M. Hakala, M. J. Puska and R. M. Nieminen, "Native defects and self-diffusion in GaSb," *J. Appl. Phys.*, **91**, p.4988-4994, (2002).

[74] M.A. Cotta, M.M.G. de Carvalho, M.A.A. Pudenzi, K.M.I. Landers, C.F. de Souza, R.B. Martins, R. Landers, O. Teschke, "Surface morphologies of Be-doped homoepitaxial InP films," *J. Crys. Growth*, **164**, p.409-414, (1996).

[75] J. G. Cederberg and R. M. Biefeld, "The growth of n-type GaSb by metal-organic chemical vapour deposition: effects of two-band conduction on carrier concentrations and donor activation," *Semicond. Sci. Technol.*, **19**, p.953–958, (2004).

[76] J. Singh, *Semiconductor Devices: An Introduction*, p.233,248, McGraw-Hill Inc., (1994).

[77] F. Paskal, F. Delannoy, J. Bougnot, L. Gouskov, G. Bougnot, P. Grosse, and J. Kaoukab, "Growth and characterization of undoped and n-type (Te) doped MOVPE grown gallium antimonide," *J. Electron. Mater.*, **19**, p.187-195, (1990).

[78] E. A. Fitzgerald, A.Y. Kim, M.T. Currie, T. A. Langdo, G. Taraschi and M. T. Bulsara, "Dislocation dynamics in relaxed graded composition semiconductors," *Mater. Sci. Eng. B,* **67**, p.53-61, (1999).

[79] R. Clawson, "Guide to references on III-V semiconductor chemical etching," *Materials Science and Engineering*, **31**, p.1-438, (2001).

[80] O. Dier, C. Lin, M. Grau and M.C. Amann, "Selective and non-selective wet-chemical etchants for GaSb-based materials," *Semicond. Sci. Technol.*, **19**, p.1250-53, (2004).

[81] G. C. DeSalvo, R. Kaspi and C.A. Bozada, "Citric acid etching of GaA$_{s1-x}$Sb$_x$, Al$_{0.5}$Ga$_{0.5}$Sb, and InAs for heterostructure device fabrication," *J. Electrochem. Soc.*, **141**, p.3526-31, (1994).

[82] J. P. Langer and P. S. Dutta, "Electron cyclotron resonance plasma etching of GaSb in $Cl_2/BCl_3/CH_4/Ar/H_2$ at room temperature," *J. Vac. Sci. Technol. B*, **21**, p.1511-12, (2003).

[83] R. Giehl, M. Gumbel, M. Kessler, N. Herhammer, G. Hoffmann, H. Fouckhardt, "Deep dry etching of GaAs and GaSb using Cl2/Ar plasma discharges," *J. Vac. Sci. Technol. B*, **21**, p.2393-97, (2003).

[84] S. S. Ou, "Reactive ion etching of GaSb and GaAlSb using SiCl4," *J. Vac. Sci. Technol. B*, **14**, p.3226-29, (1996).

[85] G. Morello, M. Quaglio, G. Meneghini, C. Papuzza and C. Kompocholis, "Reactive ion etching induced damage evaluation for optoelectronic device fabrication," *J. Vac. Sci. Technol. B*, **24**, p.756-761, (2006).

[86] J. R. Mileham, J. W. Lee, E. S. Lambers and S. J. Pearton, "Dry etching of GaSb and InSb in $CH_4/H_2/Ar$," *Semicond. Sci. Technol.*, **12**, p.338-344, (1997).

[87] A. Semu and P. Silverberg, "Methane-hydrogen III-V metal-organic reactive ion etching," *Semicond. Sci. Technol*, **6**, p.287-289, (1991).

[88] J. Werking, J. Schramm, C. Nguyen, E. L. Hu and H. Kroemer, "Methane/hydrogen-based reactive ion etching of InAs, InP, GaAs, and GaSb," *Appl. Phys. Lett.*, **58**, p.2003 (1991).

[89] J. W. Lee, C. R. Abernathy, S. J. Pearton, C. Constantine, R. J. Shul and W. S. Hobson, "Etching of Ga-based III-V semiconductors in inductively coupled Ar and CH_4/H_2-based plasma chemistries," *Plasma Sources Sci. Technol.*, **6**, p.499-507, (1997).

[90] H. Luo, J.A. Gupta, H. C. Liu, "1.55 μm GaNAsSb photodetector on GaAs," *Appl. Phys. Lett.*, **86**, p.211121 (2005).

[91] C. D. W. Wilkinson and M. Rahman, "Dry etching and sputtering," *Phil. Trans. R. Soc. Lond. A*, **362**, p.125-138 (2004).

[92] B. Chapman, *Glow Discharge Processes*, John Wiley and Sons, N.Y. (1980).

[93] Jes Asmussen, "Electron cyclotron resonance microwave discharges for etching and thin-film deposition," *J. Vac. Sci. Technol. A*, **7**, p.883-93, (1989).

[94] D. L. Melville, J. G. Simmons and D. A. Thompson, "Identification of volatile products in low pressure hydrocarbon electron cyclotron resonance reactive ion etching of InP and GaAs," *J. Vac. Sci. Technol. B,* **11**, p.2038-45, (1993).

[95] D. L. Melville, D. A. Thompson and J. G. Simmons, "Effects of Electron Cyclotron Resonance Power and Cavity Dimensions in Plasma Etching of III–V Compounds," *J. Electrochem. Soc.*, **142**, p.2762-69, (1995).

[96] S. J. Pearton, T. A. Keel, A. Katz, and F. Ren, "Optical emission spectroscopy of electron cyclotron resonance discharges for_III-V semiconductor processing," *Semicond. Sci. Technol.*, **8**, p.1889-96, (1993).

[97] J. Kaindl, S. Sotier and G. Franz, "Dry Etching of III/V-Semiconductors: Fine Tuning of Pattern Transfer and Process Control," *J. Electrochem. Soc.*, **142**, p.2418-24, (1995).

[98] S. J. Pearton, J. W. Lee, E. S. Lambers, C. R. Abernathy, F. Ren, W. S. Hobson and R. J. Shul, "Comparison of Dry Etching Techniques for III-V Semiconductors in $CH_4/H_2/Ar$ Plasmas," *J. Electrochem. Soc.*, **143**, p.752-58, (1996).

[99] F. M. Mohammedy, Z. L. Peng, D. A. Thompson and M. J. Deen, "RIE of GaSb with an ECR source using Methane/Hydrogen chemistry in an Argon plasma," *J. Electrochem. Soc.*, **154**, p.H127-H130, (2007).

[100] D. Cullity and S. R. Stock, *Elements of X-Ray Diffraction*, Prentice-Hall Inc., 3rd ed., (2001).

[101] Paul F. Fewster, "X-ray diffraction from low-dimensional structures," *Semiconductor Science and Technology*, **8**, p.1915-1934, (1993).

[102] Paul F. Fewster, *X-ray Scattering from Semiconductors*, Imperial College Press, 2nd ed., (2003).

[103] K. Bowen and B. Tanner, *High Resolution X-ray Diffractometry and Topography*, Taylor & Francis, (1998).

[104] K. Yuan, K. Radhakrishnan, H. Q. Zheng, Q. D. Zhuang and G. I. Ing, "Characterization of linearly graded metamorphic InGaP buffer layers on GaAs using high-resolution X-ray diffraction," *Thin Solid Films*, **391**, p.36-41, (2001).

[105] J. A. Czaban, *Ph.D. Thesis*, Dept. of Engineering Physics, McMaster University, (2007).

[106] Julia Huang, *M.A.Sc. Thesis*, Dept. of Engineering Physics, McMaster University, (2004).

[107] M. A. G. Halliwell, M. H. Lyons, S. T. Davey, M. Hockly, C. G. Tuppen, and C. J. Gibbings, "Estimation of percentage relaxation in Si/$Si_{1-x}Ge_x$ strained-layer superlattices," S*emicond. Sci. Technol.*, **4**, p.10-15, (1989).

[108] Shun Lien Chuang, *Physics of Optoelectronic Devices*, Wiley, (1995).

[109] E. P. O'Reilly, "Valence band engineering in strained-layer structures," *Semicond. Sci. Technol.*, **4**, p.121-137, (1989).

[110] J. A. Czaban, D. A. Thompson and B. J. Robinson, "Improved InAsP metamorphic layers grown on an InP substrate using underlying InP grown at low temperatures," *Semicond. Sci. Technol.*, **22**, p.408-412, (2007).

[111] D. Lee, M. S. Park, Z. H. Luo, R. Beresford and C. R. Wie, "Characterization of metamorphic $In_xAl_{1-x}As$/GaAs buffer layers using reciprocal space mapping," *J. Appl. Phys.*, **101**, p.063523 (2007).

[112] M. Fatemi and R E. Stahlbush, "X-ray rocking curve measurement of composition and strain in Si-Ge buffer layers grown on Si substrates", *App. Phys. Lett.*, **58**, p.825-827, (1991).

[113] H. J. Haugan, L. Grazulis, G. J. Brown, K. Mahalingam and D. H. Tomich, "Exploring optimum growth for high quality InAs/GaSb type-II superlattices," *J. Cryst. Growth,* **261**, p.471-478, (2004).

[114] R. Kaspi, "Compositional abruptness at the InAs-on-GaSb interface: Optimizing growth by using the Sb desorption signature," *J. Cryst. Growth,* **201/202**, p.864-867, (1999).

[115] F. M. Mohammedy, O. Hulko, B. J. Robinson, D. A. Thompson, M. J. Deen and J. G. Simmons, "Growth and characterization of GaAsSb metamorphic samples on an InP substrate," *J. Vac. Sci. Technol. A*, **24**, p.587-590, (2006).

[116] F. M. Mohammedy, O. Hulko, B. J. Robinson, D. A. Thompson and M. J. Deen, "Effect of growth temperature on InGaSb metamorphic layers and the fabrication of InGaSb p-i-n diodes," *J. Vac. Sci. Technol. B*, **26**, p.636-642, (2008).

[117] H. Ehsani, I. Bhat, R. J. Gutmann, G. Charache and M. Freeman, "Role of relative tilt on the structural properties of GaInSb epitaxial layers grown on (001) GaSb substrates," *J. Appl. Phys.*, **86**, p.835-840, (1999).

[118] G.W. Reynolds, J.W. Taylor and C.J. Brooks, "Direct measurement of x-ray mask sidewall roughness and its contribution to the overall sidewall roughness of chemically amplified resist features," *J. Vac. Sci. Technol. B*, **17**, p.3420-25, (1999).

[119] M. Kodama, "Improvement of reverse leakage current characteristics of GaSb and $Al_{0.3}Ga_{0.7}Sb$/GaSb diodes grown by MBE," *Solid-State Electronics*, **37**, p.1567-1569 (1994).

[120] M. Perotin, P. Coudray, L. Gouskov, H. Luquet, C. Llinares, J. J. Bonnet, L. Soonckindt and B. Lambert, "Passivation of GaSb by sulphur treatment," *J. Electron. Mater.*, **23**, p.7-12 (1994).

[121] P. Dutta, J. Langer, V. Bhagwat, and J. Juneja, "Dry etching, surface passivation and capping processes for antimonide based photodetectors," Infrared Technology and Applications XXXI, *Proceedings of SPIE*, Vol.**5783**, p.98-105, (2005).

[122] Chavan, A. Chandola, S. Sridaran and P. Dutta, "Surface passivation and capping of GaSb photodiode by chemical bath deposition of CdS," *J. Appl. Phys.*, **100**, 064512 (2006).

[123] E. Papis-Polakowska, "Surface treatments of GaSb and related materials for the processing of mid-infrared semiconductor devices," *Electron Technology - Internet Journal*, **37/38**, p.1-34, (2005/2006), http:// www.ite.waw.pl/etij/

[124] S. M. Sze, *Physics of Semiconductor Devices*, 2nd Ed., John Wiley and Sons, (1981).

[125] S. R. Forrest, "Performance of InGaAsP photodiodes with dark current limited by diffusion, generation, recombination and tunneling," *IEEE J. Quantum Electron.*, **17**, p.217-226, (1981).

[126] M. A. Kinch, "Electronic properties of HgCdTe," *J. Vac. Sci. Technol.*, **21**, p.215-219, (1982).

[127] F. K. Hopkins and J. T. Boyd, "Dark current analysis of InSb photodiodes," *Infrared Physics*, **24**, p.391-395, (1984).

[128] A. Tevke, C. Besikci, C. Van Hoof and G. Borghs, "InSb infrared p-i-n photodetectors grown on GaAs coated Si substrates by molecular beam epitaxy," *Solid-State Electronics*, **42**, p.1039-1044, (1998).

[129] Q. K. Yang, F. Fuchs, J. Schmitz, and W. Pletschen, "Investigation of trap-assisted tunneling current in InAs/ (GaIn)Sb superlattice long-wavelength photodiodes," *Appl. Phys. Lett.*, **81**, p.4757-4759, (2002).

[130] V. Gopal, "Variable-area diode data analysis of surface and bulk effects on HgCdTe photodetector arrays," *Semicond. Sci. Technol.*, **9**, p.2267-2271, (1994).

[131] V. Gopal, "A general relation between zero-bias resistance-area product and perimeter-to-area ratio of the diodes in variable-area diode test structures," *Semicond. Sci. Technol.*, **11**, p.1070-1076, (1996).

[132] P. K. Bhattacharya, *Semiconductor Optoelectronic Devices*, 1996, Prentice-Hall.

[133] T. F. Refaat, M. N. Abedin, V. Bhagwat, I. B. Bhat, P. S. Dutta, and U. N. Singh, "InGaSb photodetectors using an InGaSb substrate for 2 μm applications", *Appl. Phys. Lett.*, **85**, p.1874 (2004).

[134] F. Pascal-Delannoy, N. J. Mason, G. Bougnot, P. J. Walker, J. Bougnot, A. Gianni, G. G. Allogho, "InGaSb/GaSb photodiodes grown by MOVPE," *J. Crys. Growth*. **124** , p.409-414, (1992).

[135] A. Hood, M. Razeghi, E. H. Aifer, G. J. Brown, "On the performance and surface passivation of type II InAs/ GaSb superlattice photodiodes for the very-long-wavelength infrared," *Appl. Phys. Lett.*, **87**, p.151113, (2005).

[136] J. Vanhellemont, E. Simoen, and C. Claeys, "Extraction of the minority carrier recombination lifetime from forward diode characteristics," *Appl. Phys. Lett.*, **66**, p.2894-2896, (1995).

[137] Hood, P. Y. Delaunay, D. Hoffman, B. M. Nguyen, Y. Wei and M. Razeghi, "Near bulk-limited R_oA of long-wavelength infrared type-II InAs/GaSb superlattice photodiodes with polyimide surface passivation," *Appl. Phys. Lett.*, **90**, p.233513, (2007).

[138] J. V. Li, S. L. Chuang, O. V. Sulima, J. A. Cox, "Passivation of AlGaAsSb/InGaAsSb/GaSb photodiodes using aqueous $(NH_4)_2S$ solution and polyimide encapsulation," *J. Appl. Phys.*, **97**, p.104506, (2005).

[139] P. S. Dutta, e-mail communication, (2008).

[140] Y. Tian., T. Zhou, B. Zhang, Y. Jin and H. Jiang, "Analysis of the RoA product and detectivity in a GaInAsSb infrared photovoltaic detector," *J. Phys. D*, **31**, p.3291-3297, (1998).

[141] Krier, H. H. Gao and Y. Mao, "A room temperature photovoltaic detector for the mid-infrared (1.8 – 3.4 μm) wavlength region," *Semicond. Sci. Technol.*, **13**, p.950-956, (1998).

[142] F. Pascal-Delannoy, J. Bougnot, G. G. Allogho, A. Gianni, L. Gouskov and G. Bougnot, "MOVPE grown $Ga_{0.6}In_{0.4}Sb$ photodiodes for 2.55 μm detection," *Electron. Lett.*, **28**, p.531-532, (1992).

[143] M. Levinshtein, S. Rumyantsev and M. Shur (ed.), Handbook Series on Semiconductor Parameters, Vol.1 and 2, p.125(v.1), 89(v.2), (1996). Also available at Ioffe Institute online archive: http://www.ioffe.ru/SVA/NSM/Semicond/GaSb/electric.html .

[144] V. Gopal and S. Gupta, "Contribution of dislocations to the zero-bias resistance-area product of LWIR HgCdTe photodiodes at low temperatures," *IEEE Trans. Electron. Devices*, **51**, p.1078-1083, (2004).

[145] G. K. Wertheim and G. L. Pearson, "Recombination in plastically deformed germanium", *Phys. Rev.*, **107**, p.694, (1957).

[146] E. Plis, P. Rotella, S. Raghavan, L. R. Dawson, S. Krishna, D. Le and C. P. Morath, "Growth of room-temperature "arsenic free" infrared photovoltaic detectors on GaSb substrate using metamorphic InAlSb digital alloy buffer layers", *Appl. Phys. Lett.*, **82**, p.1658-1660, (2003).

[147] G. E. Stillman and C. M. Wolfe, "Avalanche photodiodes," in *Semiconductors and Semimetals*, edited by R. K. Willardson and A. C. Beer, Vol.12, volume editor W. T. Tsang, p.1-245, Academic Press, (1977).

[148] F. Capasso, "Physics of avalanche photodiodes," in *Semiconductors and Semimetals*, edited by R. K. Willardson and A. C. Beer, Vol.22, volume editor W. T. Tsang, p.1-245, Academic Press, (1985).

[149] K. F. Brennan, *The Physics of Semiconductors with Applications to Optoelectronic Devices*, Cambridge University Press, U.K., (1999).

[150] R. J. McIntyre, "Multiplication noise in uniform avalanche diodes," *IEEE Transactions on Electron Devices*, **13**, 1, p.164-168, (1966).

[151] M. P. Mikhailova and I. A.Andreev, "High speed avalanche photodiodes for the 2-5μm spectral range", in *Mid-Infrared Semiconductor Optoelectronics*, A. Krier (ed.), Springer Verlag, p.547-592, (2006).

[152] A. P. Dmitriev, M. P. Mikhailova and I. N. Yassievich, "Impact ionization in AIIIBV semiconductors in high electric fields," *Phys. Stat. Sol. (b)*, **140**, p.9-37, (1987).

[153] M. Z. Zhingarev, V. I. Korolkov, M.P. Mikhailova, V.V. Sazonov and D. N. Tretyakov, "Avalanche multiplication and coefficients of impact ionization in p-n homojunctions and heterojunctions made of GaSb and its solid solutions," *Sov. Phys. Semicond.*, **14**, p.801-806, (1980).

[154] B. K. Ridley, "A model for impact ionization in wide-gap semiconductors," *J. Phys. C.*, **16**, p.4733-4751, (1983).

[155] A. Bandyopadhyay and M. Jamal Deen, "Photodetectors for optical fiber communications", in *Photodetectors and Fiber Optics*, H. S. Nalwa (ed.), Academic Press, p.307-368, (2001).

[156] C. H. Grein, H. Ehrenreich, "Impact ionization enhancements in $Al_xGa_{1-x}Sb$ avalanche photodiodes," *Appl. Phys. Lett.*, **77**, p.3048-3050, (2000).

[157] O. Hildebrand, W. Kuebart, K. W. Benz and M. H. Pilkhun, "$Ga_{1-x}Al_xSb$ avalanche photodiodes: Resonant impact ionization with very high ratio of ionization coefficients," *IEEE J. of Quantum Electron.*, **17**, p.284-288, (1981).

[158] M. Z. Zhingarev, V. I. Korolkov, M. P. Mikhailova and V. V. Sazonov, "Dependence of the electron and hole impact-ionization coefficients on the orientation and composition in solid solutions," *Sov. Tech. Phys. Lett.*, **7**, p.637-638, (1981).

[159] Y. Okuto and C. R. Crowell, "Energy-conservation considerations in the characterization of impact ionization in semiconductors," *Phys. Rev.*, **6**, p.3076-3081, (1972).

[160] C. L. F. Ma, M. J. Deen and L. E. Tarof, "Characterization and modeling of SAGCM InP/InGaAs avalanche photodiodes for multigigabit optical fiber communications," in *Advances in Imaging and Electron Physics*, vol.**99**, Academic Press Inc., (1998).

[161] K. Brennan, K. Hess, and Y.C. Chang, "Theory of steady-state high-filed hole transport in GaSb and $Al_xGa_{1-x}Sb$: The impact ionization resonance," *J. Appl. Phys.*, **57**, p.1971-1977, (1985).

[162] I. Vurgaftman, J. R. Meyer, L. R. Ram-Mohan, "Band parameters for III-V compound semiconductors and their alloys," *J. Appl. Phys.*, **89**, p.5815-5875, (2001).

[163] M. Fatemi, "Refinement of high-resolution x-ray diffraction data in characterizing epitaxial layers and multiple-quantum wells by the peak separation technique," *J. Crys. Growth*, **207**, p. 188-199, (1999).

[164] N. Yamamoto, K. Akahane, and S. Gozu, "Over 1.3 μm continuous-wave laser emission from InGaSb quantum-dot laser diode fabricated on GaAs substrates," *Appl. Phys. Lett.*, **86**, 203118 (2005).

[165] R. Q. Yang, C. J. Hill, K. Mansour, Y. Qiu, A. Soibel, R. E. Muller, and P. M. Echternach, "Distributed feedback mid-IR interband cascade lasers at thermoelectric cooler temperatures", *IEEE Journal of Selected Topics In Quantum Electronics*, **13**, pp.1074-1078, (2007).

[166] V. M. Smirnov, P. J. Batty, R. Jones, A. Krier, V. I. Vasil'ev, G. S. Gagis and V. I. Kuchinskii, "GaInAsPSb/GaSb heterostructures for mid-infrared light emitting diodes," *Phys. Stat. Sol. (a)*, **204**, pp.1047–1050, (2007).

Appendix 1

Fundamental parameters [143],[162].

				$In_xGa_{1-x}Sb$		
		GaSb	**InSb**	x = 0.10	x = 0.182	Comments
Lattice constant, a	Å	6.0954	6.4788	6.134	6.165	Vegard's
Bandgap at room temperature, E_g	eV	0.725	0.149	0.63	0.558	Bowing $-x(1-x)C$, C = 0.415
Bandgap at 0 K, E_g	eV	0.812	0.235	0.717	0.707	
L-bandgap at room temperature, E_{g-L}	eV	0.875	0.93	0.845	0.826	Bowing $-x(1-x)C$, C = 0.4
Split-off bandgap, Δ_{so}	eV	0.76	0.81	0.756	0.754	Vegard's
Stiffness coefficients	C_{11}, Gpa	884.2	684.7	864.25	847.9	Vegard's
	C_{12}, Gpa	402.6	373.5	399.7	397.3	Vegard's
Poisson's ratio		0.313	0.353	0.317	0.32	Vegard's
Electron effective mass, m_e*/m		0.0412	0.0135	0.037	0.0347	$0.014+0.0178(1-x)+.0092(1-x)^2$
Light hole effective mass, $m_{lh}*/m$		0.05		0.044	0.04	$0.015+0.01(1-x)+.025(1-x)^2$
Heavy hole effective mass, $m_{hh}*/m$		0.28		0.403	0.405	$0.435-0.03(1-x)$
Density of states hole mass, m_h*/m		0.294		0.413	0.414	$\left(m_{lh}^{1.5}+m_{hh}^{1.5}\right)^{2/3}$
Split-off band effective mass, $m_{so}*/m$		0.12	0.11	0.119	0.118	Vegard's
Intrinsic concentration, n_i	cm^{-3}	7.4E11		5.6E12	1.8E13	Room Temp.
Dielectric constant, ε_r		15.7		15.81	15.9	$16.8-1.1(1-x)$
LO phonon wave-number	cm^{-1}	233	197	229.4	226.5	Vegard's
Temperature dependence of Γ-band	α, meV/K	0.417	0.32	0.407	0.399	Vegard's
	β, K	140	170	143	145.5	Vegard's

Appendix 2: Lithography steps

We followed the standard lithography process to define patterns of squares and circles of different sizes onto a GaSb wafer. The flowchart for the steps involved in the processing done in a Class-10000 Clean Room facility are shown in Figure A-1.

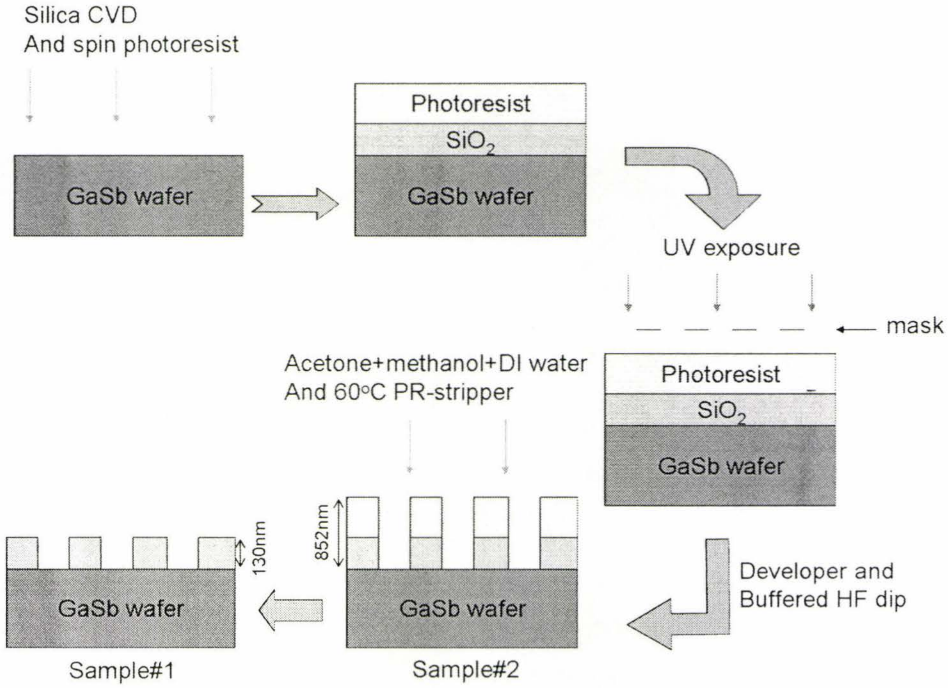

Figure A-1: Flowchart for standard lithography.

The steps are mentioned below:

Step-1: Deposit silicon dioxide/silicon nitride on the wafer by chemical vapor deposition (CVD). The thickness of the deposited oxide has to be carefully chosen.

Step-2: Desorb the sample wafer on a hot-plate at 110°C for 5 min.

Step-3: Start-up the mask-aligner machine. Prepare two separate syringes and fill them up with primer (hexamethyle disilazane, HMDS) and positive photoresist (PR S1808 or SC1827).

Step-4: Calibrate the rotation speed of the 'primer-bench' at 4000 rpm for 30 s. Put the sample wafer back on the primer rotational bench and put primer first. Wait for 30 s and then start rotation for 30 s. Next, spread the photoresist solution onto the wafer. Wait another 30 s and then start rotation. The rotation speed has to be determined according to the specific resist's spin-speed relation and the desired mesa height. For a thick mesa height, the resist must cover the complete mesa, hence the rotation speed should be chosen accordingly.

Step-5: Soft-bake the wafer at 110° C for 2 min.

Step-6: Put the wafer onto the mask-aligner and with the mask #1 as shown in Figure 5.3, expose the wafer with ultraviolet light. The exposure time and the exposing power of the light source have to be carefully noted. Usually, they are around 4.0 s and 7.7 mW for PR1808 respectively to provide an exposure of ~ 30 mJ. For SC1827, this exposure is about 215 mJ. Note that the exposure time changes with different processing requirements.

Step-7: After exposure, the sample has to be put in a 'developer' solution prepared before. This is actually NaOH (351 Shipley) 10 mL mixed with 50 mL de-ionized water.

Step-8: Immerse the sample in the 'developer' solution mentioned above. About 25 s is good enough for GaSb samples. Usually, it can be seen that the undeveloped photoresist withers away by that time.

Step-9: Hard-bake the sample at 120 °C for 2 min. Without hard-bake, the photoresist would vanish with the next step.

Step-10: Rinse with 'buffered HF' (49% HF in 10 part of NH4Fl solution in water) solution (BHF:water = 1:10) to etch off the silicon dioxide exposed to the HF solution.

Step-11: Measure the thickness of the developed mesa (which is photoresist plus silicon dioxide) in a profilometer (alpha-step).

Step-12: Rinse in Acetone, Methanol and de-ionized water to get rid of any remaining photoresist. The resulting sample has only silicon dioxide masks on GaSb wafer.

For lift-off (i.e. the third mask), the processes are slightly different. After the second mask, the following steps are followed for metal lift-off:

Step-13: Spin photoresist SC1827 (for mesas thicker than 1 μm) for 30 seconds at 1500 rpm (spin speed depends on the mesa height) and wait for 30 seconds.

Step-14: Soft bake at 90°C for 2 min.

Step-15: Use longer exposure (260 mJ) in the photolithography machine with the third mask in each mask-set. For non-liftoff procedures, 215 mJ exposure is fine with SC1827.

Step-16: Toluene dip for 5 min and then blow dry by nitrogen gun.

Step-17: Over develop for 90 seconds in the developer solution (351).